ADVANCES IN INORGANIC CHEMISTRY, VOL. 35

INTERACTION BETWEEN OPTICAL CENTERS AND THEIR SURROUNDINGS: AN INORGANIC CHEMIST'S APPROACH

G. BLASSE

Debye Research Institute, University of Utrecht,
3508 TA Utrecht, The Netherlands

I. Introduction

Nowadays the existence of optical centers in solids, in liquids, and in molecules is well known and their properties have been studied inten-

sively. Two of these are well established, viz., the phenomenon of optical absorption leading to colored compositions, and the phenomenon of emission of radiation (luminescence).

There is hardly a better example to illustrate this than the case of ruby (Al_2O_3: Cr^{3+}). Ruby is a beautiful gemstone whose color varies from pale pink to deep red, depending on the chromium concentration. Artificial crystals are presently available. The "cold fire" of ruby—its deep-red luminescence—increases the attraction these crystals have for many people, not only scientists.

The spectroscopic properties of ruby have been studied for over one hundred years starting with the work by Becquerel (1867), who excited ruby with sunlight. He claimed that the properties of this crystal were intrinsic, but later it was shown that the color as well as the luminescence of ruby are due to the Cr^{3+} ion that plays the role of an optical center in the nonabsorbing Al_2O_3 host. Only much later these properties could be explained by considering the influence of the surroundings of the Cr^{3+} center on its energy levels (crystal-field theory). For a summary of ruby history the reader is referred to ref. *1*.

The study of optical centers in solids, liquids, and molecules has fascinated many scientists over a range of years. However, not only scientific curiosity has pushed forward this type of spectroscopy. Simultaneously, many possible applications became clear. The first solid state laser was based on a ruby crystal. Also, in the development of tunable infrared lasers the Cr^{3+} ion played an important role.

Some applications other than laser materials are the following: luminescent materials for lighting, for display in cathode-ray tubes, and for X-ray radiography; scintillator materials; electroluminescent thin films; glasses for solar concentrators; colored materials for all types of applications (e.g., pigments). The greater part of these applications were reviewed in refs. *2* and *3*. Optical centers can in many cases also be used as probes of the surroundings.

In this chapter we will concentrate on the progress in this field over the last decade, stressing the interaction between the optical center and its surroundings (the ligands). We will refrain from a strict mathematical approach. For this the reader is referred to refs. *4–6*. In Section II the models necessary for our considerations will be introduced and the phenomena to be expected will be derived. These models are mainly the configurational coordinate model and the Förster–Dexter model of energy transfer. Crystal field theory will be assumed to be familiar to the reader. The phenomena involved are radiative and nonradiative transitions, spectral band shapes including zero-phonon lines, as well as energy transfer and energy migration.

In later sections the various developments will be illustrated by considering several examples; the reader is referred to the contents given above.

For those who are not yet familiar with these types of phenomena, this section ends with a qualitative picture of the physical phenomena to be discussed. Figure 1 shows an optical center (an ion or a complex ion) in a solid or a liquid. The center is irradiated. For simplicity we assume that the surroundings do not absorb the irradiating light. The center shows optical absorption, so that it makes a transition from the ground state to the excited state. If the irradiation is with visible light, the sample is colored. The excited state will ultimately return to the ground state. This may occur by a nonradiative or a radiative process.

In the former case the energy of the excited state is used to excite the vibrations of the surroundings (generation of heat). The latter case is known as luminescence (see Fig. 1). In this field the irradiation is called excitation. Usually the emission is situated at longer wavelengths than the excitation. The energy difference between these two is called the Stokes shift.

The quantum efficiency (q) of the luminescence is the ratio of the number of photons emitted and the number of photons absorbed. If there are no competing nonradiative transitions, $q = 1$; if the nonradiative transitions are dominating, $q \sim 0$, and there is practically no emission.

A more complicated situation occurs if two (equal or unequal) centers are close together (Fig. 2). The excited center may transfer its excitation energy to the neighboring center that is still in the ground state:

$$\text{center S}^* + \text{center A} \rightarrow \text{center S} + \text{center A}^* \qquad (1)$$

where the excited state is marked by an asterisk. This process may be followed by emission from A or by a nonradiative decay on A. In the former case we speak of sensitized emission (A is sensitized by S); in the latter case A is called a quenching center.

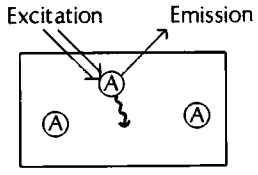

FIG. 1. Luminescence processes in an isolated ion (see also text).

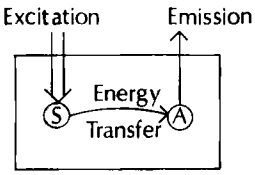

FIG. 2. Energy transfer between two ions (see also text).

We now start with a discussion of the models we will use in our considerations.

II. Models Used to Describe the Interaction between Optical Centers and Their Surroundings

In this section we will first consider the configurational coordinate diagram (*4*, *7*) that describes the interaction of an optical center with its surroundings in the absence of center-center interaction. Later we will deal with the interaction between two centers that results in energy transfer (*4*, *8*).

A. The Configurational Coordinate Diagram

Let us consider a dopant ion in a host lattice and assume that it shows luminescence upon illumination. What we will have to discuss is the interaction of the dopant ion with the vibrations of the lattice. The environment of the dopant ion is not static: the surrounding ions vibrate about some average positions, so that the crystalline field varies. The simplest model to account for the interaction between the dopant ion and the vibrating lattice is the single-configurational coordinate model (*4*, *7*).

In this model we consider only one vibrational mode, viz., the so-called breathing mode in which the surrounding lattice pulsates in and out around the dopant ion (symmetrical stretching mode). This mode is assumed to be described by the harmonic oscillator model. The configurational coordinate (Q) describes the vibration. In our approximation it represents the distance between the dopant ion and the surrounding ions. In ruby this Q would be the Cr^{3+}–O^{2-} distance.

If we plot energy vs. Q we obtain for the electronic states parabolas (harmonic approximation). This is presented in Fig. 3 for the electronic ground state g and one electronic excited state e. Further Q_0 presents

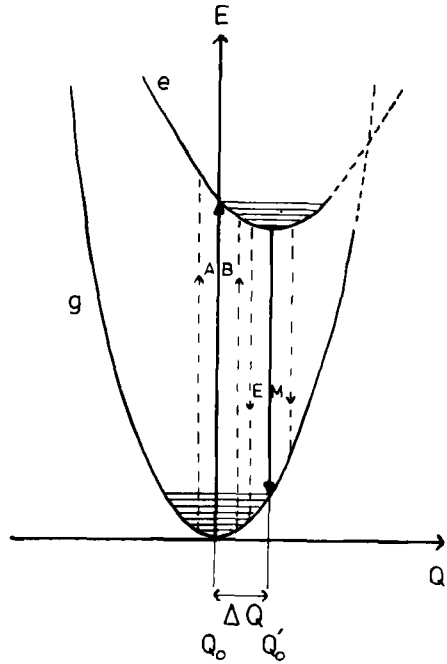

FIG. 3. The configurational coordinate diagram. The curves g and e relate to the ground state; ΔQ gives the parabolas offset. (See also text.)

the equilibrium distance in the ground state, Q'_0 that in the excited state. Note that in general these will be different! The g parabola is given by

$$V = \tfrac{1}{2}k(Q - Q_0)^2 \tag{2}$$

where k is the force constant. Within the parabolas the (equidistant) vibrational energy levels have been drawn. They are numbered by $n = 0, 1, 2 \ldots$. The excited state parabola is drawn in such a way that the force constant is weaker than in the ground state. Since the excited state is usually weaker bound than the ground state, this is a representative situation.

Optical absorption corresponds to a transition from the g to the e state under absorption of electromagnetic radiation. Emission is the reverse transition. Let us now consider how these transitions have to be described in the configurational coordinate model. It is essential to remember that the wave function of the lowest vibrational state (i.e.,

$n = 0$) is Gaussian; that is, the most likely value of Q is Q_0 (or Q'_0 in the excited state). For the higher vibrational states, however, the most likely value is at the edges of the parabola (i.e., at the turning points, like in the classic pendulum).

The most probable transition in absorption at low temperatures is from the $n = 0$ level in g, starting at the value Q_0. Optical absorption corresponds to a vertical transition, because the transition $g \rightarrow e$ on the dopant ion occurs so rapidly that the surrounding lattice does not change during the transition (Born–Oppenheimer approximation). Our transition will end on the edge of parabola e, since it is there that the vibrational states have their highest amplitude. This transition, drawn as a solid line in Fig. 3, corresponds to the maximum in the absorption band. However, we may also start at Q values different from Q_0, although the probability is lower. This leads to the width of the absorption band, indicated in Fig. 3 by broken lines. It can be shown that the probability of the optical transition between the $n = 0$ vibrational level of the ground state and the $n = n'$ vibrational level of the excited state is proportional to

$$<e(Q) \mid r \mid g(Q) >< \chi n' \mid \chi_0> \tag{3}$$

where r presents the electric-dipole operator and χ the vibrational wave functions. The first term, the electronic matrix element, is independent of the vibrational levels; the second term gives the vibrational overlap. The transition from $n = 0$ to $n' = 0$ does not involve the vibrations. It is called the zero-vibrational transition (or no-phonon transition). Equation (3) shows that the effect of the vibrations is mainly to change the shape of the absorption line (or band), but not the strength of the transition (which is given by the electronic matrix element).

What happens after the absorption transition? First we return to the lowest vibrational level of the excited state; that is, the excited state relaxes to its equilibrium position, giving up the excess energy as heat to the lattice. The system of dopant ion and surroundings is then in the relaxed excited state. The emission transition can be described in exactly the same way as the absorption transition. This is indicated in Fig. 3 in the same way as for the absorption transition. Finally the system relaxes within the g parabola to the lowest vibrational level.

If the temperature is not low, higher vibrational levels may be occupied thermally, so that we start the process not only from $n = 0$, but also from $n = 1$, and possibly from even higher levels. This leads to a further broadening of the absorption and emission bands, but does not change our arguments essentially.

The emission transition will usually be situated at lower energy than the absorption transition. This phenomenon is known as the Stokes shift. Only the zero-vibrational transition is expected to occur at the same energy in the absorption and emission spectra. The Stokes shift is a direct consequence of the relaxation processes that occur after the optical transitions. It is obvious that the larger $Q'_o - Q_o$ is, the larger the Stokes shift will be. If the two parabolas have the same shape and vibrational frequency, it is possible to define a parameter S (the so-called Huang–Rhys parameter) as follows

$$\tfrac{1}{2}k(Q'_o - Q_o)^2 = S\hbar\omega \tag{4}$$

where $\hbar\omega$ is the energy difference between the vibrational levels. The Stokes shift is then given by

$$\Delta E_s = k(Q'_0 - Q)^2 - \hbar\omega = 2S\hbar\omega \tag{5}$$

The parameter S measures the interaction between the dopant ion and the vibrating lattice. Equation [5] shows that if S is large, the Stokes shift is also large. Equation [4] shows that S is immediately related to the offset of the parabolas in the configurational coordinate diagram (Fig. 3). This offset, $\Delta Q = (Q'_o - Q_o)$, may vary considerably as a function of the dopant ion and as a function of the vibrating lattice, as we will see below.

It can be shown that the relative intensity of the zero-vibrational transition ($n_g = 0 \leftrightarrow n_e = 0$) is $\exp(-S)$ (*5, 7*). We can now divide our luminescent centers into three classes, viz.,

a. Those with weak coupling (i.e., $S < 1$), so that the zero-vibrational transition dominates the spectrum.

b. Those with intermediate coupling (i.e., $1 < S < 5$), so that the zero-vibrational transition is observable, but not the strongest line in the absorption or emission band.

c. Those with strong coupling (i.e., $S > 5$), so that the zero-vibrational transition is so weak that it is not observable in the spectra. This case is also characterized by large Stokes shifts.

Figure 4 shows three emission spectra that are representative of the three cases. Characteristic examples of case (a) are the trivalent rare earth ions. The value of S is so small for these ions that the spectra consist in good approximation of the zero-vibrational transitions only. Figure 4a gives as an example the emission spectrum of the Gd^{3+} ion in LaB_3O_6. It consists of one strong electronic line at about 310 nm,

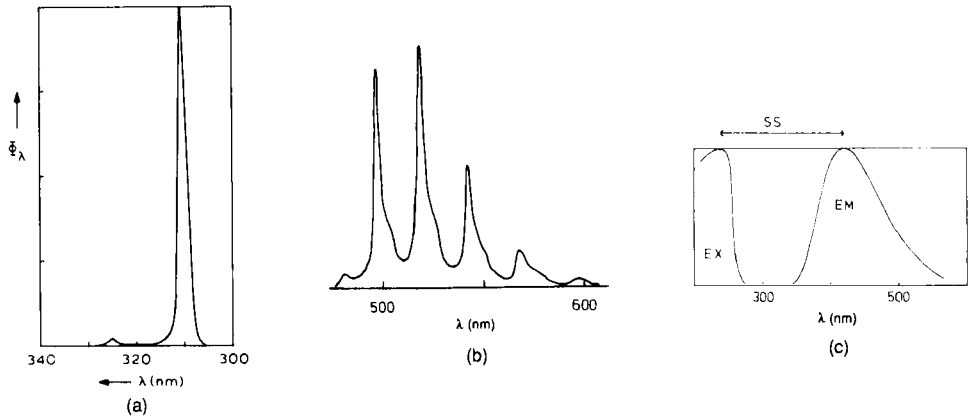

FIG. 4. Emission spectra of (a) LaB_3O_6:O_6:Gd (weak coupling), (b) UO_2^{2+} (intermediate coupling), and (c) $CaWO_4$ (strong coupling). In this chapter emission spectra are plotted as radiant power per constant wavelength interval and excitation spectra as relative quantum output, unless otherwise indicated.

whereas the weak repetition at about 325 nm is a vibronic transition. Actually the energy difference between these two lines corresponds to the vibrational stretching frequency of the borate group in LaB_3O_6.

A characteristic example of case (b) is the uranyl ion (UO_2^{2+}). The $n_e = 0 \rightarrow n_g = 2$ line dominates in the spectrum (Fig. 4b). The tungstate ion (WO_4^{2-}) is a good example of case (c). The very broad emission spectrum (see Fig. 4c) does not show any vibrational structure at all, the Stokes shift is very large ($\sim$16,000 cm^{-1}) and the zero-vibrational transition is not observable, not even at the lowest possible temperatures nor for the highest possible resolving powers.

Finally we draw attention to the fact that the single configurational coordinate diagram is only an approximation. In practice there is more than one vibrational mode involved and the system is not harmonic. Therefore the value of S is not so easy to determine as suggested above. However, for a general understanding the simple model is extremely useful, as we will see below.

If we measure an absorption or emission spectrum, the following properties of the bands or lines are of importance:

a. their spectral position, that is, the energy at which the transition occurs;

b. their shape, that is, sharp line, structured narrow band, or structureless broad band;

c. their intensity.

For the spectral position the reader will be referred to the literature, except for details of importance. The shape of the bands was discussed above (see Figs. 3 and 4). The intensity is contained in the electronic matrix element

$$<e(Q) \mid r \mid g(Q)> \tag{6}$$

in Eq. (3). The intensity can be very low if selection rules apply. Here we mention a few, well-known examples.

For electric-dipole transitions the parity of the initial and final states should be different (parity selection rule). This implies that transitions within one and the same shell, for example $3d$ or $4f$, are forbidden. This selection rule may be relaxed by the admixture of opposite-parity states due to the crystal field, or by vibrations of suitable symmetry.

Optical transitions are forbidden between states of different spin multiplicity (spin selection rule). This selection rule may be relaxed by the spin-orbit coupling. Since the latter increases strongly with the atomic number, the value of this selection rule decreases if we proceed from top to bottom through the periodic table.

Many other selection rules of a more specialized nature will be mentioned where applicable and as far as necessary.

If we consider dopant ions in a solid, their spectral features will show inhomogeneous broadening, even if their mutual interaction is neglected. The reason for this is the fact that the crystal field at the dopant ion varies slightly from ion to ion due to the presence of defects, as, for example, impurities, vacancies, dislocations, or the surface (*9*). As a matter of fact the inhomogeneous broadening will be more pronounced for line spectra than for broadband spectra. Its magnitude is also much larger in disordered solids (glasses!) than in ordered solids (*10*).

Up to this point it was assumed that the return from the excited state to the ground state is radiative. In other words, the quantum efficiency (q), which gives the ratio of the numbers of emitted and absorbed quanta, was assumed to be 100%. This is usually not the case. Actually there are many centers which do not luminescence at all. We will try to describe here the present situation of our knowledge of nonradiative transitions that is satisfactory only for the weak-coupling case. For detailed reviews the reader is referred to ref. *11*.

Let us consider the configurational coordinate diagrams of Fig. 5 in order to understand the relevant physical processes. Figure 5a presents essentially the same information as Fig. 3. Absorption and emission transitions are quite possible and are Stokes-shifted relative to each other. The relaxed-excited state may, however, reach the crossing of the

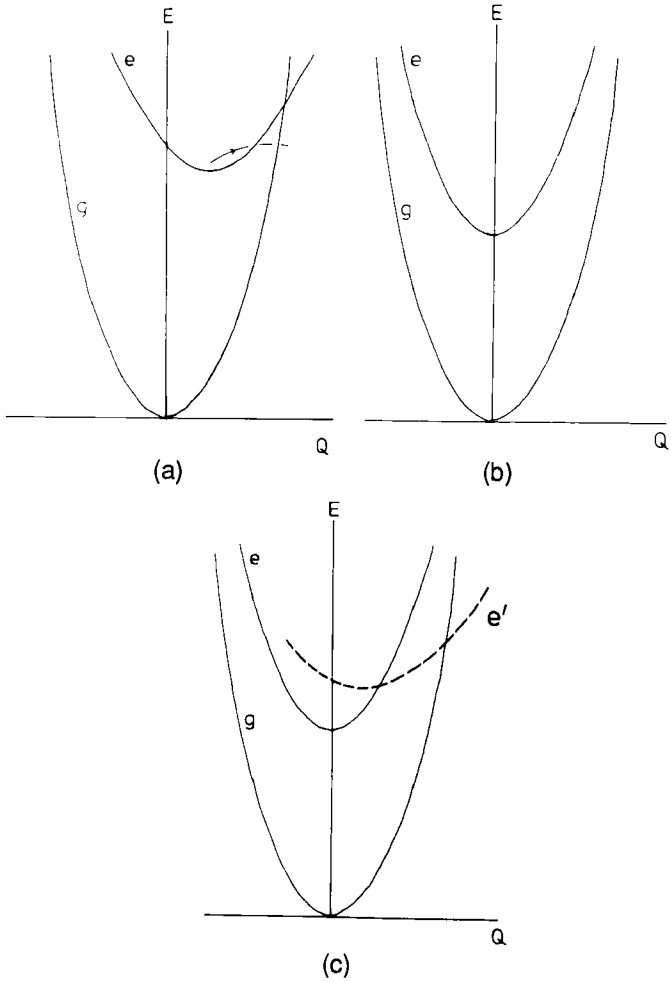

FIG. 5. Nonradiative transitions in the configurational coordinate model: (a) strong coupling, (b) weak coupling, (c) combination of both.

two parabolas if the temperature is high enough. Via the crossing, it is possible to return to the ground state in a nonradiative manner. The excitation energy is then completely given up as heat to the lattice. This model accounts for the thermal quenching of luminescence.

In Fig. 5b the parabolas are parallel ($S = 0$) and will never cross. It is impossible to reach the ground state in the way described for Fig. 5a.

However, nonradiative return to the ground state is possible if certain conditions are fulfilled; that is, the energy difference ΔE should be equal to or less than 4–5 times the highest vibrational frequency of the surroundings. In that case this amount of energy can excite simultaneously a few high-energy vibrations and is then lost for the radiative process. Usually this nonradiative process is called multiphonon emission.

In Fig. 5c both processes are possible in a three-parabola diagram. The parallel parabolas will belong to the same configuration, so that they are connected by forbidden optical transitions only. The third one originates from a different configuration and is probably connected to the ground state by an allowed transition. This situation occurs often. Excitation (absorption) occurs now from the ground state to the highest parabola in the allowed transition. From here the system relaxes to the relaxed excited state of the second parabola. Figure 5c shows that the nonradiative transition between the two upper parabolas is easy. Emission occurs now from the second parabola (line emission). This situation is found for $Al_2O_3:Cr^{3+}$ ($^4A_2 \rightarrow {}^4T_2$ excitation, $^4T_2 \rightarrow {}^2E$ relaxation, $^2E \rightarrow {}^4A_2$ emission), Eu^{3+} ($^7F \rightarrow$ charge-transfer state excitation, charge-transfer state to ^5D relaxation, $^5D \rightarrow {}^7F$ emission), and Tb^{3+} ($^7F \rightarrow 4f^7 5d$ excitation, $4f^7 5d \rightarrow {}^5D$ relaxation, $^5D \rightarrow {}^7F$ emission).

In general the temperature dependence of the nonradiative processes is reasonably well understood. However, the magnitude of the nonradiative rate is not, and cannot be calculated with any accuracy except in the weak-coupling case. The reason for this is that the temperature dependence stems from the phonon statistics which is known. However, the physical processes are not accurately known. Especially the deviation from parabolic behavior in the configurational coordinate diagram (anharmonicity) may influence the nonradiative rate with many powers of ten (*11*).

For transitions between $4f^n$ levels, the temperature dependence of the nonradiative rate is given by

$$W(T) = W(0)\,(n + 1)^p \tag{7}$$

where $W(T)$ is the rate at temperature T, $p = \Delta E/\hbar\omega$, ΔE the energy difference between the levels involved, and

$$n = [\exp(\hbar\omega/kT) - 1]^{-1} \tag{8}$$

$W(T)$ is large for low p, that is, for small ΔE or high vibrational frequencies. Further

$$W = \beta \exp[-(\Delta E - 2\hbar\omega_{max})\,\alpha] \tag{9}$$

with α and β constants and ω_{max} the highest available vibrational frequency of the surroundings of the rare-earth ion. This is the energy-gap law in the revised form of Van Dijk and Schuurmans (*12*) that makes it possible to calculate W with an accuracy of one order of magnitude.

B. Energy Transfer (Förster–Dexter Model)

If luminescent centers come closer together, they may show interaction with each other that results in new phenomena. Consider two centers, S and A, with a certain interaction. The relaxed-excited state of S may transfer its energy to A. This energy transfer has been treated by Förster and Dexter and is now well understood (*8*).

Dexter, following the classic work by Förster, considered energy transfer between a donor (or a sensitizer) S and an acceptor (or activator) A in a solid. This process occurs if the energy difference between the ground and excited states of S and A are equal (resonance condition) and if a suitable interaction between both systems exists. The interaction may be either an exchange interaction (if we have wave function overlap) or an electric or magnetic multipolar interaction. In practice the resonance condition can be tested by considering the spectral overlap of the S emission and the A absorption spectra. The Dexter result looks as follows:

$$P_{12} = \frac{2\pi}{\hbar} |\langle 1,2^*|H_{SA}|1^*, 2\rangle|^2 \int g_S(E) g_A(E)\, dE \tag{10}$$

Here the integral represents the spectral overlap, H_{SA} the interaction Hamiltonian and $|j\rangle$ and $|j^*\rangle$ are the electronic ground- and excited-state functions, respectively, with $j = 1,2$. Here 1 refers to S and 2 to A. The distance dependence depends on the interaction mechanism.

A high transfer rate (i.e., a high value of P_{12}) requires a considerable amount of

a. resonance, that is, the S emission band should overlap spectrally the A absorption band(s);

b. interaction, which may be of the multipole-multipole type or of the exchange type.

Not always all of the excitation energy is transferred. If only part of it is transferred, this is called cross-relaxation (*13, 14*). Let us consider some examples. The higher energy level emissions of Tb^{3+} and Eu^{3+} (Fig. 6) can also be quenched if the concentration is high. The following cross-relaxations may occur (compare Fig. 6):

$$Tb^{3+}(^5D_3) + Tb^{3+}(^7F_6) \rightarrow Tb^{3+}(^5D_4) + Tb^{3+}(^7F_0) \quad (11)$$

$$Eu^{3+}(^5D_1) + Eu^{3+}(^7F_0) \rightarrow Eu^{3+}(^5D_0) + Eu^{3+}(^7F_3) \quad (12)$$

The higher energy level emission is quenched in favor of the lower energy level emission.

Such processes can be nicely investigated by laser spectroscopy. Here we mention the example of $^5D_3$ - $^5D_4$ cross relaxation in Tb^{3+} in α-GdOF

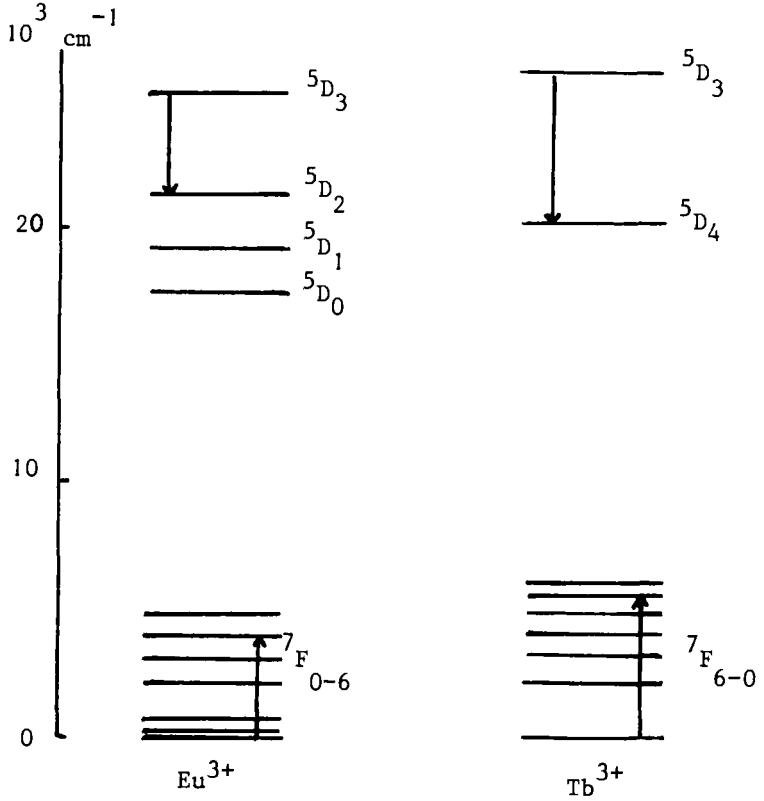

FIG. 6. Cross relaxation in Eu^{3+} and Tb^{3+}.

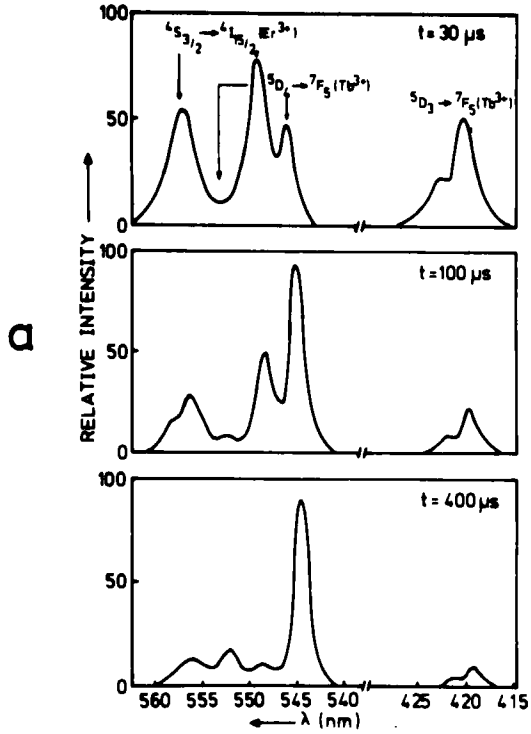

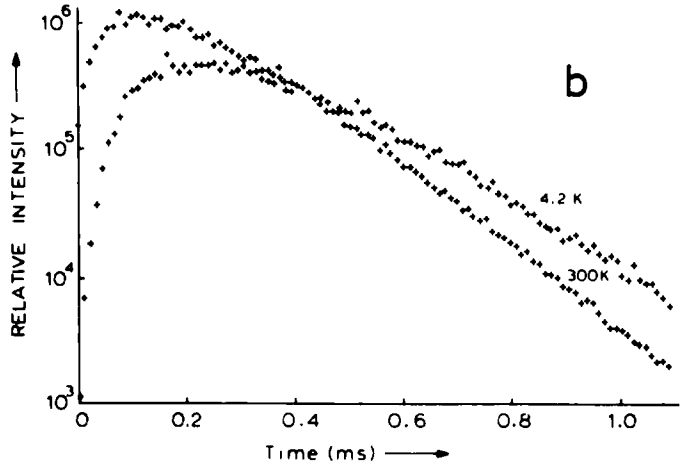

FIG. 7. (a) Time resolution of the Tb^{3+} emission of GdOF:Tb upon $^5D_3$ excitation at 4.2 K. The time after excitation is indicated by t. (b) $^5D_4$ decay curves of GdOF:Tb under the same conditions. Note the build-up. (After M. J. J. Lammers, thesis, Utrecht, 1986.)

(*15*). Multiphonon emission is a very improbable process in this case, since the energy difference between the $^5D_3$ and $^5D_4$ levels is about 5500 cm^{-1}, whereas the phonon cutoff frequency in α-GdOF is smaller than 500 cm^{-1} (i.e., $p \geq 11$). Figure 7 shows the time dependence of the Tb^{3+} emission spectrum after excitation into the $^5D_3$ level of Tb^{3+}. At 30 μs after the pulse the $^5D_3$ emission intensity is higher than the $^5D_4$ emission intensity (the picture is obscured by a certain amount of Er^{3+} emission, since Er^{3+} is present as an impurity); after longer times the $^5D_4$ emission intensity is much stronger than that of the $^5D_3$ emission. Actually the Tb^{3+} $^5D_4$ decay curves show a build-up (see Fig. 7). This shows that the population of the $^5D_4$ level occurs by $^5D_3$-$^5D_4$ cross relaxation. An analysis of these data yields the following results: the cross-relaxation process occurs by electric dipole-dipole interaction over a distance of 10 Å (value at 300 K). This process is temperature dependent, since at 4.2 K the transfer distance is less (8.5 Å). Since the Tb^{3+} ions are statistically distributed over the Gd^{3+} sublattice, the analysis contains a statistical averaging over all the interacting Tb^{3+}–Tb^{3+} pairs with different distances (Inokuti–Hirayama, ref. *8*).

Therefore this type of research is presently directed toward pairs of ions with a given distance. This can be done applying site-selective laser spectroscopy with high resolving power, so that ions with slightly different surroundings are excited selectively. An example is the study of LaF_3–Pr^{3+} by Vial and Buisson (*16*).

If we consider now transfer between two identical ions, for example between S and S, the same considerations can be used. If transfer between two S ions occurs with a high rate, what will happen in a lattice of S ions, for example in a compound of S? There is no reason why the transfer should be restricted to one step, so that we expect that the first transfer step is followed by many others. This can bring the excitation energy far from the site where the absorption took place: energy migration. If in this way the excitation energy reaches a site where it is lost nonradiatively (a killer or quenching site), the luminescence efficiency of that composition will be low. This phenomenon is called concentration quenching (*17*). This type of quenching will not occur at low concentrations, because then the average distance between the S ions is so large that the migration is hampered and the killers not reached.

Energy migration in concentrated systems has been an issue of research in the last decade. Especially since lasers became easily available, the progress has been great. In Section VIII we will first consider the case that S is an ion to which the weak-coupling scheme applies. In practice this case consists of the trivalent rare earth ions. Subsequently we will deal with the case where S is an ion to which the intermediate- or strong-coupling scheme applies.

III. Radiative Transitions: New Results

The field of inorganic electronic spectroscopy has been extensively reviewed (see, for example, ref *18*). In view of the amount of research already performed, one might wonder whether new transitions or known transitions located at deviating spectral positions can still be found. That this is indeed the case will be illustrated in this section. The selection of topics is not complete, but dictated by the author's interest and experience.

A. Infrared Emission from Transition-Metal Ions

Güdel and coworkers have reported during recent years many cases of (near)infrared emission from several transition-metal ions. This was only possible by the use of suitable detectors of radiation (e.g., a cooled germanium photodetector) and careful crystal synthesis. Here we mention some examples.

Compositions $CsMg_{1-x}Ni_xCl_3$ show emission at about 5000 cm^{-1} (*19*). The emission band shows vibrational structure yielding an S value of about 2.5. From this value ΔQ is found to be 0.7 Å, which gives $\Delta r = 0.24$ Å for the change in the Ni–Cl distance. This emission is due to a transition from one of the crystal-field components of the first excited state $^3T_{2g}$ to the $^3A_{2g}$ ground state ($3d^8$, O_h notation). The lifetime of the excited state is 5.2 ms. The luminescence is quenched above 200 K.

In the analogous bromide system S, ΔQ, and Δr are larger than in the chloride system; the Stokes shift is also larger, but the quenching temperature of the luminescence is lower, in agreement with the arguments given in Section II,A.

The properties of $V^{2+}(3d^3)$ were investigated in a.o $MgCl_2$ (*20*). The emission is due to the $^4T_2 \rightarrow {}^4A_2$ transition and is situated at about 7000 cm^{-1}. Vibrational structure yields S values of about 5. The excited state appears to be distorted (Jahn–Teller effect, see below). Above 250 K the emission is quenched.

Also V^{3+} ($3d^2$) shows luminescence, for example in Al_2O_3 and YP_3O_9 (*21*). Even more impressive is a study of the isoelectronic Ti^{2+} ion in $MgCl_2$ (*22, 23*). The infrared emission is due to the $^1T_{2g} \rightarrow {}^3T_{1g}$ transition (O_h notation) around 7000 cm^{-1}, but there is also a visible emission from the $^3T_{1g}$ level.

The spin-forbidden transition shows an analogy with the ruby R lines. The lifetime of the emitting state is the longest-lived *d-d* luminescence (viz., 109 ms!). This is due to the weak spin-orbit coupling. The

orbital degeneracy of the ground state leads to a great deal of structure in the emission spectrum (see Fig. 8).

By codoping $MgCl_2$ with Ti^{2+} and Mn^{2+} the authors were also able to study clusters like $Ti^{2+}Mn^{2+}$ and $Mn^{2+}Ti^{2+}Mn^{2+}$. This is possible by applying site-selective dye-laser spectroscopy. The exchange interactions in these clusters are considerable. Figure 9 shows a schematic diagram of excitation, energy transfer, and luminescence in such clusters. The long lifetime mentioned above is reduced by two orders of magnitude (exchange induced intensity in the singlet-triplet transition).

In connection with transition-metal infrared emission, a recent report of $3d$ Cu^{2+} luminescence must be mentioned. Dubicki et al. (*24*) have investigated crystals with composition $KCu_{0.01}Zn_{0.99}F_3$ and $K_2Cu_{0.01}Zn_{0.99}F_4$ and observed $^2T_{2g} \rightarrow {}^2E_g$ Cu^{2+} emission with magnetic-dipole zero-phenon lines at 6830 and 7498 cm^{-1}, respectively. The low-temperature lifetimes are of the order of 1 μs. It turns out that the spin-orbit coupling quenches the Jahn–Teller coupling in the excited state, so that the emitting $^2T_{2g}$ state has octahedral geometry. The final state is the lower level of the Jahn–Teller split ^2E_g state. In $Ba_2ZnF_6:Cu^{2+}$ Matthies et al. (*25*) observed visible luminescence. This has been ascribed tentatively to a charge-transfer transition in a Cu^{2+}–O^{2-} impurity.

B. Mn^{3+} Emission

Luminescence of the more common ions of the transition metals is well-known, Mn^{2+} and Cr^{3+} being notable examples. For Mn^{3+} ($3d^4$) there are practically no reports in the literature on possible lumines-

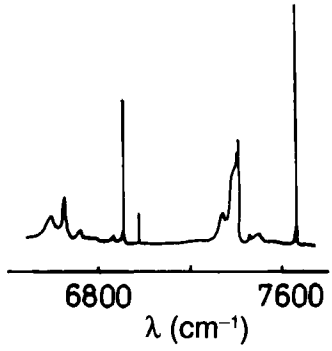

FIG. 8. Emission spectra of $MgCl_2:Ti^{2+}$ at low temperatures. (Adapted from ref. *22*.)

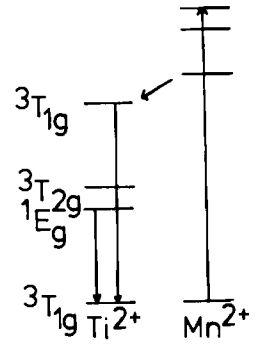

FIG. 9. $Mn^{2+} \rightarrow Ti^{2+}$ energy transfer in Mn^{2+}–Ti^{2+} pairs in $MgCl_2$:Mn^{2+}, Ti^{2+}.

cence. Recently Faber et al. (*26*) reported Mn^{3+} luminescence at low temperatures in a borate glass. It consists of a broad band with a maximum at about 12,000 cm^{-1} (see Fig. 10). The emission is ascribed to the spin-forbidden transition $^3T_1$–^5E (Fig. 11), in agreement with the long decay time of 1.7 ms. In crystalline solids this emission has not been observed for well-known hosts like Al_2O_3, $ZnAl_2O_4$, and $LaA10_3$ (*27*). However, for $Y_3Al_5O_{12}$ it has been observed (*28*), even at 300 K, which seems an exceptional situation. This has been ascribed to the Jahn–Teller effect, which is acting on the ground state.

C. The Lanthanide Ions

The absorption and emission spectra of the rare earths ions are well known (*29*). Recently Carnall et al. (*30*) have given an extended review on the spectra and the calculation of the energy levels of the trivalent lanthanide ions in LaF_3.

Although there is a lot of interesting spectroscopy on these ions going on (see below), reports on new (i.e., up till now unobserved) transitions have become rather scarce. Here we mention two cases that were both made possible by using untrivial techniques.

Szczurek and Schlesinger (*31*) have reported all the $4f^n \rightarrow 4f^{n-1}5^d$ absorption transitions for the trivalent rare earth ions in CaF_2. For the greater part these are in the vacuum ultraviolet. These transitions show a rich vibrational structure. The position of the lowest zero-phonon line varies from 31,923 cm^{-1} (Ce^{3+}, $4f^1$) to 77,760 cm^{-1} (Gd^{3+}, $4f^7$). Using these spectra we were able to find the position of the Eu^{3+}–F^- charge-transfer transition: 66,000 cm^{-1} (*32*).

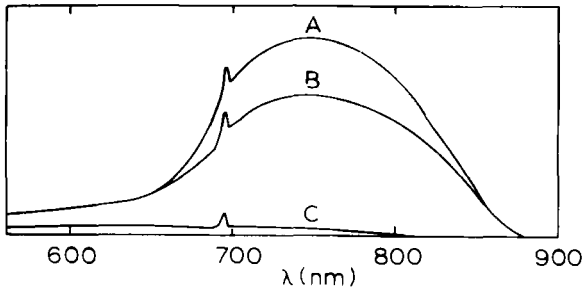

FIG. 10. Emission spectrum of Mn^{3+} in potassium borate glass at 4.2 K (a), 50 K (b), and 300 K (c). The peak emission near 700 nm is due to Mn^{4+}. (After A. van Die, Thesis, Utrecht, 1987.)

Heretofore unobserved transitions within the $4f^n$ shell have been reported for Gd^{3+} ($4f^7$) by Brixner and Blasse (*33, 34*) using X-ray excitation. Figure 12 shows the emission spectrum of GdF_3. There are emission transitions from the ^6P, ^6I, ^6D, and even ^6G levels, the latter at 205 nm. For comparison Fig. 13 gives the energy-level diagram of Gd^{3+}. In certain compositions there was even an emission line at 186 nm, viz., in YBO_3:Gd, Y_2O_3:Gd, YPO_4:Gd, and some others. This is the highest narrow emission line for $4f^n$ configurations reported up till now. It was ascribed to a $J = 3/2$ level, which in LaF_3:Gd is situated at 53,754 cm^{-1} with an energy gap to the next lower level of some 1000 cm^{-1}.

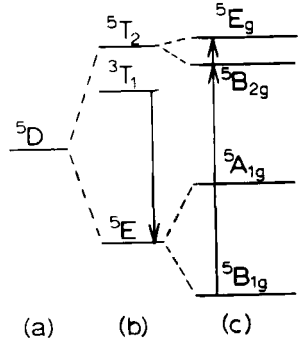

FIG. 11. Energy level scheme of Mn^{3+} ($3d^4$): (a) free ion, (b) octahedral field, (c) Jahn–Teller splitting.

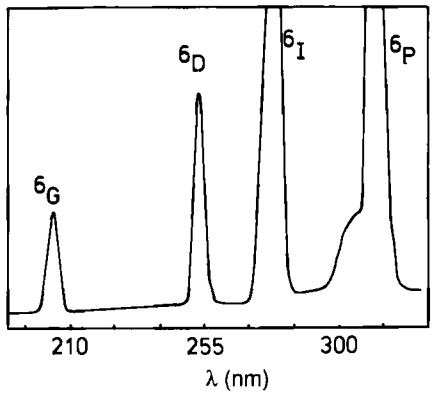

FIG. 12. X-ray excited emission spectrum of GdF_3 at 300 K. Note higher-level emissions.

D. TWO-PHOTON SPECTROSCOPY

Extremely interesting results were obtained for Mn^{4+} in $Cs_2GeF_6:Mn^{4+}$ by McClure et al. by using two-photon spectroscopy (*35*). Although this involves only absorption spectroscopy, the results are mentioned here because they are of interest for the understanding of ion-lattice coupling. The MnF_6^{2-} octahedron in Cs_2GeF_6 has perfect octahedral symmetry. The transitions within the $3d^3$ shell are parity forbidden for one-photon spectroscopy, resulting in very weak zero-phonon lines and strong vibronics due to coupling with *ungerade* vibrations (false origins). In two-photon spectroscopy the zero-phonon lines

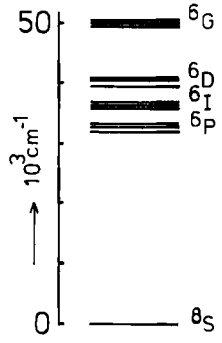

FIG. 13. Energy level scheme of the Gd^{3+} ($4f^7$) ion.

are allowed and are expected to dominate. This makes a complete analysis of the vibrational structure possible without complications. Here we mention only a few results.

The $^4A_2 \rightarrow {}^2E$ transition (the reverse of the emission transition) shows that the expansion in the ^2E level is only 0.003 Å (weak-coupling scheme). The $^4A_2 \rightarrow {}^4T_2$ transition shows that for the $^4T_2$ level this expansion is much larger (viz., 0.053 Å), and S = 3 (intermediate coupling scheme). However, there is not only coupling with the ν_1 (a_{1g}) mode, but also with e_g and t_{2g} (Jahn–Teller active modes). This is even more pronounced in the $^4A_2 \rightarrow a^4T_{1g}$ transition, which shows a clear progression in e_g with a maximum intensity at the fifth member of the progression. The corresponding value of S for this mode is 5. This shows that in the excited a^4T_{1g} state there occurs a large Jahn–Teller distortion (see below).

Let us now consider more-than-one-photon excitation of rare-earth luminescence, a topic that is now being studied intensively. By way of introduction we will consider a two-photon excitation experiment on La_2O_2S-Tm^{3+} (*36*).

The energy level diagram of Tm^{3+} ($4f^{12}$) is given in Figure 14. However, the host lattice shows absorption above 35,000 cm^{-1}, which makes direct observation of the Tm^{3+} levels above 35,000 cm^{-1} by one-photon spectroscopy impossible. Figure 15a shows a two-photon excitation spectrum. This was obtained by monitoring the $^1D_2 \rightarrow {}^3H_6$ emission (27,400 cm^{-1}). The excitation region (20,500–22,500 cm^{-1}) is at lower energy and was scanned with a tunable dye laser. This suggests

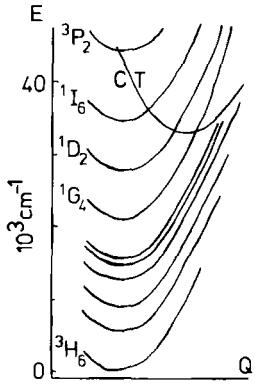

FIG. 14. Energy level scheme of the Tm^{3+} ($4f^{12}$) ion in La_2O_2S. Energy E in 10^3 cm^{-1}. Host lattice absorption starts at 35,000 cm^{-1}.

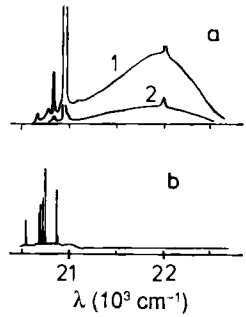

FIG. 15. (a) Two-photon excitation spectrum of La_2O_2S–Tm^{3+} at 4.2 K. Emission: $^1D_2 \rightarrow {}^3H_6$ (27,400 cm^{-1}). Curve 2: 50% reduction in excitation intensity. (b) One-photon excitation spectrum of the $^1G_4 \rightarrow {}^3H_4$ emission.

that we are dealing with two-photon excitation, which is confirmed by the fact that a reduction of the excitation energy by a factor of two results in a reduction of emission intensity of a factor of four.

The features around 20,700 cm^{-1} occur also in the one-photon excitation spectrum of the $^1G_4 \rightarrow {}^3H_4$ emission (see Fig. 15b) and are due to the $^1G_4$ level. In the two-photon excitation spectrum they correspond to a two-step excitation process that uses the $^1G_4$ level as an intermediate level. The sharp peak at 22,000 cm^{-1} has no analogue in the one-photon excitation spectrum. It corresponds to two-photon excitation of the $^3P_2$ level at 44,000 cm^{-1} without any intermediate level. Note the essential difference between these two excitation processes, viz., with and without an intermediary level, respectively.

The broad band points to the presence of a state originating from a different configuration (most probably a charge-transfer state). It is reached by direct two-photon absorption and feeds the $^1D_2$ level from which the emission is monitored.

This experiment teaches us that the energy-level structure of an ion in a host lattice, the absorption of which covers the higher part of the energy levels of the dopant ion, can be unraveled by two-photon spectroscopy. It shows also that two-photon excitation may occur via an intermediate level or directly. Our discussion continues now with the latter case.

The most thoroughly studied case in this category is $4f^7$, viz., Gd^{3+} in LaF_3 and aqueous solution (*37*) and Eu^{2+} in CaF_2 and SrF_2 (*38*) by Downer et al. Figure 13 shows the energy level diagram of Gd^{3+}. Two-photon transitions were studied between the ground state ($4f^7$) $^8S_{7/2}$ and the levels in Fig. 13 (^6P_J, ^6I_J, ^6D_J). Configurations different

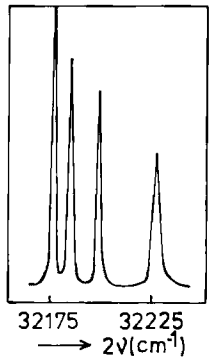

FIG. 16. Two-photon excitation spectrum of the Gd^{3+} emission in LaF_3. The transition involved is $^8S_{7/2} \rightarrow {}^6P_{7/2}$.

from the $4f^7$ configuration lie above 78,000 cm^{-1}. The UV luminescence from the ^6P_J, ^6I_J, and ^6D_J levels was monitored for two-photon excitation by a tunable dye laser. As an example Fig. 16 shows the excitation spectrum around 16,000 cm^{-1} for the $^8S_{7/2} \rightarrow {}^6P_{7/2}$ transition of Gd^{3+} in LaF_3. The crystalline field of Gd^{3+} in LaF_3 has split the $^6P_{7/2}$ level into four components.

Downer et al. have derived a theory that can account for the observed intensities quantitatively, following an earlier approach by Judd and Pooler (*39*).

The results for Eu^{2+} in CaF_2 and SrF_2 are even more interesting, since the excited $4f^7$ levels cannot be observed by single-photon spectroscopy due to the overlap by the $4f^6 5d$ band. At the same time, the lower position of the $4f^6 5d$ states for Eu^{2+} relative to Gd^{3+} increases the absolute two-photon absorption strength.

More two-photon transitions without intermediate state have been reported in the literature. Here we mention the $^3H_4 \rightarrow {}^1S_0$ transition of Pr^{3+} by Bloembergen et al. (*39*). The $^1S_0$ level is at about 47,000 cm^{-1} above the $^3H_4$ ground state level. It is also far above the one-but-highest level of the $4f^2$ configuration of Pr^{3+} ($^3P_2$ at about 23,000 cm^{-1}). Experimentally the two-photon excitation spectrum of the $^1S_0 \rightarrow {}^1G_4$ and $^3F_4$ emission is monitored. Figure 17 shows this spectrum, together with the luminescence intensity dependence on the exciting laser beam intensity (quadratical). These data are for $LaCl_3$, where the $^1S_0$ level is inaccessible for one-photon spectroscopy due to the fact that it is overlapped by the $4f5d$ configuration.

A different example is the $4f \rightarrow 5d$ two-photon transition of Ce^{3+} ($4f^1$), which is electric-dipole forbidden (*40*). It is possible to measure the

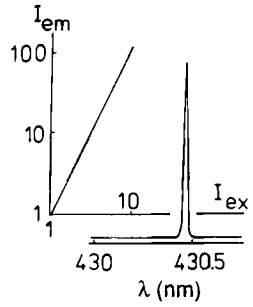

FIG. 17. Two-photon excitation spectrum of the $^1S_0$ emission of Pr^{3+} in $LaCl_3$. Note the quadratic dependence on excitation intensity.

one- as well as the two-photon excitation spectrum of the $d \rightarrow f$ emission. The spectra are very similar. The measurements were performed on Ce^{3+} in CaF_2 where the Ce^{3+} site symmetry is C_{4v}; that is, it lacks inversion symmetry. The odd component V_u mixes states of opposite parity and determines the strength of the zero-phonon line of the two-photon transitions. The absorption cross section of the zero-phonon line was found to be $5 \cdot 10^{-54}$ cm^4 sec. Typical values for allowed transitions are 10^{-49}–10^{-51} cm^4 sec. Note the similarity between the intraconfigurational transitions in one-photon spectroscopy and the interconfigurational transitions in two-photon spectroscopy. Both are parity forbidden, but can gain intensity by configuration mixing due to the presence of an uneven crystal field potential.

Let us now turn to two-photon excitation via an intermediary level. In this chapter we restrict ourselves to processes without energy transfer, that is, typical one-ion processes. A recent and "intensity-rich" example is Eu^{3+} in LaOCl (*41*). Excitation of the $^5D_0$ level of Eu^{3+} (cf. Fig. 6) does not only yield the usual emission transitions from the $^5D_0$ level, but also yields anti-Stokes emission from the higher $^5D_{1,2,3}$ levels. The intensities of these emissions were at least one order of magnitude smaller (for excitation with a continuous dye laser pumped with an argon ion laser).

The excitation mechanism of the anti-Stokes emission is as follows. First the ion is excited into the $^5D_0$ level. Although the $^7F_0$–$^5D_0$ transition is highly forbidden ($J = 0 \rightarrow J = 0$), it has a rather high absorption strength in LaOCl due to the strong linear crystal-field component at the $La^{3+}(Eu^{3+})$ site. The lifetime of the $^5D_0$ level is long (of the order of milliseconds). A second photon is now absorbed, which raises the system to the charge-transfer state. This is an allowed transition. More-

over, in LaOCl this charge-transfer state of the Eu^{3+}–oxychloride complex is at an energy about twice that of the $^5D_0$ level. Then the system relaxes rapidly to the ^5D levels, resulting in emission from the various ^5D levels. The absorption of the first photon is the rate-determining step in the whole process.

A similar process has been described by Boulon et al. (*42*) for Gd^{3+}. These authors observed, on pumping into the first excited level $^6P_{7/2}$ at 311.5 nm, an anti-Stokes emission from the $^6I_{7/2}$ level at 278.9 nm (cf. Fig. 13).

If we consider, under comparable excitation energy, the two-photon excitation processes without and with an intermediate level, the one with an intermediary level is several orders of magnitude more intense. The physical interpretation of this observation is that photons travel fast, so that their energies are only available in the medium during a time that is very short in comparison with the lifetime of the intermediary state (*43*).

The two-photon excitation process using an intermediary level has also been observed in the reverse way; that is, excitation by a one-photon process is followed by emission of two photons. These are emitted subsequently. A well-known example is Pr^{3+} ($4f^2$) (*44*). With short-wavelength UV excitation this ion can be brought into the highest level of the $4f^2$ configuration, viz., $^1S_0$. The radiative return to the ground state occurs in two steps (allowing a maximum quantum efficiency of 200%). The first step is $^1S_0 \rightarrow {}^3P_2$ and/or $^1S_0 \rightarrow {}^1I_6$ (blue emission); the second step consists of the usual radiative transitions from the $^3P_0$ level (green and red emission). This phenomenon can be described as two-photon emission (using an intermediate state).

The process of excited state absorption involving broad bands is another type of radiative transition that has become of great interest during recent years. By using laser excitation it is possible to achieve significant excited state population, making it possible to study excited state absorption. The study of this phenomenon in solids has received a strong impetus because excited state absorption is a detrimental factor that reduces the pumping efficiency of solid state lasers drastically, if it does not inhibit laser action completely. For this loss to occur it is necessary that the excited state absorption spectrum overlaps the emission spectrum. The possibilities for overlap are especially enhanced in solids with broad absorption and emission bands. An example of the deleterious role of excited state absorption is $Y_3Al_5O_{12}$:Ce (*45*), where laser action is completely quenched. Figure 18 shows the ground state absorption spectrum of $Y_3Al_5O_{12}$:Ce($4f^1$). The lower bands are due to allowed $4f \rightarrow 5d$ transitions on Ce^{3+}. The broad emission band extends

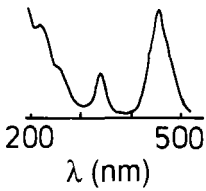

FIG. 18. The ground state absorption spectrum of $Y_3Al_5O_{12}$–Ce^{3+}.

from 500 to 650 nm. Figure 19 shows the excited state absorption spectrum. The oscillator strength of this transition is 0.03. Finally Fig. 20 shows the energy levels of the Ce^{3+} ion in $Y_3Al_5O_{12}$ relative to the valence and conduction band of the host lattice.

The excited state absorption starts on the lower 5*d* level and ends on a level in the conduction band. Therefore this two photon transition results in photoionization of the Ce^{3+} ion. The conduction band minimum lies only 10,000 cm^{-1} above the lowest (relaxed) 5*d* level. The higher energy part of the ground state absorption spectrum ($\lambda <$ 300 nm in Fig. 18) is due to direct (one-photon) photoionization of the Ce^{3+} ion. The excited state absorption of Ce^{3+} is strongly host dependent. In CaF_2:Ce^{3+} and $LiYF_4$:Ce^{3+} it is situated in the near ultraviolet (*46, 47*).

Photoionization of other rare-earth ions (Eu^{2+}, Sm^{2+}) has been reported by Pedrini et al. (*48*). They were able to detect the charge carriers in the conduction by photoconductivity measurements.

Since Cr^{3+} is used as an ion in tunable near-infrared lasers, much work has also been done on the excited-state absorption of the Cr^{3+} ion in lattices where the $^4T_2$ level is situated below the ^2E level (see, e.g., *49*). Due to the Jahn–Teller effect a complicated situation arises. It is now possible to suggest criteria for choosing Cr^{3+} hosts for which the effect of excited state absorption is minimized. These criteria are a large

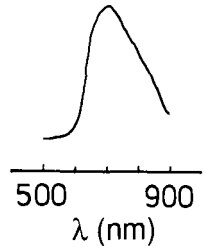

FIG. 19. The excited state absorption spectrum of $Y_3Al_5O_{12}$–Ce^{3+}.

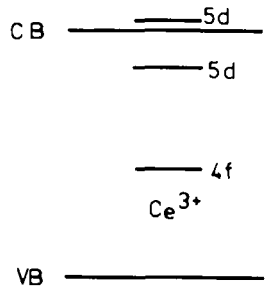

FIG. 20. Energy level scheme of $Y_3Al_5O_{12}$–Ce^{3+}. VB: valence band; CB: conduction band. (Figures 18–20 after data in ref. *45*.)

crystal field, a small substitutional site, and a crystal with high phonon frequencies (*49*).

Time-resolved excited-state absorption of Mn^{2+} in the spinel $MgAl_2O_4$ has been reported by Petermann et al. (*50*). Several types of excited state absorption transitions have been observed and can be understood in terms of a configurational coordinate mode. As a consequence the Mn^{2+} ion cannot lase in the spinel lattice.

E. CHARGE-TRANSFER TRANSITIONS

From a chemical point of view charge-transfer transitions are intriguing and interesting, since they bring about large changes in the chemical bond and strong coloring of the sample under study. The spectra consist of very broad bands that do not reveal much information due to the absence of vibrational structure. These transitions are clear-cut examples of the strong-coupling case.

The charge-transfer (CT) transitions can be of the metal-to-ligand or of the ligand-to-metal type (MLCT or LMCT, respectively). They have been discussed extensively in the literature (*18, 51*). To this we would like to add the following.

Broadband transitions on Cu(I) have long been known. They span a wide range in the ultraviolet and visible spectrum, depending on the nature of the ligands. Often they give rise to efficient emission after excitation in the broad absorption bands. In Table I we have summarized data on a large number of Cu(I) species. (Figure 21 gives a few examples of spectra). These range from pronounced ionic cases (top) to very covalent situations or semiconductors (bottom). At first sight the regular variation suggests that the optical transition involved is of the

TABLE I

SOME SPECTRAL DATA ON Cu(I) COMPLEXES[a]

Species[b]	Maximum absorption band	Maximum emission band	Reference
$CuCl_3^{2-}$ (solution)	37	21	*60*
Cu^+ in SiO_2 glass	38.5	20	*61*
$LiSrPO_4$:Cu^+ (s)	~37	24	*62*
Cu^+ in phosphate glass	37	23	*63*
Cu^+ in SiO_2 glass	37	23	*61*
NaCl:Cu^+ (s)	36	29	*64*
Cu^+ monomer in β''-alumia (s)	-	23	*65*
$Sr_3(PO_4)_2$:Cu^+ (s)	~33	22	*62*
Cu(I) in $(CuS)_3$ cluster (m)	28.5	21	*66*
CuJ-pyridine (m)	27	17	*67*
Cu^+ pairs in β''-alumina	-	19	*65*
$[Cu(PPh_3)_2(phen)]^+$ (m)	25	18.5	*68*
$CuLaO_2$ (s)	25	18	*54*
Cu(I) in $(CuS)_3$ cluster (m)	25	16	*66*
Cu_2O (s)	17.5	-	*69*
Cu_2WO_4 (s)	~17	-	*70*
$CuNbO_3$ (s)	~17	-	*71*
$CuInS_2$ (s)	12	-	*72*
Cu_2S (s)	10	-	*73*

[a] All values are 10^3 cm^{-1}.
[b] s, Solid; m, molecular.

same type for all Cu(I) species. However, this does not seem likely. The literature discusses these transitions in different ways.

The ionic case [e.g., NaCl:Cu(I)] is discussed in terms of transitions corresponding to an interconfigurational transition $d^{10} \rightarrow d^9s$ and d^9p on the copper ion. Quantitative calculations are available (*52*).

For more covalent cases, like $[Cu(P\,Ph_3)_2\,(phen)]^+$ and Cu_2WO_4, a MLCT description seems to be more appropriate (*53*). Actually the

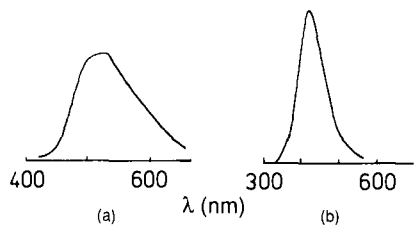

FIG. 21. The emission spectra of (a) $[Cu(PPh_3)_2(phen)]^+$ and (b) Cu^+ in $LiSrPO_4$.

$d^{10} \rightarrow d^9s$ description contains some MLCT character due to the diffuseness of the 4*s* orbital.

For the sulfur ligands a LMCT is obvious. This implies that for the cases given in Table I different descriptions are used. Whether this is really a correct approach can only be decided when quantitative calculations are available for several cases. In ref. *54* the transitions in $CuLaO_2$ are described as $d^{10} \rightarrow d^9s$ transitions. It will be clear that Table I throws some doubt on this model. This compound is in our opinion an example of a Cu(I) complex, which can be described by any of the three given descriptions.

An interesting general consideration on charge-transfer transitions has been given by McGlynn et al. (*55*). This relates immediately to the color of a large number of inorganic salts. The authors consider configurational interaction of several excited states in the following way. Consider the simple system M^+A^-. The ground configuration is written $\Psi_G = \psi(M^+A^-)$. Two excited configurations are the charge-transfer configuration $\psi_{CT} = \psi(MA)$ and the ligand-excited (LE) configuration $\psi_{LE} = \psi\{M^+(A^-)^*\}$. The excited state can be written as $\psi_E = a\psi_{LE} + b\psi_{CT}$. Figure 22 shows how the energy of the excited levels varies as a function of the ratio a^2/b^2.

The lowest absorption (and the emission) transition is ligand localized on the right-hand side and charge transfer on the left-hand side of Fig. 22. In between is an intermediate region. Since the excited states are open shell, spin-singlets and spin-triplets appear. This simple approximation can be extended by including more excited configurations,

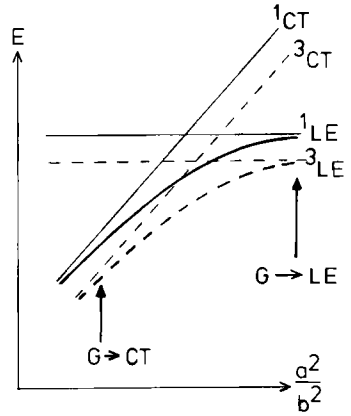

FIG. 22. Interaction of ^{1}CT/^{1}LE and ^{3}CT/^{3}LE states leading to extreme and intermediate mixing cases (see also text).

for example, back-CT [$\psi(M^{2+}A^{2-})$] and a metal-ion excited configuration [$\psi|(M^{+})^{*}A^{-}|$].

This approach accounts for a shift of the first absorption transition to lower energies than expected, or to a gain in intensity of spin-forbidden transition. Here we give an example of the latter. The nitrite ion is colorless. However, $Pb(NO_2)_2$ is strongly orange colored. The singlet-triplet transition of NO_2^- is in the visible region but is very weak. The CT mixing, although not large, enhances the weak intensity with a factor 100 if one compares $NaNO_2$ and $Pb(NO_2)_2$ (*56*). This is due to the large spin-orbit coupling of lead.

We conclude that slowly the insight in charge-transfer transitions is increasing, but that still much work has to be done to obtain a complete picture. In this the metal-to-metal (for example, Bi_3ReO_8, *57*) and mixed-valence charge-transfer transitions should also find a place (*58, 59*).

F. Cross-over Transitions

Recently there has been a lot of interest in the luminescence of BaF_2. Its crystals have a large potential as a scintillator material (detection of gamma rays). They show a luminescence at 220 nm with a very short decay time, viz., 600 ps. This short decay time offers the possibility of a good time resolution. This luminescence is of a new type (cross-over luminescence). Its nature has been unraveled by Russian investigators (*75*). Excitation with about 10 eV excites anion excitons. Upon annihilation these anion excitons show an emission at about 4.1 eV (300 nm). Excitation with about 18 eV excites cation excitons. These do not annihilate in a simple way, but by a so-called cross-over transition: an electron jumps from the F^- ion (2*p* orbital) to the hole in the 5*p* orbital of Ba^{2+} (see Fig. 23). This is accompanied by emission at about 5.7 eV

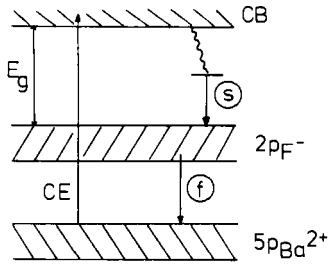

Fig. 23. Energy level scheme of BaF_2 showing cross-over luminescence.

(220 nm) and weaker emissions at even higher energy. Since the energy difference between the $2p$ (F^-) and the $5p$ (Ba^{2+}) energy band is less than the band gap (~10 eV), the corresponding emission is observed as part of the intrinsic emission of BaF_2. The 200-nm emission shows practically no temperature quenching up to room temperature, whereas the 300-nm emission is for the greater part quenched under these conditions.

Other compounds for which this phenomenon has been found are CsCl and CsBr (*76*) and KF, $KMgF_3$, $KCaF_3$, and K_2YF_5 (*77, 78*).

G. Fano Resonance

In the sixties Fano and Cooper (*79*) presented a theoretical explanation for the Beutler bands in the far-UV absorption spectra of rare gasses. Sturge, Guggenheim, and Pryce (*80*) showed that the Fano theory describing the band profile of a broad ionizing continuum in the vicinity of sharp intraatomic transitions could be applied to the situation of an impurity center for which a broad absorption band is overlapped by a sharp absorption line. This type of Fano antiresonance in solid state physics has been observed for two d^3 transition metal ions, viz., V^{2+} by Sturge et al. (*80*) and Cr^{3+} by Lempicki et al. (*81*). The explanation for the antiresonance observed for Cr^{3+} and V^{2+} is based on the interaction between the intra t_2^3 levels (^2E, $^2T_1$, and $^2T_2$) and the t^2e levels ($^4T_2$ and $^4T_1$).

Recently the observation of Fano antiresonance in the excitation spectra of the luminescence of Eu^{2+} was reported (*82*). The two-photon absorption experiments by Downer et al. [*37, 38*], for example, revealed the presence of sharp absorption lines due to transitions from the $^8S_{7/2}$ ground state to the ^6P_J, ^6I_J and ^6D_J states within the $4f^7$ configuration of Eu^{2+}. These parity-forbidden transitions are overlapped by the broad $4f^65d$ absorption bands of Eu^{2+}. For this situation the appearance of Fano antiresonance in the vicinity of the sharp absorption lines is to be expected.

Figure 24 shows the excitation spectra at 4.2 K of the Eu^{2+} emission of strontium bromoborate (*82*). In the spectrum the presence of $4f^65d$ excitation bands can be observed. The lower energetic band, located between some 330 and 400 nm, depending on the host lattice, shows a well-resolved structure due to the splitting of the $4f^6$ configuration in the $4f^65d$ excited state. This has been discussed elsewhere (*83*). The features we are interested in at present are the dips in the excitation spectrum around 320 nm and 295 nm. The positions of these dips coincide with the positions of the ^6I_J and ^6D_J excited states within the

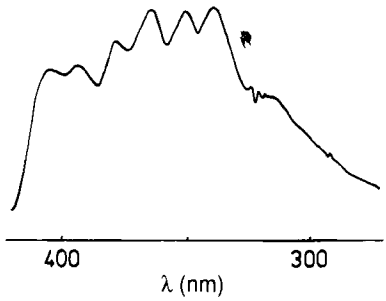

FIG. 24. Fano antiresonance (arrows) in the excitation spectrum of Eu^{2+} in $Sr_2B_5O_9Br$.

$4f^7$ configuration of Eu^{2+}, which have been determined by Downer et al. (*38*). The dips are ascribed to the presence of Fano antiresonance. Note that no dips due to Fano antiresonance are observed at the position of the ^6P_J levels, located around 360 nm. These phenomena have been satisfactorily analyzed (*82*).

H. SMALL PARTICLES

The luminescence of small particles, especially of semiconductors, is a fascinating development in the field of physical chemistry, although it is too early to evaluate the potential of these particles for applications. The essential point is that the physical properties of small semiconductor particles are different from the bulk properties and from the molecular properties. It is generally observed that the optical absorption edge shifts to the blue if the semiconductor particle size decreases. This is ascribed to the quantum size effect. This is most easily understood from the electron-in-a-box model. Due to their spatial confinement the kinetic energy of the electrons increases. This results in a larger band gap (*84*).

As an example we mention here colloids of ZnS. They can be prepared with variable particle size (down to 17-Å diameter, which corresponds to particles containing about 60 molecules of ZnS) (*85*). The onset of the optical absorption shifts from 334 nm (large particles and bulk) to 288 nm (17-Å particles). The particles show luminescence. Also the emission maximum shifts to shorter wavelength if the particle size is decreased (*85*).

A recent, well-defined example of such clusters is the existence of CdS superclusters in zeolites (*86, 87*). The authors prepared very small CdS clusters in zeolites. In zeolite Y, for example, there are sodalite cages (5

Å) and supercages (13 Å). Well-defined clusters can be made using these cages. The zeolites were Cd^{2+}-ion exchanged and subsequently fired in H_2S. The resulting zeolite is white (note that CdS is yellow). The products were characterized by several means. It was shown that CdS is within the zeolite pore structure. There are discrete $(CdS)_4$ cubes in the sodalite cages. The cubes consist of interlocking tetrahedra of Cd and S. For high enough CdS concentrations these clusters are interconnected. As this interconnection proceeds, the absorption spectra shift in band edge from 290 to 360 nm. These materials show luminescence. Three different emissions have been observed, viz., a yellow-green one (ascribed to Cd atoms), a red one (ascribed to sulfur vacancies), and a blue one (ascribed to shallow donors). A very interesting aspect is that the vibrational mode responsible for the nonradiative transitions in these materials has a frequency of 500–600 cm^{-1}. This is higher than the highest phonon frequency in CdS. This indicates that interface and host (zeolite) phonons are responsible for these processes.

An interesting development in this field is the recent report by Dameron et al. (*88*) of the biosynthesis of quantum-sized CdS crystals in the yeast cells Candida glabrata and Schizo saccharomyces pombe. Exposed to Cd^{2+} ions these cells synthesize certain peptides with an enhanced sulfide production. Small CdS crystals are formed inside the cells. These crystallize in the rock salt structure (and not in the thermodynamically stable hexagonal configuration). The organism controls particle nucleation and growth, so that uniformly sized CdS particles of about 20 Å are formed. They show pronounced quantum-size effects. This is the first example of the biosynthesis of quantum-sized semiconductor crystallites. It constitutes a metabolic route for the detoxification of Cd^{2+}-infected living cells (see also *89*).

No doubt these semiconductor superclusters present a novel class of materials where the three-dimensional structure can be controlled. They present a challenge to synthetic and physical chemists.

IV. Nonradiative Transitions: A Qualitative Approach

A. The Weak-Coupling Case

Nonradiative transitions in the weak-coupling approximation are probably the best understood nonradiative processes. The experimental data relate mainly to the rare-earth ions, as far as their sharp-line transitions are considered (i.e., intra-$4f^n$ configuration transitions). The topic has been discussed in many books and review papers (see also above) (*11*, *12*).

Let us illustrate this topic with some results. In aqueous solutions or in hydrates the rare-earth ions do not emit efficiently with the exception of Gd^{3+} ($\Delta E = 32{,}000$ cm^{-1}, $\omega_{max} \simeq 3{,}500$ cm^{-1}). For Tb^{3+} ($\Delta E \simeq 15.000$ cm^{-1}), and especially Eu^{3+} ($\Delta E \simeq 12.000$ cm^{-1}), the quantum efficiencies are depressed, the other rare-earth ions practically do not emit at all (*90*). For solids this can be nicely studied in the host lattice $NaLa(SO_4)_2H_2O$ where the rare-earth site is coordinated to one H_2O molecule only. The q values are as follows (*91*): Gd^{3+}, $q = 100\%$; Tb^{3+}, 70%; Eu^{3+}, 10%; Sm^{3+}, ~1%; Dy^{3+}, ~1%. In the classic oxide glasses the rare-earth ions do not emit efficiently, since $\omega_{max} \simeq 1{,}000$–$1{,}200$ cm^{-1} (silicates, borates, phosphates). Only Gd^{3+}, Tb^{3+}, and Eu^{3+} show efficient luminescence. This situation changes drastically by using fluoride or chalcogenide glasses, where ω_{max} is considerably lower. A very interesting lattice in this connection is $Eu_2Mg_3(NO_3)_{12}\cdot 24H_2O$ (*92*). At first sight the large amount of water molecules is expected to quench the Eu^{3+} emission completely. However, the Eu^{3+} ions are bidentately coordinated by six nitrate ions, which shield them from the water molecules. The quantum efficiency is high.

Ions like Eu^{3+} and Tb^{3+} may emit from higher excited states: Eu^{3+} not only from $^5D_0$ (red), but also from $^5D_1$ (green) and $^5D_2$ (blue). However, this depends critically on the host lattice. In Y_2O_3–Eu^{3+}, for example, all these emission are observed, since $\omega_{max} \simeq 600$ cm^{-1}. In borates and silicates, however, they are not.

This can be well studied by laser spectroscopy. An example is $NaGdTiO_4$:Eu^{3+} (*93*). The time dependence of the Eu^{3+} emission in $NaGdTiO_4$ on excitation into the $^5D_1$ level of Eu^{3+} is as follows: 10 μs after the excitation pulse the emission originates mainly from the $^5D_1$ level, but after longer time the $^5D_1 \rightarrow {}^5D_0$ decay is found to be 1.3×10^4 s^{-1} at 4.2 K. Its temperature dependence is given by $(n + 1)^p$, as argued above. The value of p turns out to be 5, the vibrational frequency involved being 347 cm^{-1}. This corresponds to the Eu–O stretching vibration. At 300 K this nonradiative rate is about 4×10^4 s^{-1}. The values of the nonradiative rate exceed that of the radiative $^5D_1$–^7F_J rate (~10^3 s^{-1}), so that the nonradiative process dominates and the emission occurs mainly from the $^5D_0$ level. In compounds with higher phonon frequencies available (e.g., borates, silicates), the $^5D_1$ emission of Eu^{3+} is usually hardly detectable, since the value of p is then much lower.

The Tb^{3+} ion may not only emit from $^5D_4$ (green), but also from $^5D_3$ (blue). ΔE is about 5000 cm^{-1}, much larger than in the case of Eu^{3+}. Diluted Tb^{3+} systems, therefore, always show some blue Tb^{3+} emission, unless ω_{max} is very high.

We will now pay some attention to an ion that is not studied frequently, viz., Gd^{3+} ($4f^7$). Its energy level scheme is given in Fig. 13. The excited levels are in the ultraviolet, and the corresponding transitions have low oscillator strengths. As a consequence accurate spectroscopy can only be performed with ultraviolet tunable lasers and/or X-ray excitation (for emission). The ground level is orbitally nondegenerate ($^8S_{7/2}$), which is an advantage for several reasons.

The emission transition $^6P_J \rightarrow {}^8S$ occurs over an energy gap of about 32.000 cm^{-1}. Nonradiative transitions cannot compete with this radiative one because it occurs over such a large ΔE. Even water molecules ($\nu \sim 3500$ cm^{-1}) are not able to quench the Gd^{3+} emission (*90*). The emission can only be quenched by transfer to other luminescent centers (*94*).

In some host lattices emission has also been observed from the higher excited levels ^6I_J, ^6D_J, and even ^6G_J (see above). In the case of borates and hydrates, however, all these emissions are quenched in favor of the ^6P_J emission. This is a clear demonstration that higher-frequency vibrations promote the radiationless transitions to the ^6P_J levels.

There is in the literature only one example of a quantitative treatment of these processes, viz., for $LiYF_4$-Gd^{3+} (*95*). The temperature dependence of the $^6I_J \rightarrow {}^6P_J$ nonradiative transition was determined by measuring the decay time of the $^6I_J \rightarrow {}^8S$ emission transition, and could be fitted to the formulas given above.

B. The Strong-Coupling Case

This section starts by illustrating how important the value of the parameter offset is for the nonradiative transition rate. We will use several examples from different fields of chemistry for this purpose.

First we consider $CaWO_4$, an X-ray phosphor well known for seventy years. The luminescent group is the tungstate group (*96*), a pronounced example of a center for which the strong-coupling scheme holds (see also Fig. 4c). $CaWO_4$ is a very efficient material at room temperature. The isomorphous $SrWO_4$, however, does not emit at 300 K, but has to be cooled down in order to reach a reasonable quantum efficiency. $BaWO_4$ also has the same crystal structure, but even at 4.2 K it does not emit with high efficiency. Nevertheless the ground state properties of the tungstate group in these compounds (distances, vibrational frequencies) are practically equal. The strongly different radiationless processes have to be ascribed to a difference in ΔQ (i.e., the parabolas offset). Since the ionic radii of Ca^{2+}, Sr^{2+}, Ba^{2+} decrease in that order, it seems obvious to assume that this is why the offset increases (i.e., why

the rate of the radiationless processes increases) as observed experimentally. The softer the surroundings, the larger is ΔQ.

There is a more impressive experiment to prove this simple model, viz., the luminescence in the ordered perovskites A_2BWO_6 where A and B are alkaline earth ions. Table II presents the quenching temperatures of the luminescence of the UO_6 group in these lattices (*97*). Those for the WO_6 group run parallel (*98*). These temperatures are used as a measure of the radiationless properties. The table shows that the radiationless rate does not depend on the nature of A, whereas the nature of B determines the value of this rate: the smaller the B ion, the higher the quenching temperature.

Figure 25 shows that an expansion of the luminescent UO_6 (or WO_6) octahedron (i.e., the parabolas offset) is not directly counteracted by the A ion. However, the B ions are immediately involved, the angle U(W)–O–B being 180°. Table II also shows relative values of ΔQ calculated from the Struck and Fonger model (*99*). It scales indeed according to predictions. Note that the total change in ΔQ is less than 10%. Since ΔQ is less than 0.1 Å for the uranate group, the variation in ΔQ in this series of compounds is less than 0.01 Å. This shows that small changes in ΔQ result in drastic changes in the nonradiative rates.

It is well known that luminescent materials with high quantum efficiencies and quenching temperatures usually have stiff lattices, so

TABLE II

THERMAL QUENCHING OF THE URANATE LUMINESCENCE OF ORDERED PEROVSKITES A_2BWO_6–U^{6+} [a]

A_2BWO_6–U		T_q(K) [b]	ΔQ(au) [c]
A–Ba	B–Ba	180	10.9
Ba	Sr	240	10.6
Ba	Ca	310	10.2
Ba	Mg	350	10.0
Sr	Mg	350	10.0
Ca	Mg	350	10.0

[a] Data from ref. *97*, cf. Fig. 25.

[b] Quenching temperature of the uranate luminescence.

[c] ΔQ in arbitrary units, calculated by the Struck and Fonger method. ΔQ is given as 10.0 for Ba_2MgWO_6.

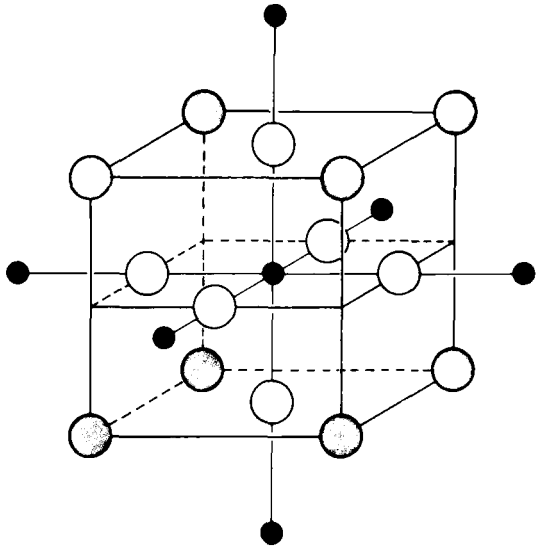

FIG. 25. Part of the crystal structure of ordered perovskite $A_2BW(U)O_6$. Center black ion W(U), other black ions B, white ions O, grey ions A.

that expansion on excitation is counteracted; that is, $\triangle Q$ is as small as possible.

Table III shows for a series of borates how the Stokes shift (i.e., $\triangle Q$) increases if the size of the host lattice cation increases (*100*). In $ScBO_3$ the rare-earth ions are strongly compressed and the surroundings are stiff. Small Stokes shifts result for Ce^{3+}, Pr^{3+}, and Bi^{3+}, but not for the smaller Sb^{3+}. Note, however, that the Stokes shift of the $4f$-$5d$ transitions is less sensitive to the surroundings than that of the $5s$-$5p$ transitions. If the data of Table III are extrapolated to, for example, borate glasses, it can be concluded that we find no efficient Sb^{3+} or Bi^{3+} emission, but for Ce^{3+} or Pr^{3+} this may still be the case. This is what has been observed experimentally.

Part of solid state chemistry is presently involved with what is called soft chemistry or soft materials. As a matter of fact these are not expected to luminescence, at least not when the luminescent centers are broadband emitters. This has been shown to be the case, for example, for the isomorphous $Al_2(WO_4)_3$, $Sc_2(WO_4)_3$, and $Zr_2(PO_4)_2SO_4$. The Stokes shift of the tungstate and zirconate luminescence in these materials is enormous, viz., some 2 eV. The quantum efficiencies, even at 4.2 K are low (*101*). The exact structural explanation has been discussed in the literature (*101*).

TABLE III

STOKES SHIFT (10^3 cm^{-1}) OF THE BAND EMISSION OF SOME TRIVALENT IONS IN THE ORTHOBORATES MBO_3[a]

Ions	$ScBO_3$	YBO_3[b]	$LaBO_3$
$Ce^{3+}(4f^1)$	1.2	2.0	2.4
$Pr^{3+}(4f^2)$	1.5	1.8	3.0
$Sb^{3+}(5s^2)$	7.9	14.5	19.5
		16.0	
$Bi^{3+}(6s^2)$	1.8	5.1	9.3
		7.7	

[a] (M = Sc, Y, La); after ref. *100*.
[b] This lattice contains two sites for Y.

Another interesting phenomenon is the change in luminescence properties if one passes the fluid-liquid transition in a 4:1 ethanol-methanol solution of [(bpy)$Re(CO)_3Cl$] (*102*). The absorption transition is not influenced, but the emission is at longer wavelengths in the liquid; that is, the Stokes shift is larger. This means that ΔQ increases if we go from the fluid to the less rigid liquid state. Simultaneously the quantum efficiency of the luminescence decreases.

This model, in which the nonradiative transitions can be suppressed by a stiff surroundings, can be most elegantly tested by studying the luminescence of rare-earth cryptates (*103–105*).

The cryptand ligands are organic cages. They were synthesized for the first time by Lehn, who obtained the Nobel prize for Chemistry in 1987 for this achievement (together with Cram and Pedersen) (*106*). Figure 26 gives two examples. The 2.2.1 cryptand is just large enough to contain the Ce^{3+} ion; that is, on excitation the Ce^{3+} ion has not much space to expand. In fact the $[Ce \subset 2.2.1]^{3+}$ cryptate shows an efficient (broadband) emission at room temperature with a small Stokes shift, in the solid state as well as in aqueous solution (*103*). The $[Ce \subset 2.2.2]^{3+}$ cryptate luminescence has a much larger Stokes shift. As a matter of fact the 2.2.2 cryptand offers a larger hole than the 2.2.1 cryptand.

Table IV shows the Stokes shift of the Ce^{3+} emission in several surroundings. In the 2.2.1 cryptand the Ce^{3+} Stokes shift is smaller than in some commercial Ce^{3+}-activated phosphors (Y_2SiO_5–Ce, Ca_2AlSiO_7–Ce). It becomes very small in $ScBO_3$ (see above) and in CaF_2 and $CaSO_4$, where it carries an effectively positive charge that will make the Ca site smaller than it is on basis of the Ca^{2+} ionic radius.

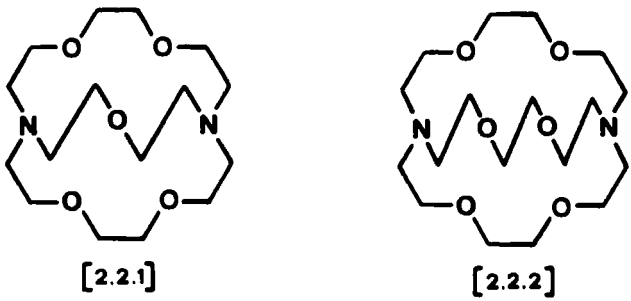

FIG. 26. The 2.2.1 and 2.2.2 cryptands.

In passing we note that the cryptands presently find an important application in the field of medical diagnostics, which is also based on their ability to suppress nonradiative transitions, viz., fluorescence immuno-assay. To detect biomolecules of a special nature, antibodies are used that are labeled with a luminescent ion, for example, Eu^{3+} (*104*), and that react specifically with the biomolecule of interest. The Eu^{3+} luminescence shows where these biomolecules are residing. However, since investigations of this kind are performed in aqueous media, the Eu^{3+} luminescence is quenched as described in the previous sector. To circumvent this problem, the Eu^{3+} ion is bound to an ultraviolet-absorbing cryptand, which transfers its absorbed energy to the Eu^{3+} ion and shields the Eu^{3+} ion from the water molecules. By this shielding the radiationless processes in the weak-coupling scheme are depressed considerably. For this purpose a macrobicyclic cryptand bpy · bpy · bpy is used that contains three 2,2′-bipyridine groups (*104*). The properties of $[Eu \subset bpy \cdot bpy \cdot bpy]^{3+}$ and $[Tb \subset bpy \cdot bpy \cdot bpy]^{3+}$ cryptate have been described in the literature (*104, 107*).

Another clear example of a more complicated nature is the charge-

TABLE IV

THE STOKES SHIFT OF THE Ce^{3+} EMISSION FOR SEVERAL COMPOSITIONS

Composition	Stokes shift (cm^{-1})
$[Ce^{3+} \subset 2.2.1]$	2100
$[Ce^{3+} \subset 2.2.2]$	4000
Ce^{3+} in aqueous solution	5000
$Y_3Al_5O_{12}$–Ce^{3+}	3800
Y_2SiO_5–Ce^{3+}	2500
$ScBO_3$–Ce^{3+}	1200

transfer excitation of the Eu^{3+} luminescence, a process that is of great importance for applications. Consider the red phosphor in the three-color fluorescent lamps. Its composition is Y_2O_3:Eu. Excitation at 254 nm in the charge-transfer state is followed by efficient red emission ($^5D_0 - {}^7F_2$) within the $4f^6$ configuration. Figure 27 shows the relevant configurational coordinate diagram.

Note that the useful properties of Y_2O_3–Eu^{3+} are based on a fast radiationless process, viz., the transition from the charge-transfer state to the excited levels of the $4f^6$ configuration. For crystalline GdB_3O_6–Eu^{3+} the same model holds. This composition can also be obtained as a glass. Interestingly enough, charge-transfer excitation in the glass results in Eu^{3+} luminescence with a quantum efficiency that is an order of magnitude smaller than in the crystalline modification (*108*). This is also the case at 4.2 K. This observation has been ascribed to a larger offset of the charge-transfer parabola in the glass than in the crystal, so that in the glass the charge-transfer state empties mainly into the ^7F ground-state manifold. Similar observations have been made by Oversluizen (*109*). It is quite conceivable that the glass surroundings can counteract the expansion on excitation less than the crystalline surroundings. The important consequence of this is that broadband emission in glasses will have low efficiencies, unless the Stokes shift is small (see above).

The quantum efficiency of the emission of $[Eu \subset 2.2.1]^{3+}$ cryptate is very low on CT excitation (*110*). This can be explained as follows. The Eu^{3+} ion is smaller than the Ce^{3+} ion and does not fit the 2.2.1 cryptate cage. The cryptand then takes another configuration in which the cage is opened to one side: it becomes more or less a half sphere (*103*). In this configuration it cannot counteract the expansion of the Eu^{3+}-CT state

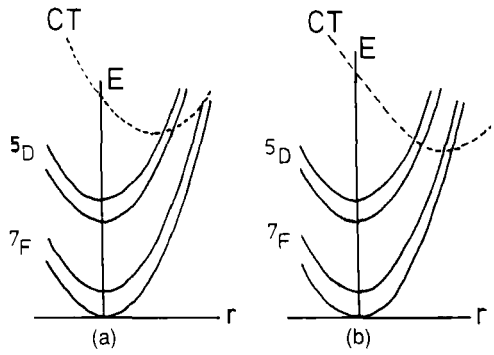

FIG. 27. The configuration coordinate diagram for Eu^{3+} in (a) Y_2O_3 and (b) glass.

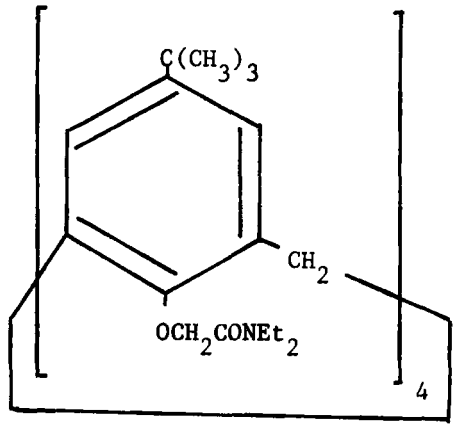

FIG. 28. The complex Eu^{3+}–calixarene.

and a large value of ΔQ results, which makes nonradiative transitions very probable. In Eu^{3+}-calixarene (*111*) (Fig. 28) the CT state is at about the same energy as in the 2.2.1 cryptate. Nevertheless it is possible to excite into this state with a reasonable quantum efficiency of the Eu^{3+} emission. The four "arms" of the calixarene ligand offer to the Eu^{3+} ion a close coordination in which strong expansion on excitation is not possible.

A related situation occurs with the transition from the $4f5d$ to the $4f^2$ configuration of Pr^{3+} (*112*). Also this phenomenon is of great technical importance. Figure 29 gives the configurational coordinate diagram of

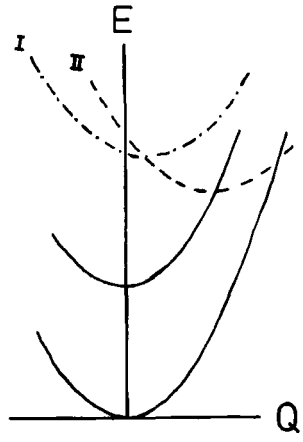

FIG. 29. The configurational coordinate diagram of Pr^{3+} ($4f^2$). Broken lines indicate two possible situations for the excited $4f5d$ configuration.

Pr^{3+} in two different host lattices. If the offset of the $4f5d$ state is small, radiative return to the $4f^2$ configuration has a higher probability than the nonradiative transition to the $4f^2$ configuration. If the offset is large, $4f5d$ excitation leads to emission from the $4f^2$ configuration after a nonradiative $4f5d \rightarrow 4f^2$ transition. The former situation is encountered for YBO_3 (*113*), YOCl (*114*), and LaB_3O_6 (*115*), the latter for the apatite $Gd_{9.33}(SiO_4)_6O_2$ (*116*) and Gd_2O_2S (*117*).

The Pr^{3+} case has an advantage above that of Eu^{3+}, viz., the higher excited state can emit, so that the Stokes shift can be measured. This gives information on the relaxation and the parabolas offset. It was found that the nonradiative $4f5d \rightarrow 4f^2$ transition becomes of importance if the Stokes shift is larger than 3000 cm^{-1}.

The Pr^{3+} ion can be used succesfully as a sensitizer in luminescent materials based on gadolinium compounds (*112–115*). However, this is only possible if the $4f5d$ state of Pr^{3+} decays radiatively. Otherwise the nonradiative return to the $4f^2$ configuration occurs more rapidly than the $Pr^{3+} \rightarrow Gd^{3+}$ transfer.

Our simple model predicts also that, if the parabolas offset is constant, the nonradiative transition will have a higher rate if the excited state is at lower energy. Or, in other words, broad excitation bands at low energies will usually imply low quantum efficiencies. Let us give a few clear examples. First we consider some organic Cu(I) complexes (see Table V) *118*). Absorption and emission occurs here in broad metal-to-ligand charge-transfer transitions. The rule stated above is well substantiated. This implies that it is easier to find efficient blue broadband emitters than red broadband emitters, a well-known experience of many phosphor investigators.

Similarly, if the charge-transfer state of Eu^{3+} shifts to low energies, the quantum efficiency of the red emission on broadband excitation drops considerably (*119*).

The more or less isoelectronic systems $CaWO_4$ and $CaMoO_4$ show broadband emission with maxima at 410 nm and 530 nm, respectively. Whereas $CaWO_4$ is very efficient at room temperature, $CaMoO_4$ is partly quenched (*96*).

Recently a new method for studying the relaxation around photoexcited centers in solids was reported by Straus and Walder (*120*). The authors observed the effect of the spatial relaxation of the matrix around the excited center in a condensed phase on the bulk optical index of refraction and used this information to derive the change in the equilibrium distance (i.e., ΔQ). For details the reader is referred to ref. *120*. The experiments were performed on Mn^{2+} in water (i.e., on the aqua-complex $[Mn(H_2O)_6]^{2+}$). No luminescence was observed. Since the

TABLE V

LUMINESCENCE PROPERTIES OF Cu^+ COMPLEXES[a]

Complex ion[b]	Absorption maximum (nm) in solution	Emission maximum (nm) 300K	Quantum efficiency 300 K	Decay time (μs) 4.2 K	300 K
$Cu(PPh_3)_2phen^+$	365	515	0.75	250	30
$Cu(PPh_3)_2dmp^+$	365	515	0.75	250	30
$Cu(PPh_2CH_3)_2dmp^+$	365	525	0.75	250	30
$Cu(PPh_3)_2bpy^+$	365	560	0.15	30	7
$Cu(PPh_3)_2biq^+$	415	605	0.17	30	7
$Cu(dmp)_2^+$	454	650	$\approx$0.01	3	–
$Cu(dpp)_2^+$	439	$\approx$710	<0.01	–	–
$Cu(biq)_2^+$	545	–	"0"	–	–

[a] After ref. *118*.

[b] PPh_3: triphenylphosphine; phen: 1, 10-phenanthroline; dmp: 2,9-dimethyl-1,10-phenanthroline; PPh_2CH_3: methyldiphenyl-phosphine; bpy: 2,2′-bipyridine; biq: 2,2′-biquinoline; dpp: 2,9-diphenyl-1,10-phenanthroline.

experimental lifetime was 4.6 μs and the radiative lifetime of the order of milliseconds, the return to the ground state was completely dominated by nonradiative processes.

The Mn^{2+} center was found to shrink on excitation, which is not unexpected, since the ground state is $^6A_{1g}$ ($t_{2g}^3e_g^2$) and the excited state $^4T_{1g}$ ($t_{2g}^4e_g$). On the other hand Cr^{3+} (in GdScGa–garnet) expands. The volume change in the case of $[Mn(H_2O)_6]^{2+}$ is $\Delta V = -7$ Å^3. This is solely due to the a_{1g} mode, because this is the mode that changes the volume of the complex. It is not a straightforward procedure to derive from this value of ΔV the corresponding value of ΔQ. The authors arrive at a value of -0.14 Å, which seems a very high value. The problem is which area belongs to the considered complex. If one take the average of the ionic radii of Mn^{2+} in the high-spin ($t_{2g}^3e_g^2$) and the low-spin state (t_2^5) we arrive at a $\Delta Q = -0.08$ Å. It is striking that these two completely different approaches yield values of the same sign and comparable values.

An appropriate way to close this section is to consider the radiationless transition that may occur by electron transfer, because it certainly belongs to the strong-coupling scheme. A rare-earth ion may lose its excitation energy not only by energy transfer, but also by electron transfer to other centers (*121*). The problem can be nicely illustrated by a molecular species, viz., the decatungstates $[RE \cdot W_{10}O_{36}]^{9-}$ (*122*).

In the case of $EuW_{10}O_{36}^{9-}$ the Eu^{3+} ion shows luminescence with high quantum efficiency. In view of the preceding arguments, $TbW_{10}O_{36}^{9-}$ and $GdW_{10}O_{36}^{9-}$ are expected to show even more efficient rare-earth ion emission. However, this is not the case. $GdW_{10}O_{36}^{9-}$ does not show any rare-earth emission at all, but only tungstate emission. The excited Gd^{3+} ion transfers its energy to the tungstate group, from which emission occurs. More problematic is the fact that $TbW_{10}O_{36}^{9-}$ shows neither efficient Tb^{3+} emission nor efficient tungstate emission. Obviously the complex as a whole undergoes a nonradiative decay to the ground state, which is not covered by the Förster–Dexter theory. This is quenching by *electron* transfer in solution, a well-known phenomenon that in nonmolecular solids is less general and has often been overlooked.

The quenching process occurs via an excited state that has a parabola in the configuration-coordinate diagram with a large offset relative to the ground-state parabola. In the case of the Eu^{3+} intraion decay this excited state was the (ligand-to-metal) CT state. However, a metal-to-metal CT state can also induce quenching if it is at low enough energy. Quenching is, therefore, expected to be of importance for a complex species consisting of a metal ion that is easily oxidized and another metal ion that is easily reduced. The complex $TbW_{10}O_{36}^{9-}$ is an exam-

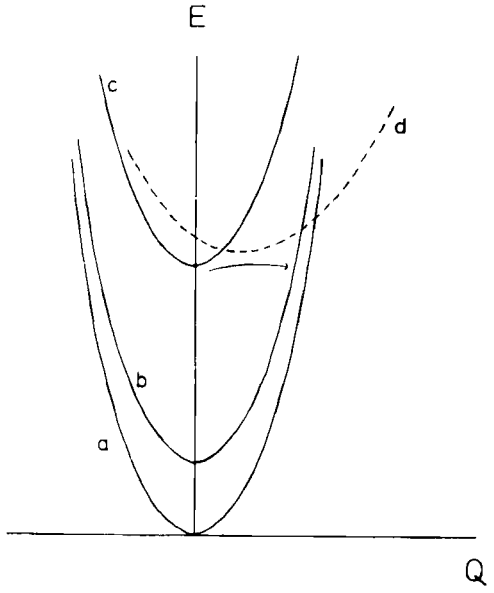

FIG. 30. Schematic representation of luminescence quenching by electron transfer.

ple, because the excited charge distribution Tb^{4+}-W^{5+} will not be at very high energy relative to the ground-state distribution Tb^{3+}–W^{6+}. This type of charge-transfer transition has an analogy to the so-called outer-sphere charge-transfer transition within ion pairs in solution (*123*). Figure 30 shows schematically this quenching process. It has been observed for many ion pairs in solution, for example, the quenching of the luminescence of $[Eu^{3+} \subset 2.2.1]$ by $M(CN)_6^{4-}$, where M = Fe, Os, or Ru (*124, 125*).

It has been little noted, however, that these processes occur also in nonmolecular solids. The quenching of all luminescence in YVO_4–Tb^{3+} is a striking example. The excited state, responsible for the quenching, has the approximate charge distribution V^{4+}–Tb^{4+}. It is interesting to note that $YTaO_4$–Tb^{3+} is a luminescent material with a very high quantum efficiency, whereas $YNbO_4$–Tb^{3+} is in between the vanadate and the tantalate. This comparison shows that the rate of the quenching process decreases if the metal-to-metal CT state shifts to higher energy (the fifth ionization potential of the host lattice metal increases in the sequence Ta, Nb, V).

V. Vibronic Transitions: New Results

Vibronic transitions have been discussed at length (*127, 128*), and much deeper than in Section II, A. These transitions have been observed for many types of optical centers. Here two special classes are discussed, viz., vibronic transitions in rare-earth ion spectra, and vibronic transitions involving Jahn–Teller vibrational modes (see Section VI).

The transitions within a given $4f^n$ configuration are usually assumed to be purely electronic, that is, to be zero-phonon lines. This is a very good approximation. However, careful monitoring of the spectra yields weak features that must be due to vibronic transitions. In some cases these are even relatively intense. Caro et al. have reviewed several examples, related mainly to Nd^{3+} and Pr^{3+} (*129*).

Recently the present author has reported extensive data on the vibronic transitions of Gd^{3+} (in cooperation with Dr. L. H. Brixner) and of Eu^{3+} (*130, 131*). These data will be reviewed here. Both ions show transitions that are very suitable to study the vibronic transition. For Gd^{3+} this is the $^6P_{7/2} \rightarrow {}^8S$ emission transition and for Eu^{3+} the $^7F_0 \rightarrow {}^5D_2$ absorption (excitation) transition. In the spectra these transitions occur as lines that limit a spectral region without any electronic transition. For example, in the emissin spectrum of Gd^{3+} the $^6P_{7/2} \rightarrow {}^8S$

emission line is the lowest-energy emission line. Every feature in the spectrum below this transition must be a vibronic line.

Let us give some examples. For Gd^{3+} vibronic transitions involving the $^6P_{7/2} \rightarrow {}^8S$ electronic transition and the following Gd-ligand vibrational transitions have been observed: Gd–O^{2-} (in Y_2O_3–Gd, ref. *34*); Gd-F^- (in Gd–fluorides, ref. *33*); Gd–Cl^- in ($Cs_2NaGdCl_6$, ref. *132*, Fig. 31); Gd–BO_3^{3-} (in YBO_3–Gd, refs *33, 130*); Gd–CO_3^{2-} (in $BaCO_3$:Gd, ref. *130*); Gd–H_2O and Gd–SO_4^{2-} [in $NaGd(SO_4)_2 \cdot H_20$, ref. *133* and $Gd_2(SO_4)_3 \cdot 8H_20$, ref. *134*, Fig. 32; Gd–OH^- (in $Y(OH)_3$:Gd, ref. *135*); Gd–ClO_4^- (in $Gd(ClO_4)_3 \cdot 6H_2O$, ref. *136*); Gd–SiO_4^{4-} (in $Na_2Si_2O_5$: Gd, ref. *130*); Gd–PO_4^{3-} (in $GdPO_4$, ref. *33, 130*, Fig. 33); Gd–GeO_4^{4-} (in Na_2GeO_3:Gd, ref. *130*), Gd–WO_4^{2-} (in $CaWO_4$:Gd, ref. *137*), Gd–TaO_6^{6-} (in Ba_2LaTaO_6:Gd, ref. *138*); Gd–cryptand (in $[Gd^{3+} \subset 2.2.1]Cl_3 \cdot 2H_2O$, ref. *139*; and Gd–acetate (in Gd–acetate tetrahydrate, ref. *140*).

This shows that the occurrence of vibronic transitions is a common phenomenon. The total vibronic intensity varies from less than 1% of the parent electronic transition to more than 10%. The examples mentioned show two different types of vibronic transitions, viz., those in which the relevant vibration occurs between Gd^{3+} and the ligand (e.g., Gd–F) and those in which the relevant vibration takes place on the ligand (e.g., Gd–H_2O). The latter type is called a cooperative vibronic

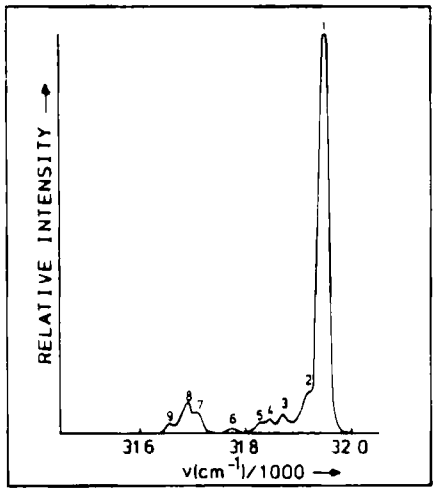

FIG. 31. Emission spectrum of $Cs_2NaGdCl_6$ at 4.2 K. (After A. J. deVries, Thesis, Utrecht.)

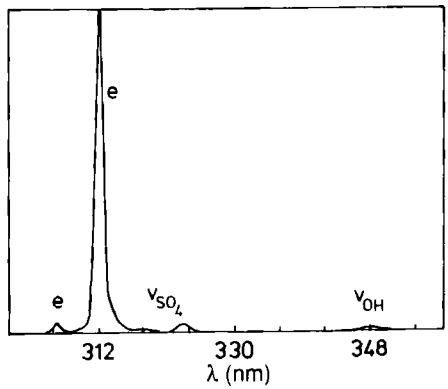

FIG. 32. The emission spectrum of $Gd_2(SO_4)_3 \cdot 8H_2O$. Vibronic transitions are indicated by v, electronic by e.

transition. It has been discussed by Stavola et al. (*141*), who observed it for the first time for an aqueous solution of Gd^{3+} (*142*). In $Gd(ClO_4)_3 \cdot 6H_2O$ there occur vibronics in which the vibration takes place on the second coordination sphere! (*136*).

In emission the rare-earth vibronic transitions are usually Stokes (i.e., at the lower energy side of the electronic line). The anti-Stokes lines have been observed for some suitable cases, for example LaF_3:Gd (*143*) (see Fig. 34).

The vibronic features in the spectra can also be used as probes of the surroundings of the rare-earth ion. For example, Brixner (*144*) was able to deduce that a Gd compound described in the literature as a Gd-

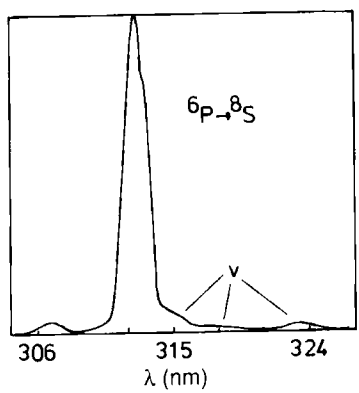

FIG. 33. The emission spectrum of $GdPO_4$ showing vibronic transitions (v).

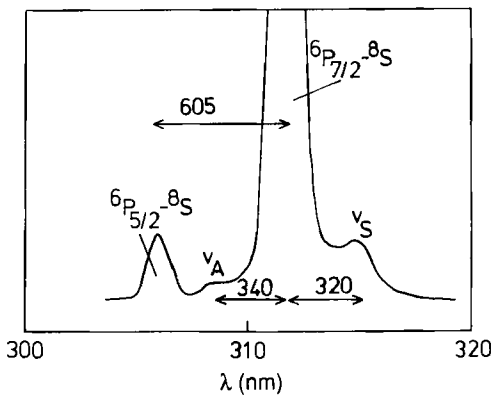

FIG. 34. Emission spectrum of LaF_3:Gd at 300 K under X-ray excitation. ν_A and ν_s are the anti-Stokes and Stokes vibronic lines.

oxalate is in reality a hydroxycarbonate, since CO_3^{2-} and OH^- vibronic transitions occur in the emission spectrum. Another example will be given in Section IX.

Let us now look somewhat more closely at the theory. The intensity of vibronic lines in the *f-f* spectra of rare earth ions is a complicated problem. Through the recent years the following approaches were made.

a. Faulkner and Richardson (*145*) gave a general theory of vibronically induced electric-dipole intensity in the *f-f* transition of octahedrally (O_h) coordinated trivalent rare-earth ions. The model includes static as well as dynamic coupling between the metal ions and the ligands. The calculations relate to elpasolite systems Cs_2NaMCl_6 [M = rare-earth ion(s)]. The coupling is with the ν_3, ν_4, and ν_6 vibrational modes of the MCl_6 octahedron. There is good agreement between the experimental results and the calculations.

b. Judd (*146*) has put forward a comparable approach for the same system (i.e., MCl_6 octahedron). In the static coupling he considers the interaction between the 4*f* electrons on M having a spherical charge distribution with net charge -ge (the ligand) and the dipoles that are induced in the ligands by the polarizing action of the central M^{3+} ion. The induced dipole moment is $3e\alpha\vec{r}_j/r_j^3$, where α is the ligand polarizability and r_j the distance from the M nucleus to the site j of the displaced ligand.

Further he shows that the dynamic-coupling term runs more or less parallel with the static coupling term. The dynamic term becomes more important if the covalency increases. Under certain conditions both terms are of comparable magnitude. We will present the final result below.

c. Stavola, Isganitis, and Sceats (*141*) added a new element to the discussion by considering cooperative vibronic transitions, that is, transitions in which there occurs simultaneously an electronic transition within the $4f$ shell of M and a vibrational transition within the ligand (for which OH^- and H_2O were used). The emission intensity depends a.o. on the infrared oscillator strength of the vibration and R^{-6}, where R is the M—ligand distance.

d. Dexpert–Ghys and Auzel (*147*) have compared the several approaches and shown that they overlap. The interaction Hamiltonian in approaches (a) and (b) is the odd vibrating part of the crystal field, and in (c) the Coulombic interaction between the M ion and the vibrating molecular species. It is shown that the static part of (a) and (b) is equivalent to (c). Further these authors state that all approaches neglect the classical one-phonon vibronic replicas (Franck–Condon case). We have shown experimentally that this point has been well taken (*148*).

At the moment we have available a large amount of data on vibronic intensities of Gd^{3+} in many different host lattices. The theoretical approaches are so complicated that they are not very suitable to analyze our data compilation. Therefore we have taken the general outcome as a basis for the further discussion. In the notation of refs (*146*) and (*147*) it runs as follows:

$$P_v \sim \nu(g + n\alpha R^{-3})^2 \, \Xi(1,2)^2 <J\|U^{(2)}\|J'>^2 \frac{1}{2J+1} <0\|T^{(1)}\|p>^2 \quad (13)$$

where P_v is the oscillator strength of the vibronic transition involved, ν its frequency, n the number of ligands around M, g and α the charge and polarizability of the ligand (see above), and R the M-ligand distance; $\Xi(1,2)$ is defined by Eq. 14 in ref. *149* and takes care of the opposite-parity mixing; J and J' are the total quantum numbers of the initial and final electronic states; the first matrix element is that of the reduced tensor operator $\| U^{(2)} \|$; and the second matrix element that of the electric dipole operator connecting the initial (0) and final (p) vibrational states.

Considering only vibronics belonging to the $^6P_{7/2} \rightarrow {}^8S$ transition, the J values and the $U^{(2)}$ matrix element will not vary. Note, however, that this matrix element imposes a selection rule on the vibronic transi-

tions, viz., $\Delta J = 0, \pm 2$. The $T^{(1)}$ matrix element predicts the most intense vibronic lines for coupling with the most infrared-intense vibrational transitions.

The term $(g + n\alpha R^{-3})^2$ is hard to analyze. It will vary less with the nature of the ligands than first thought. A higher value of g implies a lower value of α; an increase of α will usually mean that R increases too. If we consider one and the same ligand, for example oxygen, the value of α might well be different. This will be discussed now.

To start with we have presented in Table VI a number of Gd^{3+}-containing compositions for which the value of r is known (r gives the ratio between the total vibronic intensity and the electronic intensity). This value varies an order of magnitude. Although this ratio is often used in the literature, it should be realized that its value is not absolute, since the radiative rate of the electronic $^6P_{7/2} \rightarrow {}^8S$ transition varies from compound to compound. For a site with inversion symmetry this transition is purely magnetic-dipole, but if the center of symmetry is absent it also has electronic-dipole character. The radiative vibronic rate can be found by measuring the radiative decay rate of the $^6P_{7/2}$ level, the ratio r, and using the calculated radiative rate for magnetic-dipole emission. This has not been performed for many compositions. Recently these data have been reported for YOCl:Gd (*150*).

In $Y(OH)_3$:Gd (*135*) two clearly different types of vibronic transitions are observed. The one due to coupling with the OH^- vibration is of the

TABLE VI

RATIO r FOR THE $^6P_{7/2} \rightarrow {}^8S$ TRANSITION IN SEVERAL HOST LATTICES[a]

Composition	r[b]	Composition	r[b]
$Cs_2NaGdCl_6$	0.3	Gd-acetate·$4H_2O$	0.08
Gd_2O_2S	0.3	$Y(OH)_3$:Gd[c]	0.08
La_2O_3:Gd	0.25	$GdAl_3B_4O_{12}$	0.08
LaOCl:Gd	0.16	CaS:Gd	0.07
Ba_2LnTaO_6:Gd	0.12 (average)	$ScBO_3$:Gd	0.05
Y_2O_3:Gd	0.12	$CaCO_3$:Gd	0.03
$GdCl_3·6H_2O$	0.1	$LaAlO_3$:Gd	0.02
$CaWO_4$:Gd	0.09	[Gd ⊂ 2.2.1]$Cl_3·2H_2O$	0.02
$YTaO_4$:Gd	0.09	LaF_3:Gd	0.02
BaFBr:Gd	0.08	$Gd(ClO_4)_3·6H_2O$	0.02

[a] At room temperature; from ref. *138*.

[b] r, The ratio of the total vibronic intensity and the electronic intensity of the transition.

[c] OH^- contributes only 0.002.

cooperative type. Stavola et al. (*141*) performed a quantitative calculation of the OH^- vibronic transition belonging to the $^6P_{7/2} \rightarrow {}^8S$ transition, but compared the results to experiments where H_2O is used as a ligand. The infrared oscillator strength of the OH^- ion amounts to $(1–6) \times 10^{-3}$. With this value they arrived at a radiative rate for coupling with one OH^- group of 0.08 s^{-1}. This yields for nine OH^- groups (as in $Y(OH)_3$:Gd) 0.7 s^{-1}.

For this vibronic transition we find from the spectra $r = 0.002$. With a total radiative rate of 300 s^{-1} the OH^- vibronic rate is about 0.6 s^{-1}. This is a very good agreement with the prediction by Stavola et al.

For the stretching of H_2O the oscillator strength in the infrared is an order of magnitude larger than for OH^-, especially if hydrogen bonding occurs. In fact the r value of H_2O vibronic lines due to coupling of the stretching mode with the $^6P_{7/2} \rightarrow {}^8S$ transition is also an order of magnitude larger than for the OH^- stretching vibration. Examples are $[Gd \subset 2.2.1]Cl_3 \cdot 2H_2O$ (see Table VI), $Gd_2(SO_4)_3 \cdot 8H_2O$ (*134*), $NaGd(SO_4)_2 \cdot H_2O$ (133), and $Gd(ClO_4)_3 \cdot 6H_2O$ (Table VI).

The coupling with the Gd vs. $(OH)^-$ vibration in $Y(OH)_3$:Gd is much stronger, yielding $r = 0.08$. This is ascribed to a large value of the product $n\alpha$ in Eq. (13). For $Y(OH)_3$, $n = 9$. The value of α is hard to derive. According to data in ref. *151* it is not much different from that of water, which implies that $\alpha(OH)^-$ is closer to $\alpha(F^-)$ than to $\alpha(O^{2-})$. However, we have to take into account the frequency dependence of α. This can be done by using the formula (*69*)

$$\alpha(\nu) = \frac{e^2}{m} \sum_j \frac{f_{ij}}{\nu_{ij}^2 - \nu^2} \tag{14}$$

Here ν is the frequency under consideration, ν_{ij} the absorption frequency and f_{ij} the oscillator strength of the electronic transition between the states i and j. From the diffuse reflection spectrum discussed above it is clear that $\alpha(OH^-)$ at the frequency of the vibronic transition involved will be large, since $\nu_{ij}^2 - \nu^2$ is relatively small.

Since $\alpha_o\,(OH^-)$ is slightly larger than $\alpha_o\,(F^-)$, viz., $1.75 \cdot 10^{-24}$ vs. $1.04 \cdot 10^{-24}$ cm^3, respectively, and α_ν will be considerably larger for OH^- than for F^- because the optical absorption transition is at lower energy for the hydroxide than for the fluoride, it becomes clear that the vibronic transitions in Gd^{3+}-doped fluorides will be considerably less intense (see LaF_3:Gd in Table VI).

Let us consider Ba_2LaTaO_6:Gd. In this host lattice the Gd^{3+} ion has site symmetry O_h and is coordinated by six tantalate octahedra that also have O_h site symmetry. The emission spectrum of the Gd^{3+} ion

shows three vibronics due to coupling with the ν_3, ν_4, and ν_1 modes of the tantalate group. The ν_3 and ν_4 modes appear as strong bands in the infrared spectrum, so that their occurrence in the vibronic spectrum is not unexpected. However, the symmetric stretching mode ν_1 does not appear in the infrared spectrum. The matrix element $<o \| T^{(1)} \| p>$ is zero for this vibration, so that Eq. (13) also gives zero for the vibronic transition involving ν_1. Nevertheless it is observed with an r ratio of about 0.01.

This vibronic transition is ascribed to a Franck–Condon vibronic replica. The coupling parameter S can be estimated from the r value using the expression $e^{-s} = I(o\text{-}o)$, where $I(o\text{-}o)$ gives the relative intensity of the zero-phonon (or pure electronic) transition (*1*). From $e^{-s} = 0.99$ we find $S = 0.01$. Such a low value is not unexpected for the rare-earth ions and was also used in ref. *147*. A vibronic line due to coupling with a totally symmetric vibrational mode with comparable relative intensity has been observed before in many other compositions: for example, $Cs_2NaGdCl_6$ (*132*), $YTaO_4$:Gd (*130*), $GdAl_3B_4O_{12}$ (*130*), $BaSO_4$:Gd (*130*), and $BaCO_3$:Gd (*137*).

The vibronic transitions involving ν_3 and ν_4 are more intense. These modes are infrared active. In the infrared spectrum these modes have about equal intensity, as in the vibronic spectrum. The relatively high intensity of the ν_3 and ν_4 vibronic transitions is ascribed to a relatively high value of α. It should be realized that the tantalate group in Ba_2GdTaO_6 shows a broad absorption band with a maximum at 41,700 cm^{-1}. For Ba_2LaTaO_6 this result will not be much different. Equation (4) then predicts an increase of α, especially so since the value of f_{ij} is also high for the tantalate absorption transition.

The r values for Gd^{3+} in the ordered perovskites Ba_2LnTaO_6 (Ln = La, Y, Lu) depend on Ln (*138*). This is not the case for the phonon replica due to coupling with ν_1. The intensity of the vibronic transitions due to coupling with ν_3 and ν_4 should obey Eq. (13). However, this equation does not contain a term that is expected to vary from La to Lu. Since the space available for the Gd^{3+} ion decreases from La to Lu, the covalency will increase. According to Judd (*146*) and Faulkner and Richardson (*145*) increasing covalency results in higher vibronic intensity. We assume that the series Ba_2LnTaO_6:Gd, where the properties involved do not vary with the choice of Ln, is a fine example of the prediction that the vibronic intensity increases with increasing covalency.

In the elpasolite (i.e., ordered perovskite) $Cs_2NaGdCl_6$, r amounts to 0.3. There are no molecular vibrational modes. Coupling occurs with the modes of the regular $GdCl_6^{3-}$ octahedron (*132*). The values of α for Cl^- and O^{2-} are practically equal (*69*). It is questionable, however,

whether these ionic α values are useful in this connection. The Cl^- ion in elpasolite is strongly polarized toward the Gd^{3+} ion, the ion on the other side of the anion being Na^+. This is a favorable situation for high vibronic intensity, as we will see. Also, this configuration will result in a higher degree of covalency, which also promotes higher intensity (see above). Finally, R will be shorter than for the tantalate perovskite.

Now we consider the other compositions in Table VI that lack molecular (internal) vibrations. They are all characterized by a high value of r, except LaF_3:Gd. Fluorides are expected to give low vibronic intensities in view of the low value of α and the low degree of covalency. The compositions La_2O_3:Gd and Y_2O_3:Gd show high values of r, where the former gives more intense vibronics than the latter. These compounds are rather covalent, and α will be increased by the presence of a low-lying host lattice absorption (La_2O_3 44,000 cm^{-1}, Y_2O_3 47,500 cm^{-1}).

The r value for CaS:Gd (0.07) is not as high as first expected in view of the high value of α (S^{2-}) (viz., 10.2×10^{-24} cm^3) (*69*) and the low optical absorption edge (33,600 cm^{-1}). However, the high value of α is counteracted by the increase of R. More important seems the symmetric coordination of the S^{2-} ions in the rocksalt structure of CaS. This reduces the possibility to polarize the S^{2-} ion toward the Gd^{3+} ion, which will occur only in the presence of an effective positive charge on the Gd^{3+} ion.

In most of the oxidic coordinations with absorption transitions in the vacuum UV, the value of r does not exceed a few percent. $ScBO_3$:Gd, and especially $GdAl_3B_4O_{12}$, seems to have rather high r values (see Table VI). Perhaps the small distance R, due to the six-coordination of Gd^{3+} and the bent Gd–O–B angle, plays a role here. The former favors covalency, the latter a shorter distance.

The high r value for the Gd-acetate is related to the low absorption transition of the acetate group, which roughly coincides with the $^8S \rightarrow {}^6P$ transition on the Gd^{3+} ion (*140*).

Similar considerations hold for Eu^{3+}. The case of $SrTiO_3$:Eu^{3+} (*131, 152*) is here very exceptional (see Fig. 35). Not only the vibronics belonging to the $^5D_0$ - $^7F_2$ emission ($\Delta J = 2$) are very intense, but also those belonging to the $^5D_0$ - $^7F_1$ emission ($\Delta J = 1$). The former has been ascribed to the high polarizability of the ligands (*131*) in agreement with Eq. 13). The latter, however, are forbidden by Eq. (13) due to the selection rule on ΔJ. They have to be considered as the classical one-phonon vibronic replicas (*131*). Using the expression e^{-s} for the relative amount of electronic intensity, S being the Huang–Rhys parameter, we can derive for S the value of 1.4. This is much larger than usually assumed (S = 0.01, refs. *130, 147*).

The presence of relatively strong vibronic side lines to the magnetic-

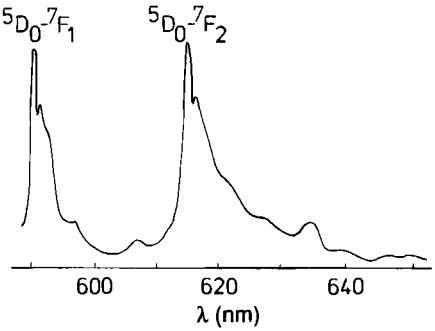

FIG. 35. The emission spectrum of $SrTiO_3:Eu^{3+}$ at 4.2 K.

dipole $^5D_0$ - $^7F_1$ transition and the corresponding relatively high values of the Huang–Rhys parameter S point to a different amount of admixture of excited configurations to the original and final levels of the transition. Calculations using configuration interaction are necessary to confirm this statement. In this connection a recent report by Garcia and Faucher is of interest (*153*). They made such a calculation for Pr^{3+}, limiting theirselves to the two lowest configurations, $4f^2$ and $4f5d$. It is interesting to note that the multiplet barycenters are affected differently: their values decrease only 4 cm^{-1} for $^3H_5$ but 60 cm^{-1} for $^3P_2$. The latter level is much closer to the $4f5d$ configuration. Also, the configuration interaction tightens all the multiplets, but not so the $^1D_2$. The crystal-field splitting of the $^1D_2$ level can be well accounted for if configuration interaction is taken into account.

Finally we note that recently beautiful extended vibronic spectra have been reported by Berry et al. (*154*) for hexakis (antipyrine) europium (III) tri-iodide and tri-perchlorate. More than 50 lines belonging to the $^7F_0$ - $^5D_2$ transition were reported.

VI. The Jahn–Teller Effect from Emission Spectra

During the last decade it has been observed that the excited state of optical centers is often strongly distorted due to the Jahn–Teller effect. This puts the simple configurational coordinate model with the breathing mode as a coordinate in severe doubt. Also, it now becomes clear that the Stokes shift is in many cases due to a relaxation via a Jahn–Teller active mode. Let us illustrate these statements by several examples that originate from three types of centers, viz., transition

metal ions (d^n), closed-shell transition-metal ions (d^{0n}), and ions with ns^2 configuration.

In II,A we mentioned the Jahn–Teller effect in the excited $^4T_2$ state of Mn^{4+}. The isoelectronic Cr^{3+} ion shows emission from this state if the crystal field is sufficiently weak. Broadband Cr^{3+} emission has been observed in halides (e.g., in the fluorides $KZnF_3$ (*155*) and $SrAlF_5$ (*156*) and in several oxides (e.g., $ScBO_3$ (*157*), $Sr_3Sc_2(BO_3)_3$ (*158*), and several garnet compositions (*159*). These show a broad emission band with a maximum in the range 750–950 nm. The decay time, at low temperatures ~100 μs, drops rapidly above room temperature due to nonradiative losses (see above). A much more detailed study is that by Güdel et al. (*160*) on several elpasolites with Cr^{3+} ($Cs_2NaInCl_6$, Cs_2NaYCl_6, Cs_2NaYBr_6). The former two show broadband emission with vibrational structure. There are progressions in $\nu_1(a_{1g})$ and in $\nu_2(e_g)$ (see Fig. 36). This enables us to obtain an accurate picture of the relaxed excited $^4T_{2g}$ level. Table VII gives S values derived from the progressions in a_{1g} and e_g and from the Stokes shift. We are clearly dealing with an intermediate coupling case. Table VII also gives the distortions. We observe again that the distortions are larger if the host-lattice ion involved is larger ($r_{Y^{3+}} > r_{In^{3+}}$) or the anion is larger ($r_{Br^-} > r_{Cl^-}$). The e_g progression is a clear indication of a Jahn–Teller effect in the $^4T_{2g}$ level.

In connection with our treatment of the configurational coordinate diagram (see above) it should be noticed that the occurrence of two

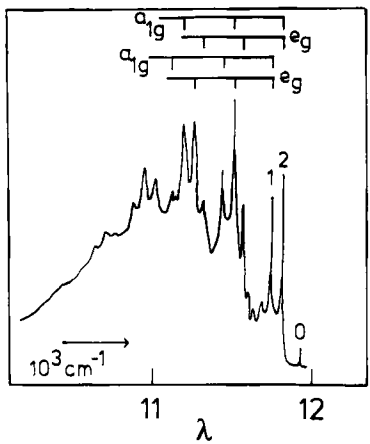

FIG. 36. Emission spectrum of $Cs_2NaInCl_6:Cr^{3+}$ at 10 K. Vibrational progressions in a_{1g} and e_g are shown. (After data in ref. *160*.)

TABLE VII

PARAMETERS CHARACTERIZING THE $^4T_2 \rightarrow {}^4A_2$ EMISSION OF Cr^{3+} IN SOME CUBIC ELPASOLITES[a]

Host lattice	$Cs_2NaInCl_6$	Cs_2NaYCl_6	Cs_2NaYBr_6
$S(a_{1g})$[b]	1.6	1.6	[c]
$S(e_g)$[b]	1.1	1.7	[c]
S_{total}[d]	3.7	3.6	6.7
Stokes shift (cm^{-1})	1780	1740	2200
$\Delta Q(a_{1g})$ (Å)	0.13	0.13	0.22[e]
$\Delta Q(e_g)$ (Å)	−0.13	−0.15	−0.22[e]
$\Delta_{x,y}$ (Å)	0.09	0.10	0.15
Δz (Å)	−0.02	−0.03	−0.05

[a] Data from ref. *160*.
[b] From intensity ratios in vibrational progression.
[c] No vibrational structure observed.
[d] From the value of the Stokes shift.
[e] Assuming $\Delta Q(a_{1g}) = \Delta Q(e_g)$.

progressions for Cr^{3+} in the elpasolites indicates that a multiconfigurational coordinate diagram must be used.

Considerable progress has been made in understanding the excited state of transition-metal ion complexes with an empty *d* shell. Examples are CrO_4^{2-}, VO_4^{3-}, and MoO_4^{2-}. Van der Waals group has contributed considerably (*161–164*). The emission of these species is usually structureless with a large Stokes shift (strong-coupling case).

It has long been realized that the transitions involved are of the charge-transfer type, and that the emitting state is a triplet state (*96*). This follows from the long decay times observed. Further characterization is hardly possible, due to the absence of any structure in the spectra. By performing EPR measurements in the excited state Van der Waals et al. were able to demonstrate directly the triplet character of this excited state.

Let us first consider $CaMoO_4$ (*163*). In the ground state there is one MoO_4^{2-} group with S_4 site symmetry in the unit cell. However, in the excited state there are four magnetically equivalent MoO_4^{2-} groups in the unit cell. These show a strong trigonal distortion due to a static Jahn–Teller effect. This distortion can occur along any of the four Mo–O bonds. This means that the configurational coordinate diagram should take a Jahn–Teller active mode into account (probably the ν_2 mode). It is interesting to note that the interactions entering the prob-

lem decrease in the order: Jahn–Teller coupling > crystal field > spin-orbit coupling.

Very similar results have been observed for YVO_4 (with a VO_4^{3-} group). In $Ba_3(VO_4)_2$ the site symmetry is C_{3v}. Therefore only one or three inequivalent excited species are expected. The latter possibility turned out to be the case. This confirms the model sketched.

Another example of a different kind is the class of ions with s^2 configuration, for example Tl^+, Pb^{2+}, Bi^{3+} (all $6s^2$), and Sn^{2+}, Sb^{3+} (both $5s^2$). The theory of their absorption and emission spectra in alkali halides has been reviewed by Ranfagni et al. (*165*). The host lattice dependence of the luminescence of these ions has been studied in oxides and halides. This dependence is strong for Bi^{3+} (*166, 167*). In $Cs_2NaYCl_6:Bi^{3+}$ the emission is a narrow band with considerable vibrational structure and a small Stokes shift. In $LaPO_4:Bi^{3+}$ the emission is a broad band without any structure at all and with a large Stokes shift. Table VIII shows that the Stokes shift may vary one order of magnitude, and the same will hold true for the value of the Huang–Rhys factor S (*166*).

This large variation has been ascribed to the amount of space available for the Bi^{3+} ion in the lattice. The small-Stokes-shift case (vibrational structure) is only observed for Bi^{3+} in 6 coordination. Examples are Cs_2NaYCl_6 (*168*), CaO (*169*), $NaMO_2$ (M = Sc, Lu, Y, Gd) (*170*), and $YAl_3B_4O_{12}$ (*171*). The Bi^{3+} ion is too large for six coordination and has no possibility to relax to a different equilibrium distance of the excited state. In a large hole (eight or higher coordination) the situation is different. It has been proposed that in the ground state the Bi^{3+} ion goes off-center in such a situation, so that it obtains its preferred asymmetrical coordination (*171*). This is a pseudo Jahn–Teller effect. On excitation it relaxes to the center of the coordination polyhedron. Because of this large relaxation a large Stokes shift results.

There is twofold evidence for such a model. In the first place an EXAFS study by Van Zon et al. on $LaPO_4$–Bi has shown that the Bi^{3+} coordination is different from the La^{3+} coordination (*172*). In the second place Bi^{3+} compounds with asymmetrically coordinated Bi^{3+} ions (as determined crystallographically) show luminescence with very large Stokes shifts. Examples are $Bi_4Ge_3O_{12}$, $Bi_2Ge_3O_9$, and $Bi_2Al_4O_9$. The ground state is distorted due to the pseudo Jahn–Teller effect (*173*). The same holds for the isoelectronic Pb^{2+} ion ($PbAl_2O_4$, $PbGa_2O_4$).

The excited configuration of the Bi^{3+} ion is $6s6p$, which yields a lower ^3P state. This state is subject to spin-orbit (SO) coupling and the Jahn–Teller (JT) effect. In the case of $6s^2$ ions, SO coupling dominates and the spectra can be interpreted along those lines. In the case of $5s^2$ ions the

TABLE VIII

STOKES SHIFT OF THE EMISSION OF THE Bi^{3+} ION ($6s^2$) IN SEVERAL HOST LATTICES, TOGETHER WITH THE VALUE OF THE ENERGY DIFFERENCE (ΔE) BETWEEN THE $^3P_1$ AND $^3P_0$ LEVELS[a]

Composition	Stokes shift (cm^{-1})	ΔE(cm^{-1})
Cs_2NaYCl_6–Bi	800	1.150
$Cs_2NaLaCl_6$–Bi	~1.200	800
Cs_2NaYBr_6–Bi	1.600	650
$ScBO_3$–Bi	1.800	1.000
$YAl_3B_4O_{12}$–Bi	2.700	1.100
CaO–Bi	2.700	1.200
$CaLaAlO_4$–Bi	7.700	400
$LaBO_3$–Bi	8.500	440
LaOCl–Bi	8.500	540
$CaSb_2O_6$–Bi	8.800	410
BiOCl	9.600	~400
La_2O_3–Bi	10.800	370
La_2SO_6–Bi	11.200	380
$Bi_2Al_4O_9$	16.000	25
$Bi_4Ge_3O_{12}$	17.600	25
$Bi_2Ge_3O_9$	20.000	16
$LaPO_4$–Bi	19.200	16
CaO–Pb	2.000	950
$PbAl_2O_4$	19.2000	60

[a] After ref. *166* with addition of several data from the Debye laboratory.

JT becomes important. Because of mixing of ground and excited state, the ground state distorts. However, the structureless broad bands in the spectra prevent the evaluation of parameters.

The case of Sb^{3+} ($5s^2$) has also been investigated. The SO coupling is less important here. Oomen et al. have studied the Sb^{3+} luminescence in the elpasolites Cs_2NaMCl_6 and Cs_2NaMBr_6, where M is an optically indifferent lanthanide ion (*174, 175*). The site available for the dopant Sb^{3+} ion has perfect octahedral symmetry. The Jahn–Teller effect can now be observed in the absorption spectra, because a temperature-dependent splitting of the $^1S_0 \rightarrow {}^3P_1$ transition occurs. It was also observed that the Stokes shift increases for larger M ions. The elpasolites form a good model system because of the octahedral coordination for the M ion. In oxides, however, the Sb^{3+} coordination is more irregular.

Nevertheless the orthoborates show the same increase of the Stokes shift of the Sb^3+ emission for increasing host lattice cation (*176*). This suggests that the model proposed for Bi^{3+} is also valid for Sb^{3+}.

Extremely remarkable is the case of $YPO_4:Sb^{3+}$ (*177*). In this lattice the Sb^{3+} ion shows two emissions from the ^3P relaxed excited state. This is due to the JT effect, which results in two different minima from which emission occurs (Fig. 37). At low temperature the X minimum, which is populated by optical excitation, emits. At higher temperatures the barrier can be overcome, and emission from the T minimum is also observed. At still higher temperatures thermal equilibrium occurs and the X emission reappears (see Fig. 38). In $LuPO_4$ and $ScPO_4$ the barriers are slightly different, but the situation is in principle the same. These effects were previously observed only in the alkali halides (*165*).

The occurrence of two different minima depends markedly on the ratio between SO and JT couplings and the site symmetry of the s^2 ion.

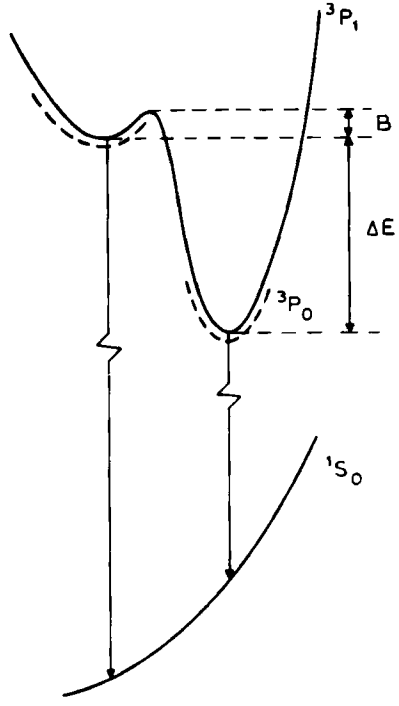

FIG. 37. Schematic configurational coordinate diagram for $LnPO_4$–Sb^{3+} (Ln = Y, Sc, La). See text.

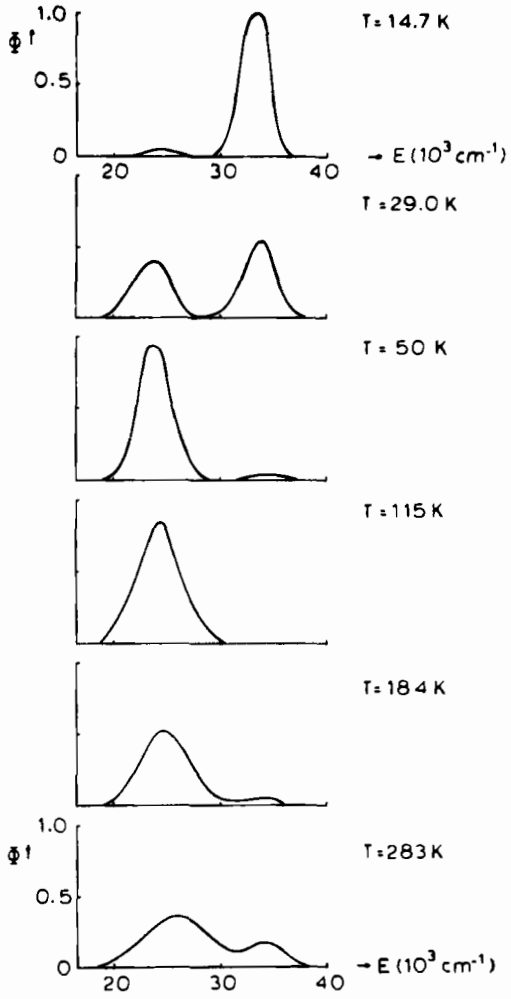

FIG. 38. Emission spectra of YPO_4–Sb^{3+} as a function of temperature. See text. (After E. W. J. L. Oomen, Thesis, Utrecht, 1987.)

The observation of the double Sb^{3+} emission in YPO_4 is, therefore, unique. For Bi^{3+} it has never been observed due to strong SO coupling.

In this connection recent results on the Te^{4+} luminescence in Cs_2TeCl_6 and $Cs_2Zr_{1-x}Te_xCl_6$ are of interest (*178–181*). The absorption spectra of the Te^{4+} ion, which occupies a regular octahedral site in this structure, are comparable to those for Sb^{3+} in the elpasolites.

They show also the influence of the Jahn–Teller effect. The emission spectrum shows a vibrational structure that consists of a long progression in ν_2 (e_g), a JT-active mode. This points to a strongly distorted excited state (X). According to Schmidtke et al. (*178*) the magnitude of the distortion is $\Delta z = -2\Delta x = -2\Delta y = 0.2$ Å, corresponding to a tetragonal Jahn–Teller distortion.

Donker (*182*) has recently given an interesting relation for the Sn^{2+} ($5s^2$) luminescence. The larger the Stokes shift of the luminescence, the higher the position of the absorption band (see Fig. 39). This is a remarkable relation, the origin of which is not so easy to explain by a simple, single consideration (*182*).

In conclusion we note that up till a few years ago it was generally

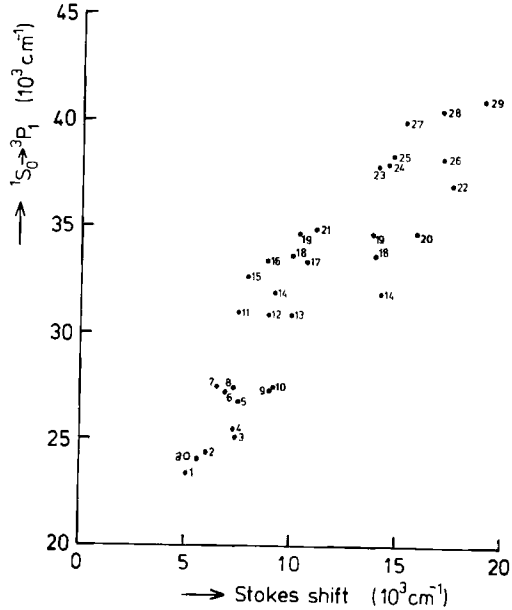

FIG. 39. Stokes shifts vs. spectral position of the $^1S_0 \rightarrow {}^3P_1$ transitions for various compositions containing $5s^2$ ions at octahedral sites (after ref. *182*). 1, CaSe:Sb^{3+}; 2, MgS:Sb^{3+}; 3, Cs_2ZrCl_6:Te^{4+}; 4, CaS:Sb^{3+}; 5, CaSe:Sn^{2+}; 6, CaO:Sn^{2+}; 7, $Cs_2NaScBr_6$:Sb^{3+}; 8, Cs_2NaYBr_6:Sb^{3+}; 9, $Cs_2NaLaBr_6$:Sb^{3+}; 10, CaS:Sn^{2+}; 11, $Cs_2NaScCl_6$:Sb^{3+}; 12, Cs_2NaYCl_6:Sb^{3+}; 13, $Cs_2NaLaCl_6$:Sb^{3+}; 14, KI:In^+; 15, $ScBO_3$:Sb^{3+}; 16, NaCl:In^+; 17, $LuBO_3$:Sb^{3+} (hT); 18, KBr:In^+; 19, $KCaCl_3$:Sn^{2+}; 20, $CsCaCl_3$:Sn^{2+}; 21, KCl:In^+; 22, $CaCO_3$:Sn^{2+}; 23, YBO_3:Sb^{3+}; 24, $GdBO_3$:Sb^{3+}; 25, $LuBO_3$:Sb^{3+} (1T); 26, ZrP_2O_7:Te^{4+}; 27, $Sc(PO_3)_3$:Sb^{3+}; 28, $Lu(PO_3)_3$:Sb^{3+}; 29, $Gd(PO_3)_3$:Sb^{3+}; 30, SnO(molecule).

agreed that the Stokes shift is mainly due to a parabola offset in the configurational coordinate diagram, using the breathing mode as a coordinate (see Section II,A). Now it is becoming more clear that Jahn–Teller modes also play an important role. Large Stokes shifts, like those observed for YVO_4, $CaMoO_4$, and Cs_2TeCl_6, are probably mainly due to an offset along a Jahn–Teller coordinate. Research along these lines is on its way.

VII. Localization vs. Delocalization

In the preceding chapters the discussion was based on the configurational coordinate diagram. The luminescence centers were classified according to the value of the Huang–Rhys parameter S, which determined their properties in a decisive way. This implies that the interaction between electronic and vibrational transitions was dominant in the discussion. However, there is another important factor in solids that results in delocalization of the electronic charge. Whereas the discussion up till here results in localization, we will now show that there is a competitive effect resulting in delocalization. The treatment is based on considerations given for the first time by Toyozawa (*183*) and elucidated by us elsewhere (*166, 184*).

Imagine a system of luminescent centers, each with a two-level energy scheme. After excitation we can distinguish two extreme situations. In general the radiative lifetime τ_r is much longer than the electron-lattice relaxation time τ_{lr}, so that after excitation the excited state relaxes to the equilibrium state of the excited state. The relaxation lowers the energy of the systems by E_{1r}. If E_{1r} is large enough, the excitation energy stays at that particular site accompanied by a distortion of the surroundings (self-trapped state, S). However, there exists another energy effect: the excitation energy can be transferred from one center to another, forming an exciton band of width $2B$, where $2B = 2\nu|J|$. Here ν is the number of nearest neighbors and J the transfer energy between nearest neighbors. The total energy of the system is lowered by B if the excitation propagates through the crystal without lattice distortion (nearly free state, F).

Excitonic emission from the F state should be a sharp line (almost resonant with the onset of the band gap), whereas emission from the S state should be a Stokes-shifted broad band, characteristic of localized deexcitation. Closer consideration suggests that the stable state changes abruptly from F-like to S-like when the ratio $g = E_{1r}/B$ exceeds a certain value ($g \simeq 1$). The emission of TiO_2 and $CsVO_3$ is an

example of the F state, the emission of YVO_4 and $CaWO_4$ of the *S* state (*166*). For a very pure TiO_2 crystal we have observed a free excitation line at 412 nm, but also a broad band with a maximum at 485 nm (*185*). This emission might be ascribed to self-trapped excitations.

Examples of pronounced S state emission (i.e., high Huang–Rhys parameter values) have been treated in the preceding paragraphs. Here we remind the reader of $CaWO_4$ and $Bi_4Ge_3O_{12}$ as representative examples with Stokes shifts of 2 eV (16,000 cm^{-1}) or larger. Excitation into these centers is followed by a drastic relaxation in the excited state that brings the excited state out of resonance with the ground state, so that localisation results.

The compounds $SrTiO_3$ and $KTiOPO_4$ show S-state emission with a low thermal activation energy. In $KTiOPO_4$ the titanate groups form linear chains by corner sharing, so that the delocalization is one-dimensional (*186*). Compounds in which this delocalization plays a role often do not luminesce at all, since the excitation energy can easily reach quenching centers.

In this connection it is interesting that $KTiOPO_4$ doped with several impurities with high energy levels shows an emission that is very different from the pure material and independent of the dopant (*186*). Whereas the emission band of $KTiOPO_4$ has its maximum at about 390 nm, the doped samples have it at about 530 nm. The dopants are Zr^{4+} and the combination Nb^{5+}–Ga^{3+}. The explanation for this is that the dopant ions break the linear titanate chains. In this way the energy migration over the chain is hampered and the excitation energy is trapped by the titanate groups that form the end of the chain. Emission occurs from these ions.

The ions with s^2 configuration can show a very similar behavior. Whereas in some cases clear S-state emission has been observed ($Bi_4Ge_3O_{12}$, see above), the F-state emission and semiconducting properties have been observed for $Cs_3Bi_2Br_9$ (*187*). Note that bismuth compounds show a large flexibility in our description: whereas $Cs_2NaBiCl_6$ shows only a very weak relaxation and no delocalization (see above), $Cs_3Bi_2Br_9$ shows a typical F-state emission and $Bi_4Ge_3O_{12}$ a typical S-state emission. Figure 40 shows this in a schematic way. The top of the triangle gives the free Bi^{3+} ion. Along the right-hand leg localization in the solid increases; that is, the electron-lattice interaction and the relaxation in the excited state increases. Along the left-hand leg, delocalization by wave-function overlap increases. Compounds of the rare-earth ions are to be expected in the top of such a triangle, compounds like titanates and tungstates along the base. Those of $6s^2$ ions (Pb^{2+}, Bi^{3+}), however, can be found all over the triangle. The compound

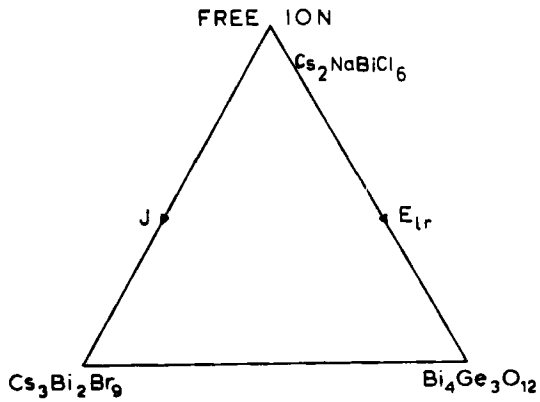

FIG. 40. Schematic representation of luminescent centers. E_{lr}, electron-lattice relaxation; J, band broadening. See also text.

$Cs_2NaBiCl_6$, for example, should be placed somewhere in the top of the triangle.

Also, in certain Sn^{2+} compounds there are indications for a delocalization effect. Consider the sulfate and the bromide. Isomorphous $SnSO_4$ and $BaSO_4$:Sn show very similar absorption and emission spectra. The Stokes shift is large, about 15,000 cm^{-1} (*188*). This indicates strongly localized behavior. However, if we compare the isomorphous couple $SnBr_2$ (*189*) and $PbCl_2$:Sn (*190*), there is a pronounced difference. The isolated Sn^{2+} ion in $PbCl_2$ shows an absorption maximum at 3.8 eV and an emission maximum at 1.8 eV with a large Stokes shift of 2.0 eV. However, in $SnBr_2$ the absorption maximum is at lower energy, viz., 3.4 eV, but the emission at higher: 2.5 eV. The Stokes shift is less than 1 eV. This indicates a delocalization of the Sn^{2+} excited state. Finally, $CsSnBr_3$ is a real semiconductor with its band gap at about 1.5 eV (*191*). The energy bandwidth of the tin ion broadens dramatically in the sequence $SnSO_4$–$SnBr_2$–$CsSnBr_3$, so that the energy gap decreases.

It is clear that this model needs further substantiation. However, it is important to take the present results into account when concentrated systems of optical centers are considered.

VIII. Energy Tranfer and Energy Migration

In Section II,B we considered energy transfer between two species S and A. If we consider now transfer between two identical ions, for example between S and S, the same considerations can be used. If

transfer between two S ions occurs with a high rate, what will happen in a lattice of S ions, for example in a compound of S? There is no reason why the transfer should be restricted to one step, so that we expect that the first transfer step is followed by many others. This can bring the excitation energy far from the site where the absorption took place: energy migration. If in this way the excitation energy reaches a site where it is lost nonradiatively (a killer or quenching site), the luminescence efficiency of that composition will be low. This phenomenon is called concentration quenching. This type of quenching will not occur at low concentrations, because then the average distance between the S ions is so large that the migration is hampered and the killers are not reached.

Energy migration in concentrated systems has been an issue of research in the last decade. Especially since lasers became easily available, the progress has been great. Here we will first consider the case where S is an ion to which the weak-coupling scheme applies. In practice this case consists of the trivalent rare-earth ions. Subsequently we will deal with the case S is an ion to which the intermediate- or strong-coupling scheme applies.

Weak-Coupling Scheme Ions

At first sight transfer between identical rare-earth ions seems to be a process with a low rate, because their interaction will be weak in view of the well-shielded character of the $4f$ electrons. This is in fact true, and transfer is restricted to short distances, that is, of the order of magnitude of 10 Å or less. However, not only are the radiative rates also small, but the spectral overlap can be expected to be large. This is because $\Delta Q = 0$, so that the absorption and emission lines will coincide. In fact energy migration has been observed in many rare-earth compounds, and concentration quenching usually becomes effective for concentrations of a few atomic percent of dopant ions. As an example we mention the transfer rate between Eu^{3+} ions and between Gd^{3+} ions, which may be of the order of $10^7\ s^{-1}$ if the distance is 4 Å or shorter. This has to be compared with a radiative rate of 10^2–$10^3\ s^{-1}$. Consequently, the excitation energy may be transferred more than 10^4 times during its lifetime.

This type of research uses pulsed and tunable lasers as an excitation source. The rare-earth ion is excited selectively, and its decay is analyzed. The shape of the decay curve is characteristic of the physical processes in the compound under study (*9*). For a detailed review the reader is referred to the literature (*8*). Here we give some results for

specific situations. We assume that the object of our study consists of a compound of a rare-earth ion S that contains some ions A that can trap the migrating S excitation energy by SA transfer.

First we consider some Eu^{3+} compounds. In $EuAl_3B_4O_{12}$ there is a three-dimensional Eu^{3+} sublattice with shortest Eu–Eu distance equal to 5.9 Å. At 4.2 K there is no energy migration, but at 300 K it occurs. The temperature dependence of the Eu–Eu energy transfer is exponential, with $\Delta E \sim 240\ cm^{-1}$ (*192*). This is because the $^5D_0$-$^7F_0$ transition is forbidden under the relevant site symmetry (D_3), so that the multipole interactions vanish. The distance of 5.9 Å is prohibitive for transfer by exchange interaction. At higher temperatures the $^7F_1$ level is thermally populated and multipolar interaction becomes effective. The experimental value of ΔE corresponds to the energy difference $^7F_0$ - $^7F_1$. The excitation energy makes 1400 jumps during its lifetime at 300 K with a diffusion length of 230 Å.

Samples of $EuAl_3B_4O_{12}$ that are so pure that the excited state does not reach a killer site during its lifetime show efficient luminescence. Samples with a certain concentration of killer sites do not emit at 300 K. For example, crystals of $EuAl_3B_4O_{12}$, grown from a K_2SO_4/MoO_3 flux, do not luminescence, since the excitation energy is trapped by the Mo^{3+} impurities (concentration 25 ppm). The migration brings all of the excitation energy to a nonradiative sink. At 4.2 K the migration is hampered and luminescence occurs.

A very exceptional case of energy migration in a Eu^{3+} compound was recently reported by Bettinelli et al. (*193*). These authors studied $Cs_2NaEuCl_6$ in which the Eu^{3+} ion occupies a site with perfect octahedral symmetry in which the pure electronic transitions are completely forbidden as electric-dipole transitions. Nevertheless the very forbidden $^7F_0$–$^5D_0$ transition was observed in the excitation spectra. The electronic origin is weak, but sharp and clear, and is accompanied by much stronger vibronic transitions. This suggests that the authors have observed here one of the rare examples of an electric quadrupole transition.

They observed for $Cs_2NaEuCl_6$, even at very low temperatures, energy migration over the Eu^{3+} sublattice. The Eu–Eu distance (7.6 Å) is too long to allow energy transfer by exchange, so that we probably have to do with energy transfer by electric quadrupole-quadrupole interaction. In this aspect $Cs_2NaEuCl_6$ behaves similarly to $Cs_2UO_2Cl_4$ for which Denning et al. (*194*) have shown that electric quadrupole transitions are also of importance.

Two-dimensional energy migration was observed for $NaEuTiO_4$ (*195*) and $EuMgAl_{11}O_{19}$ (*196*). One-dimensional energy migration was ob-

served for $EuMgB_5O_{10}$ (*197*) and $Li_6Eu(BO_3)_3$ (*198*). This fits the crystallographic data and was derived from the decay curve of the intrinsic Eu^{3+} emission.

In EuP_3O_9 a transition from one- to three-dimensional migration was observed, because this compound shows a phase transition (*199*).

The situation in Eu^{3+} compounds can be characterized as follows:

a. For Eu–Eu distances larger than 5 Å exchange interaction becomes ineffective. Only multipolar ineractions can be of importance, and they are weak anyhow. If sufficiently pure, compounds in this class will luminesce efficiently. Examples are $EuAl_3B_4O_{12}$, $Eu(IO_3)_3$, and $CsEuW_2O_8$.

b. For Eu–Eu distances smaller than 5 Å, exchange interaction is effective. Examples are the intrachain migration in $EuMgB_5O_{10}$ and $Li_6Eu(BO_3)_3$, and the migration in Eu_2O_3 (*200*).

Recently there has been a lot of interest in energy migration in Gd^{3+} compounds, because this opens interesting possibilities to obtain new, efficient luminescent materials (*201, 202*). The Gd^{3+} sublattice is sensitized and activated. The sensitizer efficiently absorbs ultraviolet radiation and transfers this to the Gd^{3+} sublattice. By energy migration in this sublattice the activator is fed and emission results. Absorption and quantum efficiencies of over 90% have been attained. The physical processes can be schematically presented as follows:

$$\xrightarrow{\text{excitation}} S \longrightarrow Gd^{3+} \xrightarrow{n\times} Gd^{3+} \longrightarrow A \xrightarrow{\text{emission}} \qquad (15)$$

Here $n\times$ indicates that the Gd–Gd transfer step is performed n times. A suitable choice of S is Ce^{3+}, Bi^{3+}, Pr^{3+}, or Pb^{2+}. For A there are many possibilities: Sm^{3+}, Eu^{3+}, Tb^{3+}, Dy^{3+}, Mn^{2+}, UO_6^{6-}, and probably many more.

Here we consider one example more in detail, viz., $NaGdF_4$:Ce,Tb (*203*). Ce^{3+} excitation results in predominantly Tb^{3+} emission. Table IX gives some of the rates of importance in this system. Figure 41 indicates the several transfer and radiative rates.

An interesting aspect of energy migration in concentrated rare-earth compounds is the influence of the magnetic order that occurs in some cases on the migration process. This has been studied on compounds of Gd^{3+} and Tb^{3+} by Jacquier et al. (*204–206*). As an example we mention $GdAlO_3$ and $TbAlO_3$, which become antiferromagnetic at 3.9 K and 3.8 K, respectively. In the paramagnetic phase the experimental decays are in agreement with fast-diffusion energy transfer. Below the Néel

TABLE IX

ENERGY TRANSFER AND RADIATIVE RATES IN THE SYSTEM $NaY_{0.98-x}Gd_xCe_{0.01}Tb_{0.01}F_4$[a]

Probability[b]	Value in $NaGdF_4$ (s^{-1})
P_1	$(4 \pm 1)10^7$
P_2	10^8
P_3	130
P_4	$10^{7\pm1}$
P_5	0
P_6	4×10^5
P_7	250

[a] At room temperature; excitation is into the Ce^{3+} ion; the transfer rates are given for nearest neighbor distances. (After ref. *203*).

[b] Cf. Fig. 41.

temperature, however, the decays are no longer exponential and are considerably slower. The migration has become diffusion limited. The diffusion constants reported are 1.6×10^{-9} cm^2 s^{-1} at 4.4 K for both compounds, but only 8×10^{-12} cm^2 s^{-1} and 8×10^{-14} cm^2 s^{-1} at 1.6 K for $GdAlO_3$ and $TbAlO_3$, respectively.

In the antiferromagnetic phase the migration of excitation energy is slowed down, because nearest neighbor Gd^{3+} (or Tb^{3+}) ions are oriented antiparallel, which makes energy transfer by exchange interaction impossible.

In $EuAlO_3$ such an effect does not occur. The Eu^{3+} ions (ground state $^7F_0$) do not carry a magnetic moment. This compound is another example of a Eu^{3+} compound in which energy migration occurs down to the lowest temperatures (*204*) due to exchange interaction (*207*).

Let us now turn to energy migration in concentrated systems for which the weak-coupling scheme is no longer valid. In compounds of

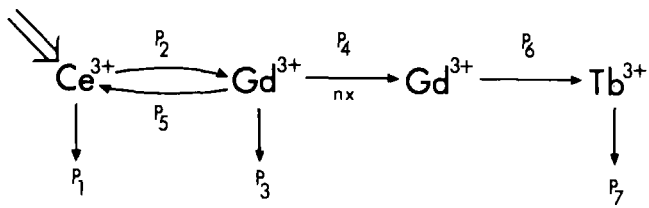

FIG. 41. Energy tranfer processes in gadolinium compounds.

ions that belong to the strong-coupling scheme the situation is completely different from that in rare-earth compounds (*8*). In the former, excitation of the luminescent center results in strong relaxation of the excited state. This brings the excited state out of resonance with the neighbors in the ground state, and as a consequence energy transfer becomes impossible, especially at low temperatures. In the expression for the transfer rate the spectral overlap vanishes, so that the transfer rate becomes very low. In practice this can be measured by the Stokes shift: If the Stokes shift is large, the transfer rate will be low; if the Stokes shift is small, the transfer rate has a value that can compete with the radiative rate. It should be kept in mind that an increasing Stokes shift implies simultaneously an increase of the nonradiative rate for return to the ground state, as argued above.

Let us start this section with some examples of luminescent compounds of ions for which the strong-coupling scheme is clearly valid. These are compounds like vanadates and tungstates (*96*). They contain oxidic anions with a central metal ion that has lost all its *d* electrons. Examples are VO_4^{3-}, MoO_4^{2-}, WO_4^{2-}, and WO_6^{6-}. The Stokes shift of their emission is large (~15,000 cm^{-1}). An example of this type of spectra was given in Fig. 4. Energy migration is hampered, often even up to room temperature. A more-or-less classic example is $CaWO_4$, which is an efficient X-ray phosphor, well-known for 70 years. Also, the new X-ray phosphors $YTaO_4$ and $LuTaO_4$ belong to this class (*208*). In these compounds the tungstate or tantalate group shows luminescence on excitation. There is no migration of the excitation energy over the host lattice. However, as mentioned in the introduction, the quantum efficiency of the luminescence does not reach 100%, not even at 4.2 K, because the large parabolas offset (ΔQ) results in a certain amount of nonradiative loss that occurs without thermal activation.

In other compounds energy migration occurs at room temperature, for example YVO_4 and Ba_2MgWO_6. They have a smaller Stokes shift, viz., some 10,000 cm^{-1}. It is this property that makes YVO_4–Eu^{3+} an efficient phosphor at room temperature (but not at low temperatures): excitation into the vanadate group is followed by energy migration to Eu^{3+} centers.

There are other luminescent centers, like Ce^{3+} and Bi^{3+}, that belong either to the strong-coupling scheme or to the weak(er)-coupling scheme, depending on the host lattice. This can be seen immediately from the Stokes shift. The Bi^{3+} ion is a very impressive example, because the Stokes shift of its luminescence is more dependent on the surroundings than that of any other luminescent ion (see Table VIII). Figure 42 shows the large difference between the spectral shape of the

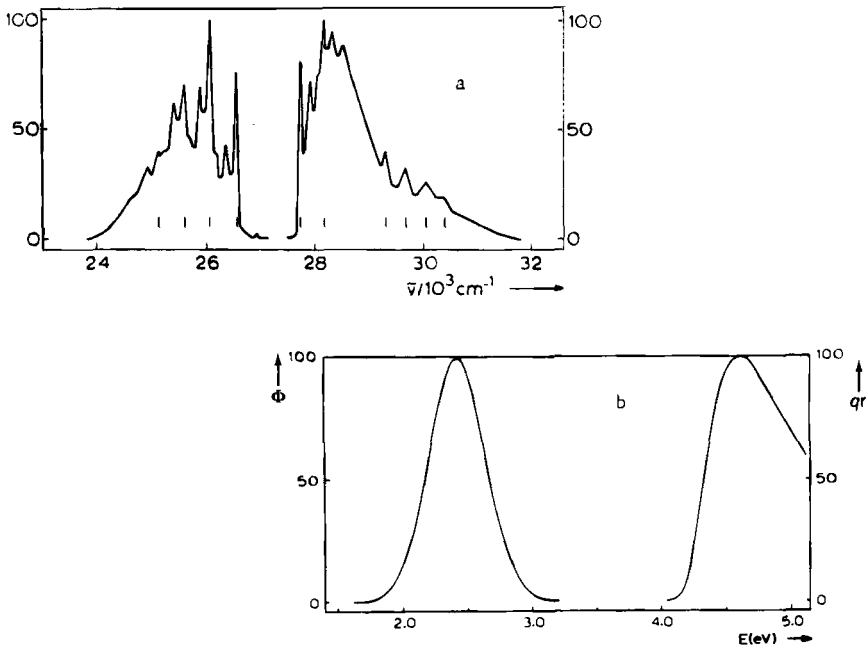

FIG. 42. Emission and excitation spectra (a) at 4.2 K of $NaYO_2$:Bi and (b) $Bi_2Al_4O_9$.

emission bands of Bi^{3+} in several compounds. The strong-coupling case (e.g., $Bi_2Al_4O_9$) shows (a) broadband emission; the weak-coupling case (e.g., $NaYO_2$–Bi^{3+} shows (b) narrowband emission with vibrational structure at low temperatures.

The marked dependence of the Stokes shift on the host lattice is related to the electronic configuration of the ground state of the Bi^{3+} ion. (See Section VII). For large Stokes shifts the nonradiative transition rates start to compete with the radiative ones: $LaPO_4$–Bi is quenched at about 100 K. It is illustrative to consider the luminescence of the bismuth compounds. If the Stokes shift is relatively small, the concentrated system is quenched. Concentration quenching in the systems $Cs_2NaY_{1-x}Bi_xCl_6$ and $Y_{1-x}Bi_xAl_3B_4O_{12}$, for example, occurs at 300 K for $x < 0.01$. The Bi^{3+}–Bi^{3+} energy transfer occurs over large distances of several tens of angstroms. If the Stokes shift is larger, efficiently emitting bismuth compounds result. A good example is $Bi_4Ge_3O_{12}$. Although chemically completely different from $CaWO_4$, the physics of their luminescence is very similar: In both cases an enormous reorganization occurs after excitation. Actually, $Bi_4Ge_3O_{12}$ was first

proposed as an X-ray phosphor, but presently it is applied in the L3 experiment at CERN in Geneva which needs 12,000 large single crystals of $Bi_4Ge_3O_{12}$.

If the Stokes shift becomes too large ($Bi_2Ge_3O_9$ 20,000 cm^{-1}), the compound is no longer luminescent at room temperature due to intracenter nonradiative transitions. Note, therefore, that the reason $Cs_2NaBiCl_6$, for example, is quenched is completely different from the reason $Bi_2Ge_3O_9$ is quenched (migration to killer centers vs. intra-Bi^{3+} nonradiative loss).

In conclusion, there are several types of nonradiative processes in luminescent materials. The two most important ones are energy transfer between two luminescent centers and intracenter nonradiative decay. The former are reasonably well understood and predictable. The latter are only understood and predictable in the case of ions for which the weak-coupling scheme is valid. For the others it is nevertheless possible to arrive at reasonable predictions by applying simple models to a series of luminescent compositions (see Section IV).

IX. Luminescent Centers as Probes

In many cases of a different nature a luminescent center can be used as a probe of its direct surroundings. Here we will consider some new examples.

In this laboratory we have studied the luminescence of rare-earth ions on porous glass. This is a glass with a narrow pore-size distribution (*209*). Aqueous solutions of rare-earth salts are brought into contact with the porous glass. After removal of the solution the spectral properties are measured. Figure 43 shows the emission spectrum of Gd^{3+} on porous glass (*210*). The main emission line is $^6P_{7/2} \rightarrow {}^8S$. It carries a few vibronic transitions. These involve a.o. vibrational frequencies of 1090 cm^{-1} and 3280 cm^{-1}. They have to be assigned to the silicate group that is present in the glass and to H_2O. In this way the Gd^{3+} ion is found to occupy a position directly on the glass surface, because otherwise the coupling with the silicate vibration is not possible. It is also clear that the water molecules are coordinated to the other side of the Gd^{3+} ion.

A comparable situation in a completely different system is the emission spectrum of [$Gd^{3+} \subset$ 2.2.1] (*211*). In addition to vibronic lines related to the vibrations of the cryptand, there are vibronic lines due to the presence of H_2O. This shows that the cage-like ligand does not shield completely from the hydrate water molecules, but that the molecules participate in the Gd^{3+} coordination. This has no consequences for

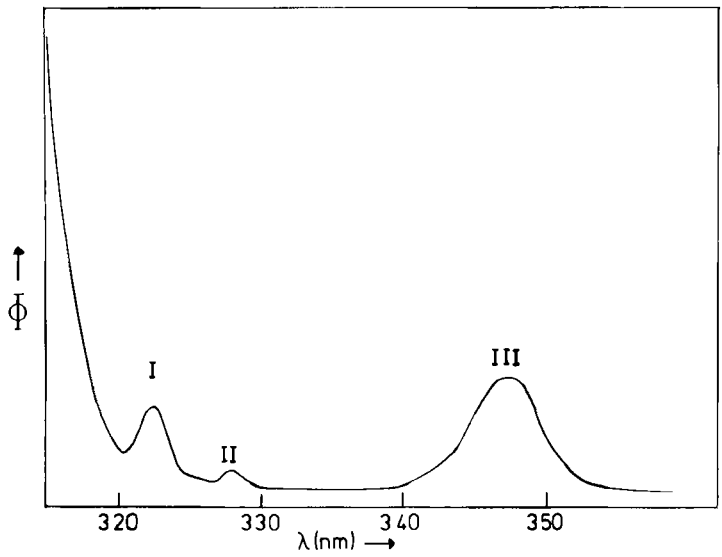

FIG. 43. Emission spectrum of Gd^{3+} on porous glass. Vibronics are indicated.

the quantum efficiency of the Gd^{3+} luminescence, but in case of the Tb^{3+} and especially Eu^{3+} cryptate these water molecules are responsible for a drastic reduction of the quantum efficiency (*212, 213*), as discussed in Section IV.

The emission spectrum of [$Gd^{3+} \subset$ 2.2.1] could only be obtained with high enough intensity under X-ray excitation (*211*). This is due to the weak absorption strength of the Gd^{3+} lines. The analogous [$Eu^{3+} \subset$ 2.2.1] shows, under X-ray excitation, a considerable amount of [$Eu^{2+} \subset$ 2.2.1] emission (*211*). Since the formation of the divalent species under the applied synthesis conditions is very improbable, this [$Eu^{2+} \subset$ 2.2.1] emission shows that under X-ray excitation electrons are trapped at the europium ions.

In this laboratory we have also studied the role of lanthanide ions in gypsum, $CaSO_4 \cdot 2H_2O$ (*214*). This material plays an important role in industrial waste streams. It is important to know the impurities present. Only small amounts of lanthanide ions can be solved in the gypsum lattice. This lattice consists of $CaSO_4$ layers separated by H_2O layers. The Ca^{2+} ions are surrounded on one side by sulfate ions and on the other side by water molecules.

Luminescence spectroscopy of, for example, $CaSO_4 \cdot 2H_2O{:}Eu^{3+}$ and $CaSO_4 \cdot 2H_2O{:}Gd^{3+}$ shows the following. The crystallites are covered with a second phase, which turns out to be $NaLn(SO_4)_2 \cdot H_2O$ (Ln = Eu,

Gd). Part of the lanthanide ions occupy Ca^{2+} sites. The emission spectrum of $CaSO_4 \cdot 2H_2O{:}Gd^{3+}$ shows vibronic transitions involving the sulfate as well as the water ligands. The emission spectrum of $CaSO_4 \cdot 2H_2O{:}Eu^{3+}$ shows an intense $^5D_0$–$^7F_0$ transition, indicating a strong linear crystal-field component (see Fig. 44). This is due to the layer-like structure, which implies a different coordination of the Eu^{3+} ion on the two sides. Finally the Eu^{3+} emission shows a weak quantum efficiency due to nonradiative losses to the surrounding water molecules.

Although the rare-earth ions offer many other examples, we prefer to discuss another example from a different field, viz., the use of luminescence as a probe of the transition crystalline → liquid crystalline (*215*). In peripherally octa-*n*-dodecoxy substituted phthalocyanine the optically active phthalocyanine groups are stacked in linear columns. This compound contains, due to the synthesis procedure, low amounts of copper phthalocyanine that act as quenching centers of the luminescence. In the crystalline modification there is an angle between the flat, optically active groups. This angle disappears at the transition to the liquid-crystalline state (at about 360 K). At 4.2 K the quantum efficiency of this polymer is higher than 50%. Migration over the phthalocyanine molecules to the quenching centers is obviously not of large importance. The emission, a broad band with a maximum at about 800 nm, is due to phthalocyanine molecules, of which at least a part is slightly disturbed. At higher temperatures the migration becomes

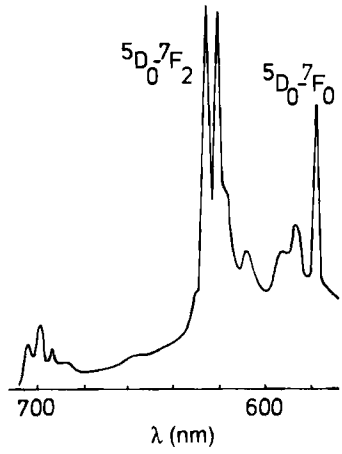

FIG. 44. Emission spectrum of $CaSO_4 \cdot 2H_2O{:}Eu^{3+}$.

faster and more quenching sites are reached, so that the efficiency drops.

Interestingly enough there is another sharp drop in luminescence intensity at the transition to the liquid-crystalline phase (*215*). This is shown in Fig. 45. In the latter phase there is an orientation of the phthalocyanine molecules that is more favorable for migration, so that more quenching centers are reached. The transition shows hysteris (Fig. 45) and coincides with thermodynamic measurements. Therefore the luminescence is used to "probe" the crystalline to liquid-crystalline transition. A further analysis yielded an estimation of the number of phthalocyanine molecules in the stack.

Here we wish to report that this model was further confirmed by changing the crystalline structure in such a way that the phthalocyanine molecules could be expected to be oriented parallel. This can be done in two ways. First a silicon phthalocyanine is prepared (*216*). The optical molecules are now kept together by a $(Si–O–Si–O)_n$ chain (see Fig. 46). As is to be expected the migration in this crystalline phase is very fast and even at 4.2 K the luminescence intensity is very low.

In another synthesis the phthalocyanine molecules are polymerized via groups at the end of the side chains (*217*). This polymer also shows hardly any luminescence at 4.2 K.

Applications in the analytical field are often based on the use of luminescent centers as probes. In our study of rare-earth ions in $GdAlO_3$, for example, we are not able to observe rare-earth emission

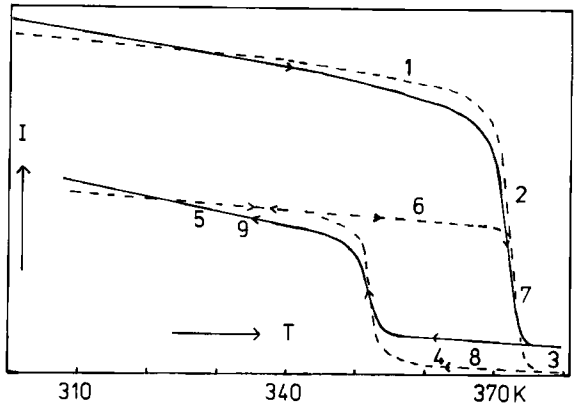

FIG. 45. Luminescence intensity of substituted phthalocyanine stacks around the solid → mesophase transition. At the transition temperature the intensity drops strongly.

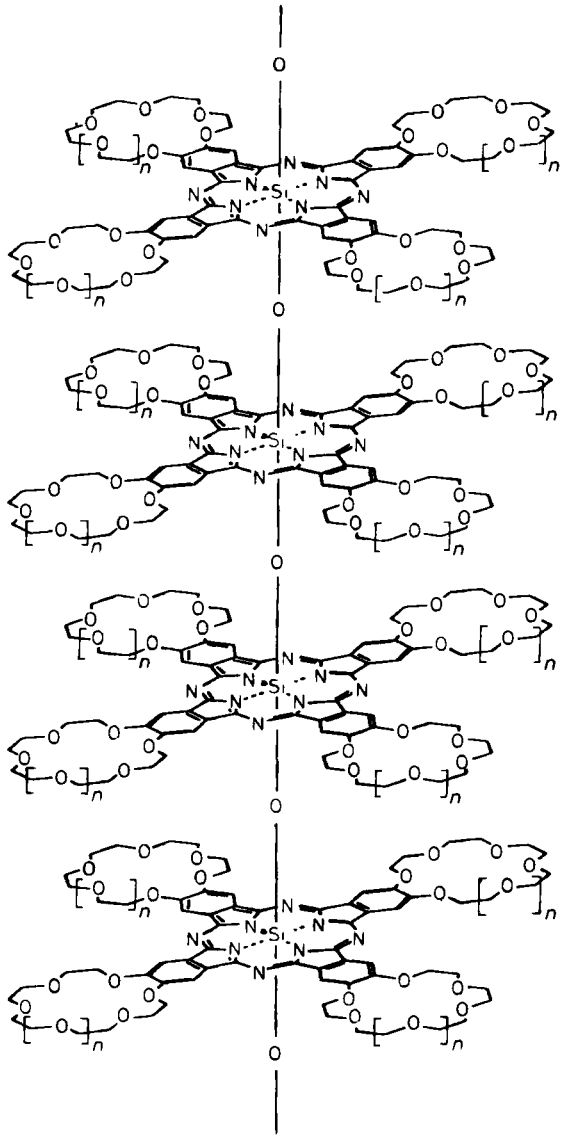

FIG. 46. Linear chain of coupled phthalocyanine molecules.

alone (*218*). There is always Cr^{3+} emission present if excitation is in the ultraviolet. The reason is that the Gd^{3+} ion is excited. This is followed by energy migration over the Gd^{3+} sublattice. The Cr^{3+} ion, present as an impurity, is very effective in trapping this excitation energy. Actually every ion able to trap excitation energy that was absorbed elsewhere is a potential analytical probe. Due to the concentration of the excitation energy in a few centers, the sensitivity is in principle high.

A recent example of this consideration is the success of $[Eu^{3+} \subset bpy.bpy.bpy]$ cryptate in luminescence immunoassay (*104*). This cryptate is used as a label to an antibody that is coupled in a specific way to a biomolecule, the presence of which has to be proved. The structure of the molecule is shown in Fig. 47. Excitation is into the bpy molecule, which shows a very high absorption strength in the ultraviolet part of the spectrum ($\epsilon_{max} \sim 10^4\ M^{-1}\ cm^{-1}$). From the bpy triplet state the energy is transferred to the Eu^{3+} ion, which finally emits (*104, 107*). Although the quantum efficiency is only 1% (*104*), the high bpy absorption strength makes application feasible.

Interestingly enough $[Tb^{3+} \subset bpy.bpy.bpy]$ only shows efficient Tb^{3+} emission on bpy excitation below 100 K (*107*). At room temperature backtransfer occurs. There is thermal equilibrium between the bpy triplet state and the Tb^{3+} $^5D_4$ state. Due to the rates involved, nonradiative decay from the triplet level prevails (*219, 220*). This is outlined in Fig. 48. In the solid state the same situation prevails, but the nonradiative rate is now ascribed to energy migration over the bpy molecules to quenchers (107).

X. New Luminescent Materials

We have recently reviewed the new luminescent materials of the last decade (*2*). Therefore we give here only a short summary:

a. Gadolinium compounds form the basis for very efficient lamp

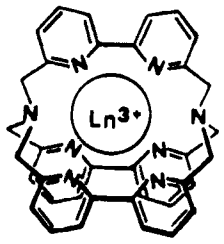

FIG. 47. $[Ln^{3+} \subset bpy \cdot bpy \cdot bpy]$ cryptate (Ln = lanthanide).

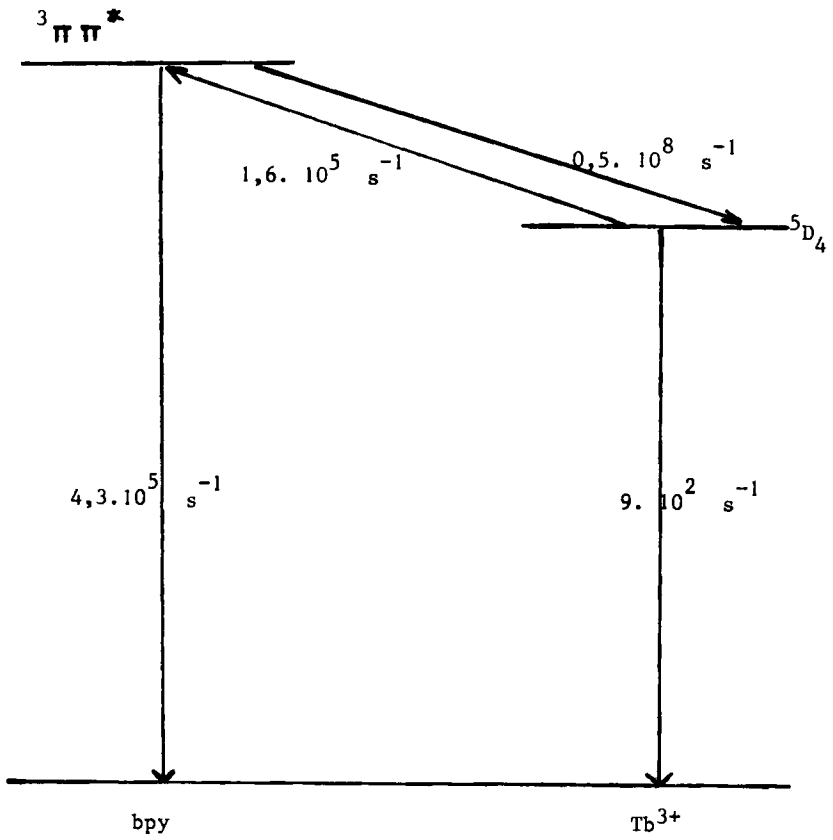

FIG. 48. Energy level scheme for [$Tb^{3+} \subset$ bpy · bpy · bpy] cryptate.

phosphors. Of great importance is the migration of excitation energy to the luminescent center. This was discussed above.

b. Gadolinium compounds also form the basis for phosphors for X-ray photography.

c. Eu^{2+}-activated compounds ($BaFBr:Eu^{2+}$, $Ba_5(SiO_4)Br_6:Eu^{2+}$) are efficient X-ray storage phosphors for digital radiography.

d. $Bi_4Ge_3O_{12}$ (BGO) is a very good scintillator material used for the detection of high-energy particles at CERN (Geneva).

e. Eu^{3+}-cryptates are used in luminescence immunoassay.

f. Cathode-ray phosphors can be used under high excitation density (projection television), for example, $InBO_3:Tb$.

g. Luminescent glasses and glass ceramics are used as laser materials or solar concentrator material.

h. Broadband emitting crystals are used in tunable lasers (low-field Cr^{3+}).

i. Crystals showing cross-over transitions (for example, BaF_2) are used in positron emission tomography.

XI. Conclusion

The study of optical centers and the influence of their immediate surroundings on their properties has proceeded successfully during the last decade. Not only has new fundamental knowledge been obtained, but also many new applications have been proposed and realized. The border lines between the different fields in which these centers are investigated, viz., the nonmolecular solid state, the molecular state (as solid or as solution), and the biochemical molecular state, are slowly fading. Stronger interactions between these fields might well be profitable to all of them.

References

1. Imbusch, G. F., *in* "Lasers, Spectroscopy and New Ideas" (W. M. Yen and M. D. Levenson, eds.), p. 248. Springer-Verlag, Berlin, 1988.
2. Blasse, G., *Chem. Mater.* **1,** 294 (1989).
3. Blasse, G., *Mater. Chem. Phys.* **16,** 3,4 (1987).
4. Di Bartolo, B., "Optical Interactions in Solids." Wiley, New York, 1968.
5. Di Bartolo, B., and Powell, R. C., "Phonons and Resonances in Solids." Wiley, New York, 1976.
6. Di Bartolo, B., ed. "Optical Properties of Ions in Solids." Wiley, New York, 1975.
7. G. F., Imbusch, *in* "Luminescence Spectroscopy," (M. D. Lumb, ed.), Ch. 1. Academic Press, London, 1978.
8. Di Bartolo, B., ed. "Energy Transfer Processes in Condensed Matter." Plenum Press, New York, 1984.
9. Holstein, T., Lyo, S. K., and Orbach, R., *in* "Laser Spectroscopy of Solids" (W. M. Yen and P. M. Selzer, eds.), p. 39. Springer-Verlag, Berlin, 1981.
10. Weber, M. J., *in* "Laser Spectroscopy of Solids" (W. M. Yen and P. M. Selzer, eds.) p. 189. Springer-Verlag, Berlin, 1981.
11. Di Bartolo, B., ed. "Radiationless Processes." Plenum Press, New York, 1980.
12. van Dijk, J. M. F., and Schuurmans, M. F. H., *J. Chem. Phys.* **78,** 5317 (1983).
13. Blasse, G., *in* "Energy Transfer Processes in Condensed Matter," p. 255. Plenum, New York, 1984.
14. Auzel, F., *in* "Radiationless Processes," p. 213. Plenum, New York, 1980.
15. Berdowski, P. A. M., Lammers, M. J. J., and Blasse, G., *Chem. Phys. Lett.* **113,** 387 (1985).
16. Vial, J. C., and Buisson, R., *J. Phys. Lett.* **43,** L745 (1982).
17. Blasse, G., and Bril, A., *Philips Techn. Rev.* **31,** 304 (1970).
18. Lever, A. B. P., "Inorganic Electronic Spectroscopy," 2nd ed. Elsevier, Amsterdam, 1984.

19. Reber, C., and Güdel, H. U., *Inorg. Chem.* **25,** 1196 (1986).
20. Gälli, B., Hauser, A., and Güdel, H. U., *Inorg. Chem.* **24,** 2271 (1985).
21. Reber, C., and Güdel, H. U., *Chem. Phys. Lett.* **154,** 425 (1989).
22. Jacobsen, S. M., Smith, W. E., Reber, C., and Güdel, H. U., *J. Chem. Phys.* **84,** 5205 (1986); Jacobsen, S. M., and Güdel, H. U., *J. Lumin.* **43,** 125 (1989).
23. Herren, M., Jacobsen, S. M., Güdel, H. U., and Briat, B., *J. Chem. Phys.* **90,** 663 (1989).
24. Dubicki, L., Kramer, E., Riley, M., and Yamada, I., *Chem. Phys. Lett.* **157,** 315 (1989).
25. Matthies, H., Recker, K., Wallrafen, F., Dirksen, G. J., and Blasse, G., *Chem. Phys. Lett.* **149,** 167 (1988).
26. Faber, A. J., van Die, A., Blasse, G., and van der Weg, W. F., *Phys. Chem. Glasses* **28,** 150 (1987).
27. van Die, A., Leenaers, A. C. H. I., van der Weg, W. F., and Blasse, G., *Mater. Res. Bull.* **22,** 781 (1987).
28. Petermann, K., and Huber, G., *J. Lumin.* **31, 32,** 71 (1984).
29. See, e.g., Dieke, G. H., "Spectra and Energy Levels of Rare Earth Ions in Crystals." Wiley, New York, 1968.
30. Carnall, W. T., Goodman, G. L., Rajnak, K., and Rana, R. S., *J. Chem. Phys.* **90,** 3443 (1989).
31. Szczurek, T., and Schlesinger, M., *in* "Rare Earths Spectroscopy" (B. Jezowska-Trzebiatowska, J. Legendziewicz, and W. Strek, eds.). p. 309. World Scientific, Singapore, 1985.
32. Blasse, G., *J. Phys. Chem Solids* **50,** 99 (1989).
33. Brixner, L. H., and Blasse, G., *Chem. Phys. Lett.* **157,** 283 (1989).
34. Blasse, G., and Brixner, L. H., *J. Electrochem. Soc.* **136,** 3529 (1989).
35. Chien, R. L., Berg, J. M., McClure, D. S., Rabinowitz, P., and Perry, B. N., *J. Chem. Phys.* **84,** 4168 (1986).
36. Bleijenberg, K. C., Kellendonk, F., and Struck, C. W., *J. Chem. Phys.* **73,** 3586 (1980).
37. Downer, M. C., and Bivas, A., *Phys. Rev.* **B28,** 3677 (1983).
38. Downer, M. C., Cordero-Montalvo, C. D., and Crosswhite, H., *Phys. Rev.* **B28,** 4931 (1983).
39. Rana, R. S., Cordero-Montalvo, C. D., and Bloembergen, N., *J. Chem. Phys.* **81,** 2951 (1984); *Phys. Rev.* **B30,** 438 (1984).
40. Gayen, S. K., and Hamilton, D. S., *Phys. Rev.* **B28,** 3706 (1983).
41. Hölsä, J., *Chem. Phys. Lett.* **112,** 246 (1984).
42. Linares, C., Jung, P., Boulon, G., and Gaume, F., *J. Less-Common Metals* **93,** 89 (1983).
43. Auzel, F., *in* "Radiationless Processes," p. 213. Plenum, New York, 1980.
44. Piper, W. W., Deluca, J. A., and Ham, F. S., *J. Lumin.* **8,** 344 (1974); Sommerdijk, J. L., Bril, A., and de Jager, A. W., *J. Lumin.* **8,** 341 (1974) and **9,** 288 (1974).
45. Hamilton, D. S., Gayen, S. K., Pogatshnik, G. J., and Ghen, R. D., *Phys. Rev.* **B39,** 8807 (1989).
46. Pogatshnik, G. J., and Hamilton, D. S., *Phys. Rev.* **B36,** 8251 (1987).
47. Lim, K. S., and Hamilton, D. S., *J. Lumin.* **40, 41,** 319 (1988).
48. Pedrini, C., Rogemond, F., and McClure, D. S., *J. Appl. Phys.* **59,** 1196 (1986).
49. Caird, J. A., Payne, S. A., Staver, P. R., Ramponi, A. J., Chase, L. L., and Krupke, W. F., *IEEE J. Quantum Electr.* **24,** 1077 (1988).
50. Petermann, K., Clausen, R., Heumann, E., and Ledig, M., *Opt. Commun.* **70,** 483 (1989).

51. Jørgensen, C. K., "Absorption Spectra and Chemical Bonding in Complexes." Pergamon Press, Oxford, 1962.
52. Chermette H., and Pedrini, C., *J. Chem. Phys.* **75,** 1869 (1981); Pedrini, C., *Phys. Stat. Sol. (b)* **87,** 273 (1978).
53. Blasse, G., and McMillin, D. R., *Chem. Phys. Lett.* **70,** 1 (1980).
54. Doumerc, J. P., Parent, C., Chao, Z. J., Le Flem, G., and Ammar, A., *C.R. Acad. Sci. Paris, Série II,* **306,** 1431 (1988).
55. McGlynn, S. P., Azumi, T., and Kumar, D., *Chem. Revs.* **81,** 475 (1981).
56. Maria, H. J., Wahlborg, A., and McGlynn, S. P., *J. Chem. Phys.* **49,** 4925 (1968).
57. Blasse, G., and Dirksen, G. J., *J. Phys. Chem.* **91,** 20 (1987).
58. Day, P., *Int. Revs. Phys. Chem.* Butterworths, London, **1,** 149 (1981).
59. Brown, D. B., ed., "Mixed-Valence Compounds." D. Reidel, Dordrecht, 1980.
60. Stevenson, K. L., Braun, J. L., Davis, D. D., Kurtz, D. S., and Sparks, R. I., *Inorg. Chem.* **27,** 3472 (1988).
61. Debnath, R., and Das, S. K., *Chem. Phys. Lett.* **155,** 52 (1989).
62. Wanmaker, W. L., and Bakker, C., *J. Electrochem. Soc.* **106,** 1027 (1959); Wanmaker, W. L., and Spier, H. L., *J. Electrochem. Soc.* **109,** 109 (1962).
63. Huimin, L., and Fuxi, G., *J. Non-cryst. Solids* **80,** 447 (1986).
64. Pedrini, C., and Jacquier, B., *J. Phys. C.: Solid State Phys.* **13,** 4791 (1980).
65. Barrie, J. D., Dunn, B., Hollingworth, G., and Zink, J. I., *J. Phys. Chem.* **93,** 3958 (1989).
66. Knotter, D. M., Blasse, G., van Vliet, J. P. M., and van Koten, G., to be published.
67. Radjaipur, M., and Oelkrug, D., *Ber. Bunsenges. Phys. Chem.* **82,** 159 (1978).
68. Blasse, G., Breddels, P. A., and McMillin, D. R., *Chem. Phys. Lett.* **109,** 24 (1984).
69. Kittel, C., "Solid State Physics," 5th ed. Wiley, New York, 1976.
70. Mumm, H. C., and Müller-Buschbaum, H. K., *J. Less-Common Met.* **142,** 85 (1988).
71. Marinder, B. O., and Wahlström, E., *Chem. Scr.* **23,** 157 (1984).
72. Binsma, J. J. M., Thesis, University of Nijmegen, 1981.
73. Seraphin, B. O., ed. *Top. Appl. Phys.* **31,** 237 (1979).
74. Vogler, A., and Kunkely, H., *Chem. Phys. Lett.* **158,** 74 (1989).
75. Valbis, Ya. A., Rachko, Z. A., and Yansons, Ya. L., *JETP Lett.* **42,** 172 (1985); Aleksandrov, Yu. M., Makhov, V. N., Rodnyl, P. A., Syreinshchikova, T. I., and Yakimenko, M. N., *Sov. Phys. Sol. State* **26,** 1734 (1984); Schotanus, P., van Eijck, C. W. E., Hollander, R. W., and Pijpelink, J., *Nucl. Instrum. Methods* **A238,** 564 (1984).
76. Valbis, Ya. A., Rachko, Z. A., and Yansons, Ya. L., *Opt. Spectrosc.* (USSR) **60,** 679 (1986).
77. Jansons, J. L., Krumins, V. J., Rachko, Z. A., and Valbis, J. A., *Solid State Commun.* **67,** 183 (1988).
78. Valbis, Ya. A., Rachko, Z. A., and Yansons, Ya. L., *Opt. Spectrosc.* (USSR) **64,714 (1988).**
79. Fano, U., and Cooper, J. W., *Phys. Rev.* **137,** A 1364 (1965).
80. Sturge, M. D., Guggenheim, H. J., and Pryce, M. H. L., *Phys. Rev. B2,* 2459 (1970).
81. Lempicki, A., Andrews, L., Nettel, S. J., and McCollum, B. C., *Phys. Rev. Lett.* **44,** 1324 (1980).
82. Meijerink, A., and Blasse, G., *Phys. Rev. B.* **40,** 7288 (1989).
83. Meijerink, A., Nuyten, J., and Blasse, G., *J. Lumin.* **44,** 19 (1989).
84. See, e.g., Nozik, A. J., Williams, F., Nenadovic, M. T., Rajh, T., and Micic, O. I., *J. Phys. Chem.* **89,** 397 (1985).
85. Weller, H., Koch, U., Gatierrez, M., and Henglein, A., *Ber. Bunsen-Ges. Phys. Chem.* **88,** 649 (1984).

86. Wang, Y., and Herron, N., *J. Phys. Chem.* **92,** 4988 (1988).
87. Herron, N., Wang, Y., Eddy, M. M., Stucky, G. D., Cox, D. E., Moller, K., and Beitz, T., *J. Am. Chem. Soc.* **111,** 530 (1989).
88. Dameron, C. T., Reese, R. N., Mehra, R. K., Kortan, A. R., Carroll, P. J., Steigerwalt, M. L., Bras, L. E., and Winge, D. R., *Nature (London)* **338,** 596 (1989).
89. Grätzel, M., *Nature (London)* **338,** 540 (1989).
90. Carnall, W. T., *in* "Handbook on the Physics and Chemistry of Rare Earths" (K. A. Gschneidner Jr. and Le Roy Eyring, eds.), Ch. 24. North-Holland, Amsterdam, 1979.
91. Zhiran, H., and Blasse, G., *J. Solid State Chem.* **52,** 130 (1984).
92. Blasse, G., Dirksen, G. J., and van Vliet, J. P. M., *Recl. Trav. Chim. Pays-Bas Belg.* **107,** 138 (1988).
93. Berdowski, P. A. M., and Blasse, G., *Chem. Phys. Lett.* **107,** 351 (1984).
94. Kiliaan, H. S., Meijerink, A., and Blasse, G., *J. Lumin.* **35,** 155 (1986); *Mat. Chem. Phys.* **18,** 155 (1987), **18,** 351 (1987).
95. de Vries, A. J., Hazenkamp, M. F., and Blasse, G., *J. Lumin.* **42,** 275 (1988).
96. Blasse, G., *Struct. Bonding* **42,** 1 (1980).
97. de Hair, J. Th. W., and Blasse, G., *J. Lumin.* **14,** 307 (1976).
98. van Oosterhout, A. B., *Phys. Stat. Sol. (a)* **41,** 607 (1977).
99. Bleijenberg, K. C., and Breddels, P. A., *J. Chem. Phys.* **72,** 3539 (1980).
100. Blasse, G., van Vliet, J. P. M., Verwey, J. W. M., Hoogendam, R., and Wiegel, M., *J. Phys. Chem. Solids,* **50,** 583 (1989).
101. Blasse, G., Piffard, Y., and Struye, L., *Chem. Phys. Lett.* **147,** 514 (1988).
102. Worl, L. A., and Meijer, T. J., *Chem. Phys. Lett.* **143,** 541 (1988).
103. Blasse, G., Dirksen, G. J., Sabbatini, N., and Perathoner, S., *Inorg. Chim. Acta* **133,** 167 (1987).
104. Sabbatini, N., Perathoner, S., Balzani, V., Alpha, B., and Lehn, J. M. *in* "Supramolecular Photochemistry" (V. Balzani, ed.), p. 187. Reidel, Dordrecht, 1987.
105. Sabbatini, N., and Blasse, G., *J. Lumin.* **40, 41,** 288 (1988).
106. Lehn, J. M., *Angew. Chem.* **100,** 91 (1988).
107. Blasse, G., Dirksen, G. J., van der Voort, D., Sabbatini, N., Perathoner, S., Lehn, J. M., and Alpha, B., *Chem. Phys. Lett.* **146,** 347 (1988); *J. Phys. Chem.* **92,** 2419 (1988).
108. Verwey, J. M. W., Dirksen, G. J., and Blasse, G., *J. Non-cryst. Solids* **107,** 49 (1988).
109. Oversluizen, G., *Fall Meeting Electrochem. Soc. Abstract* **711,** 1047 (1986).
110. Blasse, G., Buijs, M., and Sabbatini, N., *Chem. Phys. Lett.* **124,** 538 (1986).
111. Sabbatini, N., Blasse, G., and Hazenkamp, M. F., unpublished.
112. de Vries, A. J., and Blasse, G., *Mater. Res. Bull.* **22,** 1141 (1987).
113. Srivastava, A. M., Sobieraj, M. T., Ruan, S. K., and Banks, E., *Mater. Res. Bull.* **21,** 1455 (1986).
114. Blasse, G., Dirksen, G. J., van Kooten, W. E. J., and van Walree, C. A., *Chem. Phys. Lett.* **146,** 343 (1988).
115. Verwey, J. W. M., and Blasse, G., *J. Solid State Chem.* **80,** 152 (1989).
116. de Vries, A. J., and Blasse, G., *Mater. Res. Bull.* **21,** 6013 (1986).
117. Blasse, G., and Dirksen, G. J., *J. Solid State Chem.* **73,** 599 (1988).
118. Blasse, G., Breddels, P. A., and McMillin, D. R., *Chem. Phys. Lett.* **109,** 24 (1984).
119. Blasse, G., and Sabbatini, N., *Mater. Chem. Phys.* **16,** 237 (1987).
120. Strauss, E., and Walder, S., *Europhys. Lett.* **6,** 713 (1988).
121. Blasse, G., *in* "Energy Transfer Processes in Condensed Matter," p. 251. Plenum, New York, 1984.
122. Blasse, G., Dirksen, G. J., and Zonnevijlle, F., *J. Inorg. Nucl. Chem.* **43,** 2847 (1981).

123. Balzani, V., Bolletta, F., Gandolfi, M. T., and Maestri, M., *Top. Curr. Chem.* **75,** 1 (1978).
124. Balzani, V., Sabbatini, N., and Scandola, F., *Chem. Revs.* **86,** 319 (1986).
125. Sabbatini, N., Bonazzi, A., Ciano, M., and Balzani, V., *J. Am. Chem. Soc.* **106,** 4055 (1984).
126. Sabbatini, N., and Balzani, V., *J. Less-Common Met.* **112,** 381 (1985).
127. K. K. Rebane, "Impurity Spectra of Solids," Plenum, New York, 1970.
128. Atkins, P. W., "Molecular Quantum Mechanics," 2nd ed., § 12.8. Oxford University Press, Oxford, 1983.
129. Caro, P., Moune, O. K., Antic-Fidancev, E., and Lemaitre-Blaise, M., *J. Less-Common Met.* **112,** 153 (1985).
130. Blasse, G., and Brixner, L. H., *Eur. J. Solid State Inorg. Chem.* **26,** 367 (1989).
131. Blasse, G., *Inorg. Chim. Acta* **169,** 33 (1990).
132. de Vries, A. J., and Blasse, G., *J. Chem. Phys.* **88,** 7312 (1988).
133. Blasse, G., *Inorg. Chim. Acta* **132,** 273 (1987).
134. Brixner, L. H., Crawford, M. K., and Blasse, G., unpublished.
135. Blasse, G., Brixner, L. H., and Mroczkowski, S., *J. Solid State Chem.* **82,** 303 (1989).
136. Blasse, G., and Brixner, L. H., *Inorg. Chim. Acta* **161,** 13 (1989).
137. Blasse, G., and Brixner, L. H., *J. Solid State Chem.* **82,** 151 (1989).
138. Blasse, G., and Brixner, L. H., *Inorg. Chim. Acta* **169,** 25 (1990).
139. Blasse, G., Brixner, L. H., and Sabbatini, N., *Chem. Phys. Lett.* **158,** 504 (1989).
140. Blasse, G., and Brixner, L. H., *Recl. Trav. Chim. Pays-Bas* **109,** 172 (1990).
141. Stavola, M., Isganitis, L., and Sceats, M. G., *J. Chem. Phys.* **74,** 4228 (1981).
142. Stavola, M., Friedman, J. M., Stepnoski, R. A., and Sceats, M. G., *Chem. Phys. Lett.* **80,** 192 (1981).
143. Blasse, G., and Brixner, L. H., *J. Solid State Chem.* **84,** 314 (1989).
144. Brixner, L. H., unpublished.
145. Faulkner, T. R., and Richardson, F. S., *Mol. Phys.* **35,** 1141 (1978).
146. Judd, B. R., *Phys. Scr.* **21,** 543 (1980).
147. Dexpert-Ghys, J., and Auzel, F., *J. Chem. Phys.* **80,** 4003 (1984).
148. Blasse, G., Sytsma, J., and Brixner, L. H., *Chem. Phys. Lett.* **155,** 64 (1989).
149. Judd, B. R., *Phys. Rev.* **127,** 750 (1962).
150. Sytsma, J. A., Imbusch, G. F., and Blasse, G., *J. Chem. Phys.* **91,** 1456 (1989).
151. Moelwijn-Hughes, E. A., "Physical Chemistry." Pergamon Press, Oxford, 1961.
152. Weber, M. J., and Schaufele, R. F., *Phys. Rev.* **138,** A1544 (1965).
153. Garcia, D., and Faucher, M., *J. Chem. Phys.* **90,** 5280 (1989).
154. Berry, M. T., Kirby, A. F., and Richardson, F. S., *Mol. Phys.* **66,** 723 (1989).
155. Branch, U., and Dürr, U., *Opt. Comm.* **49,** 61 (1984).
156. Jenssen, H. P., and Lai, S. T., *J. Opt. Soc. Am.* **B3,** N5 (1986).
157. Lai, S. T., Chai, B. H. T., Long, M., and Morris, R. C., *IEEE J. Quant. Electr.* **22,** 1931 (1986); Blasse, G., and Dirksen, G. J., *Inorg. Chim. Acta* **145,** 303 (1988).
158. Thompson, P. D., and Keszler, D. A., *Chem. Mater.* **1,** 292 (1989).
159. Dolan, J. F., Kappers, L. A., and Bartram, R. H., *Phys. Rev.* **B33,** 7339 (1986).
160. Knochenmuss, R., Reber, C., Rajasekharan, M. V., and Güdel, H. U., *J. Chem. Phys.* **85,** 4280 (1986).
161. van der Poel, W. A. J. A., Noort, M., Herbich, J., Coremans, C. J. M., and van der Waals, J. H., *Chem. Phys. Lett.* **103,** 245 (1984).
162. Barendswaard, W., van Tol, J., and van der Waals, J. H., *Chem. Phys. Lett.* **121,** 361 (1985).
163. Barendswaard, W., and van der Waals, J. H., *Mol. Phys.* **59,** 337 (1986).

164. Barendswaard, W., Thesis, University of Leiden, 1986.
165. Ranfagni, A., Mugni, D., Bacci, M., Viliani, G., and Fontana, M. P., *Adv. Phys.* **32,** 823 (1983).
166. Blasse, G., *Revs. Inorg. Chem.* **5,** 319 (1983); Blasse, G., and van der Steen, A. C., *Solid State Commun.* **31,** 993 (1979).
167. Blasse, G., *Mat. Chem. Phys.* **16,** 201 (1987).
168. van der Steen, A. C., *Phys. Stat. Sol. (b)* **100,** 603 (1980).
169. van der Steen, A. C., and Dijcks, L. T. F., *Phys. Stat. Sol. (b)* **104,** 283 (1981).
170. van der Steen, A. C., van Hesteren, J. J. A., and Slok, A. P., *J. Electrochem. Soc.* **128,** 1327 (1981).
171. Kellendonk, F., van den Belt, T., and Blasse, G., *J. Chem. Phys.* **76,** 1194 (1982).
172. van Zon, F. B. M., Koningsberger, D. C., Oomen, E. W. J. L., and Blasse, G., *J. Solid State Chem.* **71,** 396 (1987).
173. Bersuker, I. B., "The Jahn-Teller Effect and Vibronic Interactions in Modern Chemistry." Plenum Press, New York, 1984.
174. Oomen, E. W. J. L., Smit, W. M. A., and Blasse, G., *J. Phys. C:Sol. St. Phys.* **19,** 3263 (1986).
175. Oomen, E. W. J. L., Dirksen, G. J., Smit, W. M. A., and Blasse, G., *J. Phys. C: Solid St. Phys.* **20,** 1161 (1987).
176. Oomen, E. W. J. L., van Gorkum, L. C. G., Smit, W. M. A., and Blasse, G., *J. Solid State Chem.* **65,** 156 (1986).
177. Oomen, E. W. J. L., Smit, W. M. A., and Blasse, G., *Phys. Rev. B* **37,** 18 (1988).
178. Wernicke, R., Kupka, H., Ensslin, W., and Schmidtke, H. H., *Chem. Phys.* **47,** 235 (1980).
179. Blasse, G., Dirksen, G. J., and Berdowski, P. A. M., *Chem. Phys. Lett.* **112,** 313 (1984).
180. Blasse, G., Dirksen, G. J., and Abriel, W., *Chem. Phys. Lett.* **136,** 460 (1987).
181. Drummen, P., Donker, H., Smit, W. M. A., and Blasse, G., *Chem. Phys. Lett.* **144,** 460 (1988); Donker, H., Smit, W. M. A., and Blasse, G., *J. Phys. Chem. Solids* **50,** 603 (1989).
182. Donker, H., Thesis, University of Utrecht, 1989.
183. Toyozawa, Y., *J. Lumin.* **12, 13,** 13 (1976).
184. Blasse, G., *J. Solid State Chem.* **72,** 72 (1988).
185. de Haart, L. G. J., and Blasse, G., *J. Solid State Chem.* **61,** 135 (1986).
186. Blasse, G., Dirksen, G. J., and Brixner, L. H., *Mater. Res. Bull.* **20,** 989 (1985); Blasse, G., and Brixner, L. H., *Mater. Res. Bull.* **24,** 1099 (1989).
187. Timmermans, C. W. M., and Blasse, G., *Phys. Stat. Sol. (b)* **106,** 647 (1981); *J. Lumin.* **24, 25,** 75 (1981).
188. Donker, H., Smit, W. M. A., and Blasse, G., *Phys. Stat. Sol. (b)* **148,** 413 (1988).
189. Voloshinovskii, A. S., Myagkota, S. V., Pidsyrailo, N. S., and Khapko, Z. A., *Opt. Spectrosc. (USSR)* **52,** 457 (1982).
190. Nikl, M., *Solid State Commun.* **69,** 45 (1989).
191. Clark, S. J., Flint, C. D., and Donaldson, J. D., *J. Phys. Chem. Solids* **42,** 133 (1981).
192. Kellendonk, F., and Blasse, G., *J. Chem. Phys.* **75,** 561 (1984).
193. Bettinelli, M., and Flint, C. D., poster P14 at meeting on Luminescence Fundamentals and Applications, Bologna, May 29/30, 1989.
194. Thorne, J. R. G., Denning, R. G., Barker, T. J., and Grimley, D. I., *J. Lumin.* **34,** 147 (1985).
195. Berdowski, P. A. M., and Blasse, G., *J. Lumin.* **29,** 243 (1984).
196. Buijs, M., and Blasse, G., *J. Solid State Chem.* **71,** 296 (1987).

197. Buijs, M., and Blasse, G., *J. Lumin.* **34,** 263 (1986).
198. Buijs, M., Vree, J. I., and Blasse, G., *Chem. Phys. Lett.* **137,** 381 (1987).
199. Buijs, M., and Blasse, G., *J. Lumin.* **39,** 323 (1988).
200. Buijs, M., Meijerink, A., and Blasse, G., *J. Lumin.* **37,** 9 (1987).
201. de Hair, J. Th. W., and Konijnendijk, W. L., *J. Electrochem. Soc.* **127,** 161 (1980).
202. Blasse, G., Kiliaan, H. S., and de Vries, A. J., *J. Less-common Met.* **126,** 139 (1986).
203. Kiliaan, H. S., Kotte, J. F. A. K., and Blasse, G., *J. Electrochem. Soc.* **134,** 2359 (1987).
204. Salen, Y., Joubert, M. F., Linares, C., and Jacquier, B., *J. Lumin.* **40/41,** 694 (1988).
205. Joubert, M. F., Jacquier, B., and Cone, R. L., *Phys. Rev.* **B35,** 8322 (1987).
206. Mahiou, R., Jacquier, B., and Madej, C., *J. Chem. Phys.* **89,** 5931 (1988).
207. de Vries, A. J., van Vliet, J. P. M., and Blasse, G., *Phys. Stat. Sol. (b)* **149,** 391 (1988).
208. Brixner, L. H., *Mat. Chem. Phys.* **16,** 253 (1987).
209. Corning technical information.
210. Hazenkamp, M. F., and Blasse, G., *Chem. Mater.*, in press (1990).
211. Blasse, G., Brixner, L. H., and Sabbatini, N., *Chem. Phys. Lett.* **158,** 504 (1989).
212. Blasse, G., Buijs, M., and Sabbatini, N., *Chem. Phys. Lett.* **124,** 538 (1986); Sabbatini, N., Dellonte, S., Ciano, M., Bonazzi, A., and Balzani, V., *Chem. Phys. Letters* **107,** 212 (1984).
213. Sabbatini, N., Dellonte, S., and Blasse, G., *Chem. Phys. Lett.* **129,** 541 (1986).
214. van der Voort, D., Blasse, G., Witkamp, G., and van Rosmalen, G., *Mat. Chem. Phys.* **24,** 175 (1989).
215. Blasse, G., Dirksen, G. J., Meijerink, A., van der Pol, J. F., Neeleman, E., and Drenth, W., *Chem. Phys. Lett.* **154,** 420 (1989).
216. Sielcken, O. E., van de Kuil, L. A., Drenth, W., and Nolte, R. J. M., *J. Chem. Soc. Chem. Commun.* 1232 (1988).
217. van der Pol, J. F., Neeleman, E., van Miltenburg, J. C., Zwikker, J. W., Nolte, R. J. M., and Drenth, W., Macromolecules, in press.
218. de Vries, A. J., Smeets, W. J. J., and Blasse, G., *Mater. Chem. Phys.* **18,** 81 (1987).
219. Sabbatini, N., Perathoner, S., Ballardini, R., Balzani, V., Alpha, B., Deschenaux, R., and Lehn, J. M., poster P5 at meeting on Luminescence Fundamentals and Applications, Bologna, May 29/30, 1989.
220. Alpha, B., Ballardini, R., Balzani, V., Lehn, J. M., Perathoner, S., and Sabbatini, N., *Photochem. Photobiol.*, submitted.